Modelado Multi-escala de estimulación hidráulica en reservorios con fracturas naturales

Julieta Gutiérrez

Octubre 2023 Buenos Aires, Argentina

Tesis presentada para el título de Doctora en Ciencia y Tecnología, mención Física

INSTITUTO DE TECNOLOGÍA SABATO

Universidad Nacional de San Martín

Comisión Nacional de Energía Atómica

Contents

Abstract

Unconventional hydrocarbon reservoirs are characterized by a very low permeability. To allow for economical production of these reservoirs, hydraulic stimulation or fracturing is typically required. These reservoirs often contain a network of pre-existing natural fractures that play a crucial role during stimulation and production, by interacting with propagating fractures and their stress field, and providing differentiated transport channels. Often times, other types of mechanical discontinuities are also present, and they similarly affect stimulation and later production.

Modeling and simulation of the stimulation process is often sought-for, to increase the understanding of the underlying mechanics, and to evaluate a range of scenarios allowing for the optimization of the process. Main challenges for the simulation under the conditions described above are: (1) having suitable algorithms and numerical methods that allow for tackling the strong computational demand required for incorporating a significant number of discontinuities in the simulations, and (2) having a reliable benchmark for the interaction between a propagating hydraulic fracture and a mechanical discontinuity.

Y-TEC is currently developing a numerical simulator for hydraulic fracturing and rock mechanics, called Y-FRAC®. The solution of the mechanics problem includes a Discontinuous Galerkin formulation with a cohesive zone model (CZM) for the fracture propagation. The fluid transport problem is embodied by the Reynolds lubrication equation. It is the objective of the present work to deal with the two aforementioned challenges, within the framework of Y-FRAC®.

In connection with the first objective, it is known that the mesh has to be fine enough to resolve the cohesive zones about crack tips. Here, an algorithm was developed which allows for the coarsening of the mesh required to execute a simulation, while providing results that are faithful to those obtained on a mesh with a refinement as per the requirement above. Incorporation of this algorithm in larger scale simulations would thus allow

for an increase in the number of discontinuities included.

As for the second objective, an in-depth analysis was performed of the effect of several parameters (including the critical fracture energies and critical tractions for the matrix and the interface, $G_{c,b}$, $\sigma_{c,b}$, $G_{c,i}$, $\sigma_{c,i}$ respectively) on the result of the interaction between a dry propagating fracture and a mechanical discontinuity, i.e., the deflection versus penetration (D-P) competition. Our analysis is more extended than others available, while the results obtained compare favorably under available similar conditions. The present results provide a more comprehensive view of the D-P competition, with two fundamental conclusions: (1) there exists a significant difference between results provided by linear elastic fracture mechanics (LEFM) and cohesive fracture mechanics (CFM), and (2) there exists an approximately universal relation between a normalized ratio of critical fracture energies $r_G = G_{c,b}/G_{c,i}$, and the ratio of cohesive zone sizes that gives the boundary in the D-P interaction map. These results on dry fracturing provide a robust groundwork for developing an analytical or semi-analytical benchmark to assess the interaction between a hydraulic fracture and a discontinuity.

Resumen

Los yacimientos de hidrocarburos no convencionales se caracterizan por una permeabilidad muy baja. Para permitir la producción económica de estos yacimientos, típicamente se requiere estimulación hidráulica o fracturamiento. Estos yacimientos a menudo contienen una red de fracturas naturales preexistentes que desempeñan un papel crucial durante la estimulación y la producción, al interactuar con las fracturas propagantes y su campo de estrés, y al proporcionar canales de transporte diferenciados. En muchas ocasiones, también están presentes otros tipos de discontinuidades mecánicas, que afectan de manera similar a la estimulación y la producción. Frecuentemente se busca el modelado y la simulación del proceso de estimulación para aumentar la comprensión de los mecanismos subyacentes y evaluar una variedad de escenarios que permitan la optimización del proceso. Los principales desafíos para la simulación en las condiciones descritas son: (1) contar con algoritmos y métodos numéricos adecuados que permitan abordar la fuerte demanda computacional requerida para incorporar un número significativo de discontinuidades en las simulaciones, y (2) disponer de un punto de referencia confiable para la interacción entre una fractura hidráulica propagante y una discontinuidad mecánica. Actualmente, Y-TEC está desarrollando un simulador numérico para fracturamiento hidráulico y mecánica de rocas, llamado Y-FRAC®. La solución del problema de mecánica incluye una formulación de Galerkin discontinua con un modelo de zona cohesiva para la propagación de la fractura. El problema del transporte de fluidos se describe mediante la ecuación de lubricación de Reynolds. El objetivo del presente trabajo es abordar los dos desafíos mencionados, en el marco de Y-FRAC®. En relación con el primer objetivo, se sabe que la malla debe ser lo suficientemente fina como para resolver las zonas cohesivas alrededor de las puntas de las fracturas. Aquí, se desarrolló un algoritmo que permite la disminución de la densidad de la malla requerida para ejecutar una simulación, al tiempo que proporciona resultados fieles a los obtenidos en una malla con un refinamiento según el requisito mencionado. La incorporación de este algoritmo en simulaciones a mayor escala permitiría aumentar el número de discontinuidades incluidas. En cuanto al segundo objetivo, se realizó un análisis exhaustivo del efecto de varios parámetros (incluidas las energías críticas de fractura y tracciones críticas para la matriz y la interfaz, $G_{c,b}$, $\sigma_{c,b}$, $G_{c,i}$, $\sigma_{c,i}$ respectivamente) en el resultado de la interacción entre una fractura propagante seca y una discontinuidad mecánica, es decir, la competencia de desviación versus penetración (D-P). Nuestro análisis es más amplio que otros disponibles, mientras que los resultados obtenidos se comparan favorablemente bajo condiciones similares en la bibliografía. Los resultados actuales proporcionan una visión más completa de la competencia D-P, con dos conclusiones fundamentales: (1) existe una diferencia significativa entre los resultados proporcionados por la mecánica de fractura lineal elástica (LEFM) y la mecánica de fractura cohesiva (CFM), y (2) existe una relación aproximadamente universal entre una relación normalizada de energías críticas de fractura, $r_G = G_{c,b}/G_{c,i}$, y la relación de tamaños de zona cohesiva que proporciona el límite en el mapa de interacción D-P. Estos resultados sobre fracturamiento en seco proporcionan una base sólida para desarrollar un punto de referencia analítico o semi-analítico para evaluar la interacción entre una fractura hidráulica y una discontinuidad.

List of Figures

List of Tables

Chapter 1

Introduction

1.1 Oil and gas reservoirs

Oil and gas are critical resources that power our modern world, providing fuel for transportation, heating, and electricity generation. Depending on the particular characteristics of the rock that contains them and the type of hydrocarbon, different processes are required to produce them.

A petroleum system includes all geological processes and elements needed to generate, accumulate, and store petroleum, natural gas, and other hydrocarbons. It is composed of a hydrocarbon source rock (also known as source rock), a reservoir rock and a seal rock (also known as cap rock). In addition, in a petroleum system, processes are identified that account for the generation, migration and accumulation of hydrocarbons and the formation of a geological trap, capable of containing it in the reservoir rock. During the exploratory stage of a reservoir it is extremely important to identify reservoirs that comply with all the components and processes of a petroleum system, since it allows reducing the uncertainty of finding gas or oil in it. A schematic representation of the above mentioned components and processes is shown in Fig. 1.1.

In the petroleum system, the term ”source rock” refers to sedimentary rocks with abundant organic matter. These rocks undergo burial, causing them to be exposed to high pressure and temperature in an oxygen-deprived environment. As a consequence, the organic matter undergoes physico-chemical transformations, leading to the formation and maturation of hydrocarbons (Ponce et al., 2015).

Reservoirs that present all the elements of the petroleum system and do not require

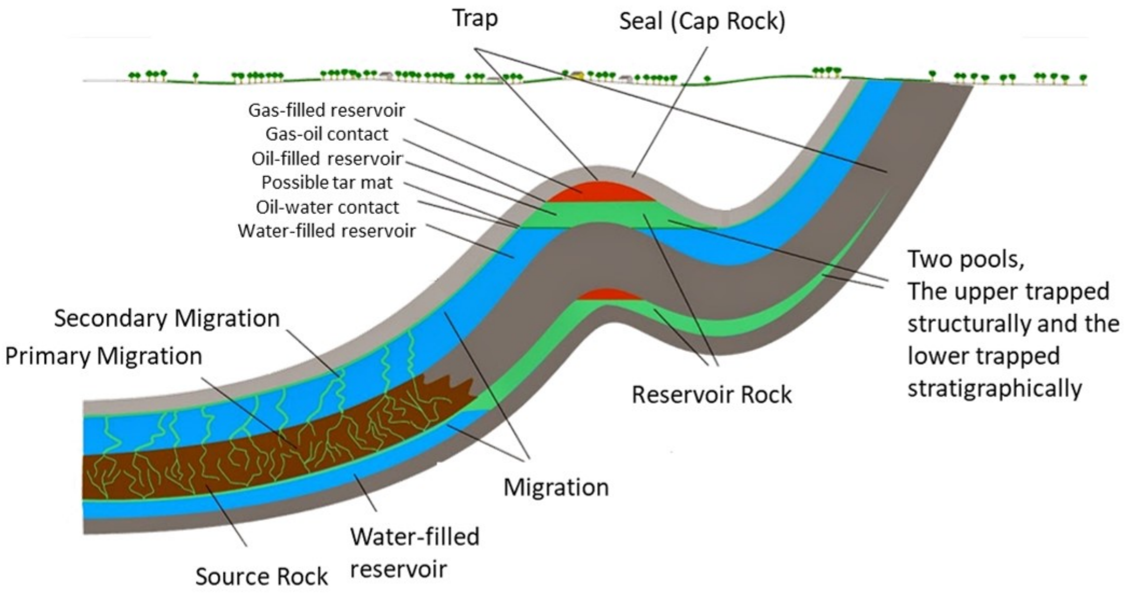

Figure 1.1: Schematic representation of the components of a petroleum system. Its elements (a source rock, a reservoir rock and a cap rock) and its main processes (generation, migration and accumulation of hydrocarbons). Adapted from: http://www.geologyin.com

additional stimulation processes for their development are known as conventional reservoirs, while unconventional reservoirs are those that lack any of the elements or processes defined above.

Conventional reservoirs are typically found in porous rock formations, such as sandstone and limestone, where oil and gas can flow relatively easily through interconnected pores and fractures. In the case of shale-type unconventional reservoirs, the hydrocarbon reaches thermal maturation in the source rock, but does not undergo the migration process, remaining trapped in these rocks of very low permeability.

Typically, in conventional reservoirs, the reservoir rock is formed by porous and permeable rocks that store gas and oil retained by a seal rock. This seal rock, due to its low permeability, prevents the migration of hydrocarbons to the surface or to other adjacent formations and is the one that allows the accumulation of hydrocarbons in the reservoir rock. Under these conditions, in a conventional petroleum system, the source rock generates the hydrocarbons that then migrate to the reservoir rock, where they accumulate (see scheme in Fig. 1.1).

In the particular case of unconventional reservoirs formed by shale-type rocks, the hydrocarbon source rock is also considered the reservoir rock and the seal rock.

In recent years, the energy industry has increasingly turned to unconventional reservoirs to meet growing demand for oil and gas. To extract oil and gas from these formations, unconventional extraction methods such as hydraulic fracturing (fracking) and horizontal drilling are required. Hydraulic fracturing involves pumping large volumes of water, sand, and chemicals into the reservoir at high pressure, creating fractures in the rock that allow oil and gas to flow more freely to the wellbore.

Those unconventional reservoirs have become increasingly important in global hydrocarbon production over the last few decades. This is primarily due to advances in drilling and hydraulic fracturing technologies, which have made it possible to extract hydrocarbons from these previously inaccessible formations (Economides and Nolte, 2000).

The shale revolution in the United States, which began in the early 2000s, is a prime example of the importance of unconventional reservoirs in global hydrocarbon production. The development of shale gas and shale oil resources in the U.S. has transformed the country's energy landscape, making it a net exporter of hydrocarbons for the first time in over half a century (Aguilera and Radetzki, 2014). The success of the shale revolution has also had ripple throughout the global energy industry, with other countries seeking to replicate the U.S. experience.

1.2 Unconventional reservoirs in Argentina

Argentina is another example of the growing importance of unconventional reservoirs in global hydrocarbon production. Different formations are currently under development in the Neuquén basin, the San Jorge Gulf basin and the Austral-Magallanes basin. The Vaca Muerta shale formation, shown in Fig. 1.2, is one of the largest shale gas and shale oil deposits in the world. The development of this resource has the potential to transform Argentina's energy sector and boost the country's economy.

The shale rocks of the Vaca Muerta formation are intrinsically complex, since they present heterogeneities that can act as nucleation points of a fracture or as preferential paths through which to propagate. Among the most studied heterogeneities, due to their presence, extension and importance in the development of hydraulic fractures, are the natural fractures (NFs) (Gale et al., 2014). These are fractures whose characteristics and properties vary greatly. For example, NFs may extend in length by hundreds of

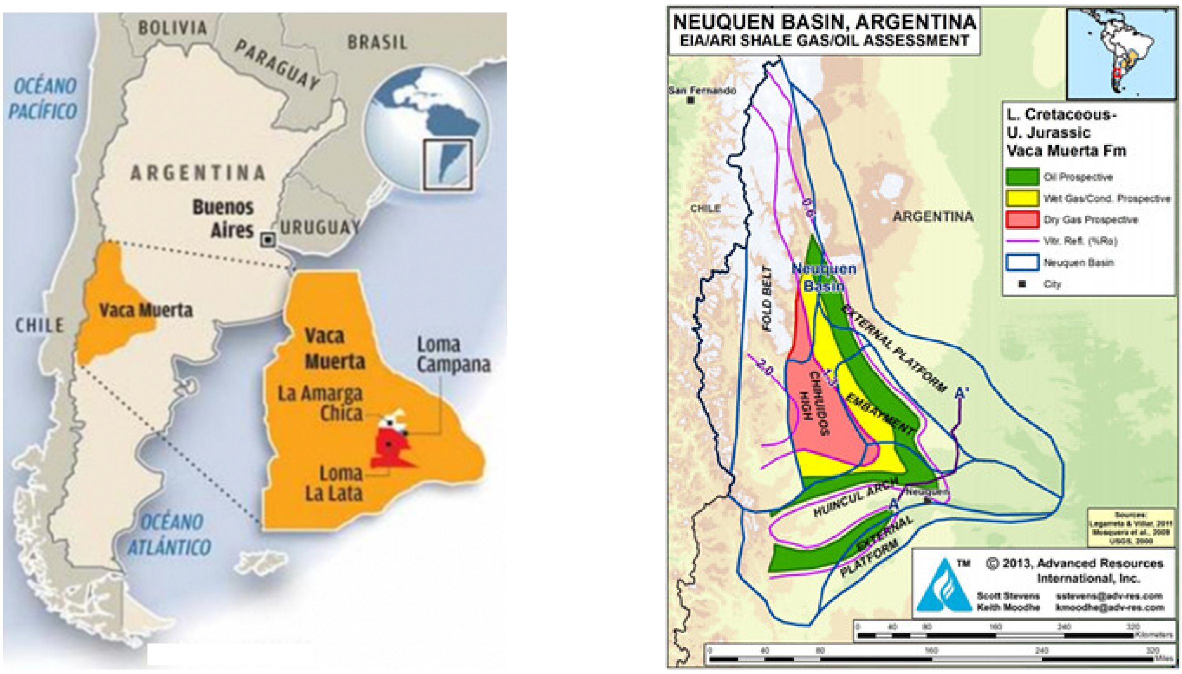

Figure 1.2: (a) Vaca muerta location in Neuquén, Argentina, extracted from www.argentina.gob.ar. (b) A detail of Neuquén Basin, extrated from www.eia.gov.

meters or only by millimeters. Natural fractures in the Vaca Muerta formation are mostly oriented perpendicular to the rock laminations (Gale et al., 2014; Ukar et al., 2017), however, it is possible to find a particular type of NFs known as beefs, or calcitic veins, which are parallel to the direction of sedimentological deposition (Gale et al., 2014). During hydraulic fracture stimulation of unconventional reservoirs, rock heterogeneities can deflect or even arrest (stop) the fracture (Gu et al., 2012, 2010), thus contributing to generate a hydraulic fracture network that increases the stimulated reservoir volume and consequent production (Gale et al., 2018). To a large extent, these heterogeneities are believed to act as high-conductivity pathways connecting the reservoir rock matrix to the wellbore (Wang et al., 2016b).

1.3 Hydraulic fracturing (fracking)

Unconventional reservoirs differ from conventional ones in their low permeability, which makes them economically unfeasible to develop without the use of techniques that allow for an increased production. The hydraulic fracturing or stimulation process aims to improve well productivity by injecting high-pressure fluid (Barati and Liang, 2014). During injection, the rock fractures are generated, seeking to create a high-permeability pathway for hydrocarbon flow from the formation to the well. In order to maintain these permeable pathways after the stimulation process, the fracturing fluid is injected with a propping agent. This propping agent is a particulate material (sand, ceramics, among others) that keeps the fractures open after the stimulation is finished and during the well's production life (Barati and Liang, 2014).

This technique has been used on a smaller scale for decades in conventional reservoirs for the same purpose. In unconventional reservoirs, the operation scale is larger since hydraulic fracturing is used to contact the largest possible volume of the reservoir. In addition to the stimulation of unconventional reservoirs, hydraulic fracturing is an important industrial process in the development of Enhanced Geothermal Systems (EGS), where heat is exchanged with the subsurface by means of the flow of a fluid through the channels generated by hydraulic fractures between the source and sink wells (Zimmermann and Reinicke, 2010). For example, in 2013, large-scale stimulations were carried out to produce geothermal energy in areas near the Newberry Volcano (in the United States), and although these types of plants produced just over 0.5% of the electricity consumed globally in 2016, the technology has great potential for future growth (Bertani, 2016; Ba Geri et al., 2019).

As previously mentioned, hydraulic fracturing in oil and gas applications is a stimulation technique that aims to create a high conductivity channel near the well, allowing for greater stimulated reservoir volume (SRV) and improved productivity. The fluid used in hydraulic fracturing is essential to the process as it promotes the initiation and propagation of fractures in the rock and transports proppants within it. The viscosity and density of the fracturing fluids are their most important properties. Depending on the type of fluid (and the attendant viscosity), they are classified into slickwater (2-3 cP), linear gels (20-50 cP), cross-linked gels (100-2000 cP), and High Viscosity Friction Reducers (HVFR) (Ba Geri et al., 2019; Hu et al., 2018).

Prior to pumping, a tool is used to perforate the casing, to connect the well with the formation. The stimulation is done by pumping fluid and proppant at high rates along the length of the well in multiple evenly-spaced stages. Pressure increases until the rock fractures, propagating the hydraulic fracture. The pumping for each stage lasts around two hours, and the process is repeated for each stage (Economides et al., 2007). Roughly 40 stages of hydraulic fracturing are conducted per horizontal well in the Vaca Muerta formation at present day.

A schematic of the hydraulic fracturing process in a shale gas reservoir is shown in Fig. 1.3, depicting the surface facilities that pump the fluid into the well, through the perforations, and finally into the formation. The flow rate during the hydraulic stimulation process must exceed the fluid loss rate to the formation, known as leak-off, to achieve pressure and fracture propagation. One of the main experimental methods available to estimate the volume of the stimulated reservoir is micro-seismic acquisition and processing, which maps the sub-seismic events produced during fracture propagation. However, this method is only used as an approximation and upper limit of the final stimulated volume, as it is impossible to determine whether fluid or proppant have reached the zones where micro-seismic events occur, or if they are isolated events.

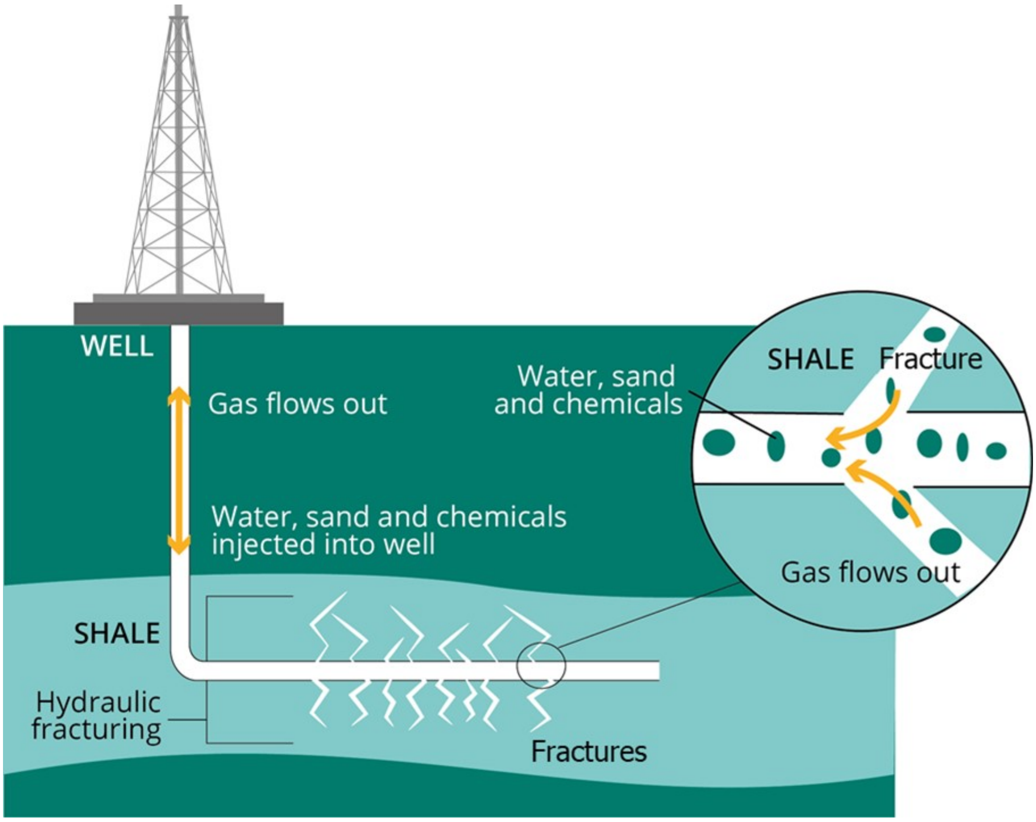

Figure 1.3: Simplified scheme of shale gas extraction through hydraulic fracturing. Image adapted from: https://www.eea.europa.eu

1.4 Naturally fractured reservoirs

Natural fractures play a crucial role in the stimulation and production of unconventional reservoirs. Understanding the spatial distribution, orientation, and connectivity of natural fractures is critical for the efficient development of these reservoirs (Warpinski et al., 2009; Wang, 2019; Economides and Nolte, 2000).

Fracture networks can enhance permeability and provide preferential flow paths for hydrocarbons to flow through the reservoir. This can significantly improve production rates and recovery factors.

Several studies have highlighted the importance of natural fractures in unconventional reservoirs. For example, a study by Gale et al. (2014) showed that natural fractures can significantly improve the permeability and hydraulic conductivity of shale formations. Another study by Wang et al. (2017) demonstrated that the spatial distribution and orientation of natural fractures can significantly affect the production performance of shale reservoirs.

Furthermore, the work of Yang et al. (2019) showed that the connectivity of natural fractures is crucial for the success of hydraulic fracturing treatments in shale reservoirs. They found that the presence of well-connected natural fractures enhances the effectiveness of hydraulic fracturing treatments and increases the production rates of the reservoir.

In conclusion, the understanding of natural fractures and their role in unconventional reservoirs is essential for the efficient development and production of these resources.

1.5 Fracture propagation modeling and simulation

There are numerous numerical methods that allow simulating both the deformation and fracture process in solids, as well as the initiation and propagation of hydraulic fractures. The most commonly used numerical models for modeling fracture propagation include the Displacement Discontinuity Method (DDM) (Ye et al., 2018; Zhang et al., 2012; Kresse et al., 2013; Weng et al., 2011, 2014; Wu et al., 2017), the Discrete Element Method (DEM) (Damjanac et al., 2016; De Pater and Beugelsdijk, 2005; Nagel et al., 2013; Zhou, 2016; Basirat et al., 2019), the Finite Element Method (FEM) and its variations such as the extended Finite Element Method (xFEM) (Remij et al., 2018), which uses enriched functions to incorporate stress singularities present in the analytical solution of stresses at the crack tip, the Finite Element Method with a damage model (Wang et al., 2017; Guo et al., 2017), or with cohesive zone models (CZM) (Taleghani et al., 2018), and the Discontinuous Galerkin (DG) method.

In this work, the chosen numerical methodology is the FEM with a DG formulation, which allows modeling both deformation and rock fracture. During the evolution of the mechanical problem, stresses and deformations in the rock are determined by constitutive laws and material models. The fracture process starts in the rock when stresses reach a critical condition. The evolution of the fracture process follows a linear softening cohesive zone modeling (CZM) law. This law determines the relationship between stresses and displacements in the fracture process zone while the rock still exhibits cohesion. Total decohesion is reached when all the fracture energy, a material property of the rock, is released. In cases where hydraulic fracture propagation is studied, the fracturing fluid flows through the fractured zones of the solid.

The FEM-DG-CZM methodology has comparative advantages over other numerical methods. For example, fracture nucleation and propagation can be modeled without modifying the finite element mesh since the method allows for incorporating displacement jumps between elements. Additionally, hydraulic fracture modeling is simply resolved by incorporating fluid flow within the channels created by the separation between these elements.

1.6 Numerical modeling of hydraulic stimulation in reservoirs with natural fractures

Numerical modeling and simulation offer an alternative approach to studying the behavior of hydraulic fracture propagation in naturally fractured reservoirs. This approach is necessary because small-scale laboratory experiments cannot replicate in-situ conditions with extremely high confining stress. Furthermore, during fracture propagation, stress anisotropy can be much lower than intended or even disappear due to fixed displacement at the rock sample boundary, as indicated by Malhotra et al. (2018). The boundary effect cannot be fully eliminated, even if a constant far-field stress field is maintained during fracture propagation. In addition, small-scale laboratory experiments cannot fully capture the impact of flow resistance dependent fluid distribution, resulting in hydraulic fracture patterns that are more complex than those found in the subsurface (Wang, 2019).

Several studies have investigated the interaction between hydraulic fractures and natural fractures using the displacement discontinuity method (DDM) (Taleghani and Olson, 2011; McClure and Horne, 2013; Sesetty and Ghassemi, 2017; Shrivastava and Sharma, 2018; Weng et al., 2011). The DDM is a type of boundary integral method that requires only discretization at the fracture surface boundaries, making it computationally efficient compared to the finite element method (FEM) or finite volume method (FVM). However, the DDM is limited to brittle rocks because its underlying assumptions are based on linear elastic fracture mechanics (LEFM). Laboratory experiments (Sone and Zoback, 2013; Hull et al., 2015) on shale samples from a variety of shale plays in U.S found that the ductility of shale sample is strongly correlated to its organic and clay content. Furthermore, sedimentary rocks tend to transit from brittle to ductile under high confining pressure (Wong and Baud, 2012), so it may not be appropriate to use DDM in deep reservoirs or shale plays with a relatively high content of clay or kerogen. Additionally, DDM assumes homogeneous properties, making it difficult to tackle challenging cases such as different rock properties along the horizontal wellbore, multi-layer formations, and near-wellbore fracture modeling. Furthermore, DDM models require a pre-defined crossing criterion based on plain strain condition, infinite elastic domain, and local Mohr-Coulomb law, making it challenging to apply in naturally fractured reservoirs in a fully coupled manner (Wang, 2019).

This study employs the cohesive zone method (CZM) to simulate hydraulic fracture propagation, which provides a promising approach for modeling complex fracture growth and interaction in reservoirs with natural fractures, without the limitations of predefined fracture propagation paths. The CZM was first introduced by Barenblatt (1959, 1962) for brittle materials, and later extended by Dugdale (1960) for ductile materials. More recent work includes a cohesive zone model for soft rock by Mokryakov (2011), a hydraulic fracture model for poroelastic and poroplastic formations by Wang et al. (2016a), a cohesive zone model for layered reservoirs by Guo et al. (2017), and a 3D cohesive zone model for multiple hydraulic fracture propagation with heterogeneity by Manchanda et al. (2018). While there have been successful implementations of CZM for planar and non-planar hydraulic fractures, there is limited work on modeling hydraulic fractures interacting with natural fractures using the CZM. Previous studies by Guo et al. (2015), Chen et al. (2017)

,and Taleghani et al. (2018) require predefining a fracture propagation path within the intact rock domain, which limits the generality of their models when simulating complex fracture growth.

1.7 Outline

The present dissertation focuses on the modeling of hydraulic fracture stimulation in reservoirs with natural fractures. Incorporation in the model of a natural fracture that can undergo deformation and link to the stimulated network of fractures to transport fluid, in an otherwise continuous region, typically increases the degrees of freedom of the system. However, including a large number of discontinuities in the model may increase the degrees of freedom of the system to the point where it becomes intractable.

To address these challenges, we utilize Y-FRAC®, a numerical hydraulic fracturing simulator designed for parallel computing. This simulator allows us to model the hydraulic stimulation, incorporating fracture and fluid mechanics. However, due to the demanding calculations involved, only a limited number of natural fractures can be incorporated into the simulations in a discrete manner.

In Chapter 3, we analyze the evolution of the fundamental variables across the life of a hydraulic fracture, from large to small fluid lag, and cover various propagation regimes. This analysis is crucial for setting up simulation parameters accurately. Additionally, we explore the validity of an approximate universal behavior that was previously described by Garagash (2006b) for the early and late time regimes and extend the result to a larger region in the domain of system parameters. We also provide quantitative time bounds for the applicability of each propagation regime and a method for the quantitative mapping of related quantities.

Chapter 4 presents a systematic study to identify controlling factors in the interaction between a hydraulic fracture and a natural fracture. We find that in the fluid lag regime, the interaction mode is controlled by the critical traction, and essentially independent of fracture energy. However, in the fluid lag-free regime, the results do not show a clear trend, and the interaction mode depends somewhat on the mesh type and the time increment. These results highlight the essential need for benchmark solutions for the interaction under simplifying conditions.

The problem of finding benchmark solutions for the interaction between a propagating hydraulic fracture and a natural fracture is divided into two cases: deflection of the hydraulic fracture into the natural fracture (kink-in) and deflection out of the natural fracture (kink-out). Unfortunately, there are no known analytic solutions for either case. In Chapter 5, we focus on the first problem and begin with the case of dry crack propagation. Even in this case, there are no analytic solutions, but a few numerical studies contribute to the body of knowledge on possible benchmarks.

Finally, in Chapter 6, we propose a new speed-up algorithm based on fracture energy adaptation and test it for hydraulic fracture simulations with natural fractures.

Capítulo 2

Introducción

2.1 Reservorios de Gas y petróleo

El petróleo y el gas son recursos críticos que impulsan nuestro mundo moderno, proporcionando combustible para el transporte, calefacción y generación de electricidad. Dependiendo de las características particulares de la roca que los contiene y del tipo de hidrocarburo, se requieren diferentes procesos para producirlos.

Un sistema petrolero incluye todos los procesos geológicos y elementos necesarios para generar, acumular y almacenar petróleo, gas natural y otros hidrocarburos. Está compuesto por una roca fuente de hidrocarburos (también conocida como roca madre), una roca de reservorio y una roca de sellado (también conocida como roca tapón). Además, en un sistema petrolero, se identifican procesos que explican la generación, migración y acumulación de hidrocarburos y la formación de una trampa geológica capaz de contenerlos en la roca de reservorio. Durante la etapa exploratoria de un yacimiento, es extremadamente importante identificar yacimientos que cumplan con todos los componentes y procesos de un sistema petrolero, ya que esto permite reducir la incertidumbre de encontrar gas u petróleo en él. Se muestra una representación esquemática de los componentes y procesos mencionados anteriormente en la Fig. 2.1.

En el sistema petrolero, el término ”roca madre” se refiere a rocas sedimentarias con abundante materia orgánica. Estas rocas experimentan entierro, lo que las expone a alta presión y temperatura en un entorno sin oxígeno. Como consecuencia, la materia orgánica sufre transformaciones fisicoquímicas, dando lugar a la formación y maduración de hidrocarburos (Ponce et al., 2015).

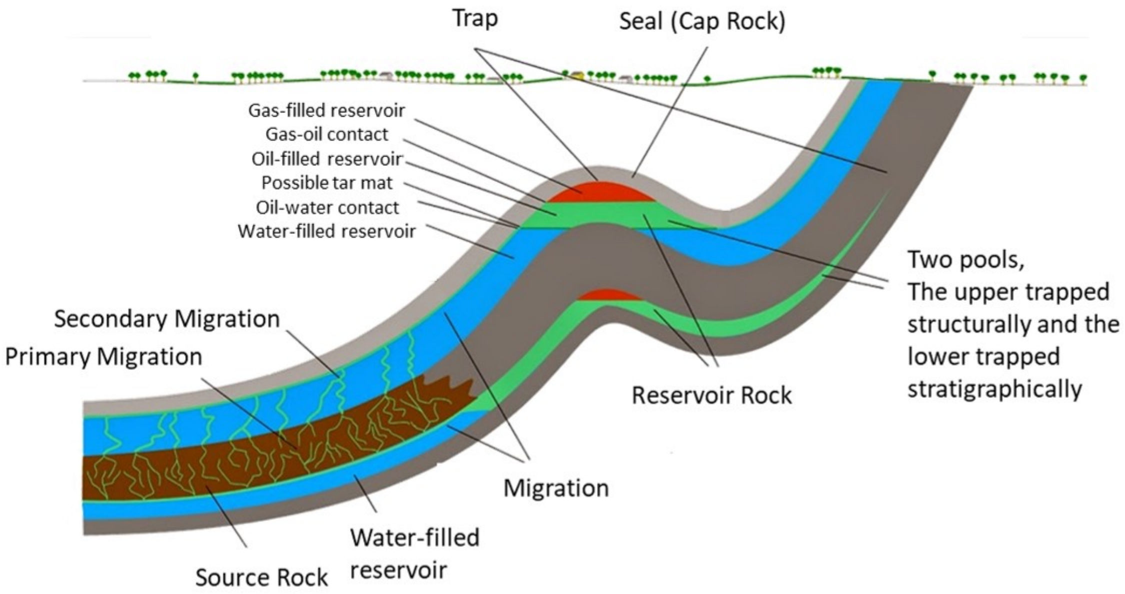

Figure 2.1: Representación esquemática de los componentes de un sistema petrolero. Sus elementos (una roca madre, una roca de reservorio y una roca tapón) y sus procesos principales (generación, migración y acumulación de hidrocarburos). Adaptado de: http://www.geologyin.com

Los yacimientos que presentan todos los elementos del sistema petrolero y no requieren procesos adicionales de estimulación para su desarrollo se conocen como yacimientos convencionales, mientras que los yacimientos no convencionales son aquellos que carecen de alguno de los elementos o procesos definidos anteriormente.

Los yacimientos convencionales se encuentran típicamente en formaciones rocosas porosas, como arenisca y caliza, donde el petróleo y el gas pueden fluir relativamente fácilmente a través de poros y fracturas interconectados. En el caso de los yacimientos no convencionales del tipo lutita (shale), el hidrocarburo alcanza la maduración térmica en la roca madre, pero no experimenta el proceso de migración, quedando atrapado en estas rocas de muy baja permeabilidad.

Por lo general, en los yacimientos convencionales, la roca de reservorio está formada por rocas porosas y permeables que almacenan gas y petróleo retenidos por una roca tapón. Esta roca tapón, debido a su baja permeabilidad, impide la migración de hidrocarburos hacia la superficie u otras formaciones adyacentes y es la que permite la acumulación de hidrocarburos en la roca de reservorio. Bajo estas condiciones, en un sistema petrolero convencional, la roca fuente, o madre, genera los hidrocarburos que luego migran a la roca de reservorio, donde se acumulan (ver esquema en Fig. 2.1).

En el caso particular de yacimientos no convencionales formados por rocas del tipo lutita, la roca fuente de hidrocarburos se considera también la roca de reservorio y la roca tapón.

En los últimos años, la industria energética se ha volcado cada vez más hacia yacimientos no convencionales para satisfacer la creciente demanda de petróleo y gas. Para extraer petróleo y gas de estas formaciones, se requieren métodos de extracción no convencionales como la fracturación hidráulica (fracking) y la perforación horizontal. La fracturación hidráulica implica bombear grandes volúmenes de agua, arena y productos químicos en el yacimiento a alta presión, creando fracturas en la roca que permiten que el petróleo y el gas fluyan más libremente hacia el pozo.

Estos yacimientos no convencionales se han vuelto cada vez más importantes en la producción global de hidrocarburos en las últimas décadas. Esto se debe principalmente a los avances en tecnologías de perforación y fracturación hidráulica, que han permitido extraer hidrocarburos de estas formaciones previamente inaccesibles (Economides and Nolte, 2000).

La revolución del shale en los Estados Unidos, que comenzó a principios de la década de 2000, es un ejemplo destacado de la importancia de los yacimientos no convencionales en la producción global de hidrocarburos. El desarrollo de recursos de gas y petróleo tipo shale en los EE. UU. ha transformado el panorama energético del país, convirtiéndolo en un exportador neto de hidrocarburos por primera vez en más de medio siglo (Aguilera and Radetzki, 2014). El éxito de la revolución del shale también ha tenido repercusiones en toda la industria energética mundial, con otros países buscando replicar la experiencia estadounidense.

2.2 Reservorios no convencionales en Argentina

Argentina es otro ejemplo de la creciente importancia de los yacimientos no convencionales en la producción global de hidrocarburos. Actualmente, se están desarrollando diversas formaciones en la cuenca Neuquina, la cuenca del Golfo San Jorge y la cuenca Austral-Magallanes. La formación tipo shale Vaca Muerta, mostrada en la Fig. 2.2, es uno de los depósitos más grandes de gas y petróleo tipo shale en el mundo. El desarrollo de este recurso tiene el potencial de transformar el sector energético de Argentina y impulsar la economía del país.

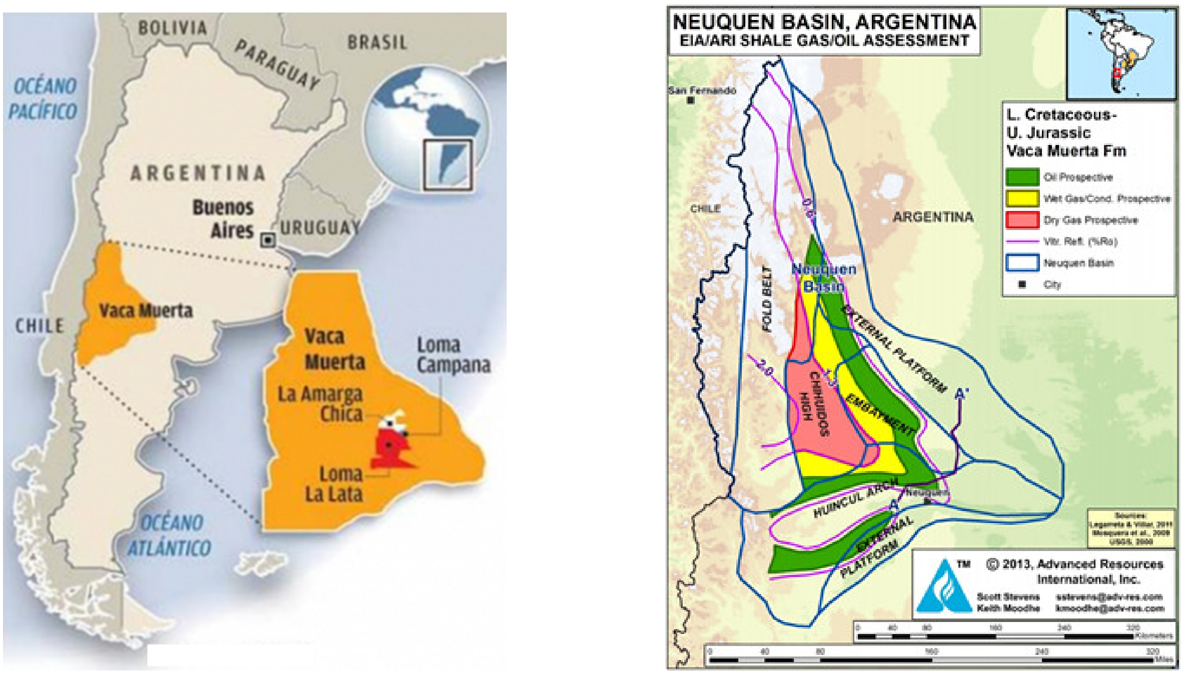

Figure 2.2: (a) Ubicación de Vaca Muerta en Neuquén, Argentina, extraída de www.argentina.gob.ar. (b) Detalle de la Cuenca Neuquina, extraído de www.eia.gov.

Las rocas tipo shale de la formación Vaca Muerta son intrínsecamente complejas, ya que presentan heterogeneidades que pueden actuar como puntos de nucleación de una fractura o como senderos preferenciales a lo largo de los cuales propagarse. Entre las heterogeneidades más estudiadas, debido a su presencia, extensión e importancia en el desarrollo de fracturas hidráulicas, se encuentran las fracturas naturales (NFs) (Gale et al., 2014). Estas son fracturas cuyas características y propiedades varían considerablemente. Por ejemplo, las NFs pueden extenderse en longitud desde cientos de metros hasta solo milímetros. Las fracturas naturales en la formación Vaca Muerta están mayormente orientadas perpendicularmente a las laminaciones de la roca (Gale et al., 2014; Ukar et al., 2017); sin embargo, es posible encontrar un tipo particular de NFs conocidas como vetas de calcita o "beefs", que son paralelas a la dirección de deposición sedimentológica (Gale et al., 2014). Durante la estimulación de fracturas hidráulicas en yacimientos no convencionales, las heterogeneidades de la roca pueden desviar o incluso detener la fractura (Gu et al., 2012, 2010), contribuyendo así a generar una red de fracturas hidráulicas que aumenta el volumen del yacimiento estimulado y, por ende, la producción (Gale et al., 2018). En gran medida, se cree que estas heterogeneidades actúan como vías de alta conductividad que conectan la matriz de la roca del yacimiento con el pozo (Wang et al., 2016b).

2.3 Fractura hidráulica (fracking)

Los yacimientos no convencionales difieren de los convencionales en su baja permeabilidad, lo que los hace económicamente inviables de desarrollar sin el uso de técnicas que permitan un aumento en la producción. El proceso de fracturamiento o estimulación hidráulica tiene como objetivo mejorar la productividad del pozo mediante la inyección de un fluido a alta presión (Barati and Liang, 2014). Durante la inyección, se generan fracturas en la roca, buscando crear un camino de alta permeabilidad para el flujo de hidrocarburos desde la formación hasta el pozo. Para mantener estos caminos permeables después del proceso de estimulación, se inyecta el fluido de fracturamiento con un agente de sostén. Este agente sostén es un material particulado (arena, cerámica, entre otros) que mantiene las fracturas abiertas después de que finaliza la estimulación y durante la vida productiva del pozo (Barati and Liang, 2014).

Esta técnica se ha utilizado en menor escala durante décadas en yacimientos convencionales con el mismo propósito. En yacimientos no convencionales, la escala de operación es mayor, ya que el fracturamiento hidráulico se utiliza para contactar el volumen más grande posible del yacimiento. Además de la estimulación de yacimientos no convencionales, el fracturamiento hidráulico es un proceso industrial importante en el desarrollo de Sistemas Geotérmicos Mejorados (EGS), donde se intercambia calor con el subsuelo mediante el flujo de un fluido a través de los canales generados por fracturas hidráulicas entre los pozos de origen y destino (Zimmermann and Reinicke, 2010). Por ejemplo, en 2013, se llevaron a cabo estimulaciones a gran escala para producir energía geotérmica en áreas cercanas al volcán Newberry (en Estados Unidos), y aunque estas plantas produjeron poco más del 0.5% de la electricidad consumida a nivel mundial en 2016, la tecnología tiene un gran potencial de crecimiento futuro (Bertani, 2016; Ba Geri et al., 2019).

Como se mencionó anteriormente, la fractura hidráulica en aplicaciones de petróleo y gas es una técnica de estimulación que tiene como objetivo crear un canal de alta conductividad cerca del pozo, permitiendo un mayor volumen de yacimiento estimulado (SRV) y una mejora en la productividad. El fluido utilizado es esencial para el proceso, ya que promueve la iniciación y propagación de fracturas en la roca y transporta los agentes de sostén en su interior. La viscosidad y densidad de los fluidos de fractura son sus propiedades más importantes. Dependiendo del tipo de fluido (y la viscosidad asociada), se clasifican en slickwater (2-3 cP), geles lineales (20-50 cP), geles reticulados (100-2000 cP) y Reductores de Fricción de Alta Viscosidad (HVFR) (Ba Geri et al., 2019; Hu et al., 2018).

Antes de la inyección, se utiliza una herramienta para perforar el revestimiento (casing) y conectar el pozo con la formación. La estimulación se realiza mediante la inyección de fluido y agente de sostén a tasas elevadas a lo largo de la longitud del pozo en múltiples etapas espaciadas uniformemente. La presión aumenta hasta que la roca se fractura, propagando la fractura hidráulica. La inyección para cada etapa dura alrededor de dos horas, y el proceso se repite para cada etapa (Economides et al., 2007). Aproximadamente se realizan alrededor de 40 etapas de fracturamiento hidráulico por pozo horizontal en la formación Vaca Muerta en la actualidad.

En la Fig. 2.3 se muestra un esquema del proceso de fracturamiento hidráulico en un yacimiento de gas de lutitas, que representa las instalaciones en la superficie que bombean el fluido al pozo, a través de las perforaciones, y finalmente hacia la formación. La tasa de flujo durante el proceso de estimulación hidráulica debe superar la tasa de pérdida de fluido hacia la formación, conocida como leak-off, para lograr la presión y la propagación de la fractura. Uno de los principales métodos experimentales disponibles para estimar el volumen del yacimiento estimulado es la adquisición y procesamiento de microsísmica, que mapea los eventos sub-sísmicos producidos durante la propagación de la fractura. Sin embargo, este método se utiliza solo como una aproximación y un límite superior del volumen estimulado final, ya que es imposible determinar si el fluido o el agente de sostén han llegado a las zonas donde se producen los eventos microsísmicos, o si son eventos aislados.

2.4 Reservorios con fracturas naturales

Las fracturas naturales desempeñan un papel crucial en la estimulación y producción de yacimientos no convencionales. Comprender la distribución espacial, orientación y conectividad de las fracturas naturales es fundamental para el desarrollo eficiente de

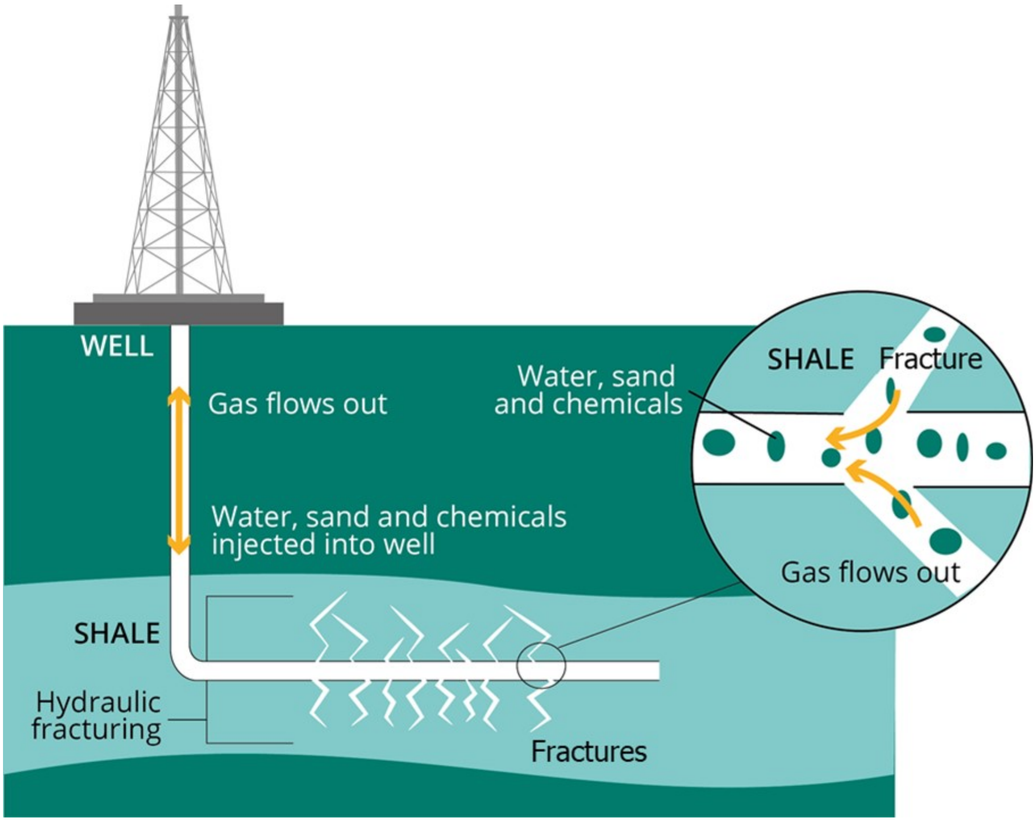

Figure 2.3: Esquema simplificado de la extracción de gas de lutitas mediante fracturamiento hidráulico. Imagen adaptada de: https://www.eea.europa.eu

estos yacimientos (Warpinski et al., 2009; Wang, 2019; Economides and Nolte, 2000).

Las redes de fracturas pueden mejorar la permeabilidad y proporcionar trayectorias de flujo preferenciales para que los hidrocarburos fluyan a través del yacimiento. Esto puede mejorar significativamente las tasas de producción y los factores de recuperación.

Además, el fracturamiento hidráulico, que se utiliza comúnmente para estimular la producción en yacimientos no convencionales, depende de las fracturas naturales preexistentes para crear y propagar fracturas hidráulicas.

Varios estudios han destacado la importancia de las fracturas naturales en yacimientos no convencionales. Por ejemplo, un estudio de Gale et al. (2014) mostró que las fracturas naturales pueden mejorar significativamente la permeabilidad y la conductividad hidráulica de las formaciones tipo shale. Otro estudio de Wang et al. (2017) demostró que la distribución espacial y orientación de las fracturas naturales puede afectar significativamente el rendimiento de producción de los yacimientos tipo shale.

Además, el trabajo de Yang et al. (2019) mostró que la conectividad de las fracturas naturales es crucial para el éxito de los tratamientos de fracturamiento hidráulico en yacimientos shale. Encontraron que la presencia de fracturas naturales bien conectadas mejora la eficacia de los tratamientos de fracturamiento hidráulico y aumenta las tasas de producción del yacimiento.

En conclusión, la comprensión de las fracturas naturales y su papel en yacimientos no convencionales es esencial para el desarrollo eficiente y la producción de estos recursos.

2.5 Modelado y simulación de la propagación de fracturas

Existen numerosos métodos numéricos que permiten simular tanto el proceso de deformación y fractura en sólidos, como la iniciación y propagación de fracturas hidráulicas. Los modelos numéricos más comúnmente utilizados para modelar la propagación de fracturas incluyen el Método de Discontinuidad de Desplazamiento (DDM) (Ye et al., 2018; Zhang et al., 2012; Kresse et al., 2013; Weng et al., 2011, 2014; Wu et al., 2017), el Método de Elementos Discretos (DEM) (Damjanac et al., 2016; De Pater and Beugelsdijk, 2005; Nagel et al., 2013; Zhou, 2016; Basirat et al., 2019), el Método de Elementos Finitos (FEM) y sus variaciones como el Método de Elementos Finitos Extendido (xFEM) (Remij et al., 2018), que utiliza funciones enriquecidas para incorporar singularidades de esfuerzos presentes en la solución analítica de esfuerzos en la punta de la fractura, el Método de Elementos Finitos con un modelo de daño (Wang et al., 2017; Guo et al., 2017), o con modelos de zona cohesiva (CZM) (Taleghani et al., 2018), y el Método de Galerkin Discontinuo (DG).

En este trabajo, la metodología numérica elegida es el FEM con una formulación DG, que permite modelar tanto la deformación como la fractura de la roca. Durante la evolución del problema mecánico, los esfuerzos y deformaciones en la roca se determinan mediante leyes constitutivas y modelos de materiales. El proceso de fractura comienza en la roca cuando los esfuerzos alcanzan una condición crítica. La evolución del proceso de fracturamiento sigue una ley de modelado lineal de zona cohesiva (CZM). Esta ley determina la relación entre los esfuerzos y desplazamientos en la zona del proceso de fracturamiento mientras la roca aún exhibe cohesión. La decohesión total se alcanza cuando se libera toda la energía de fracturamiento, una propiedad material de la roca. En casos en los que se estudia la propagación de fracturas hidráulicas, el fluido de fracturamiento fluye a través de las zonas fracturadas del sólido.

La metodología FEM-DG-CZM tiene ventajas comparativas sobre otros métodos numéricos. Por ejemplo, la nucleación y propagación de fracturas se pueden modelar sin modificar la malla de elementos finitos, ya que el método permite incorporar saltos de desplazamiento entre elementos. Además, el modelado del fracturamiento hidráulico se resuelve simplemente incorporando el flujo de fluido dentro de los canales creados por la separación entre estos elementos.

2.6 Modelado numérico de la estimulación hidráulica en yacimientos con fracturas naturales.

El modelado numérico y la simulación ofrecen un enfoque alternativo para estudiar el comportamiento de la propagación de fracturas hidráulicas en yacimientos naturalmente fracturados. Este enfoque es necesario porque los experimentos de laboratorio a pequeña escala no pueden replicar las condiciones in situ con un estrés de confinamiento extremadamente alto. Además, durante la propagación de la fractura, la anisotropía del estrés puede ser mucho menor de lo previsto o incluso desaparecer debido al desplazamiento fijo en el límite de la muestra de roca, como indicó Malhotra et al. (2018). El efecto de límite no se puede eliminar por completo, incluso si se mantiene un campo de estrés constante lejos del campo de fractura durante la propagación. Además, los experimentos de laboratorio a pequeña escala no pueden capturar completamente el impacto de la distribución de fluido dependiente de la resistencia al flujo, lo que resulta en patrones de fractura hidráulica más complejos que los encontrados en el subsuelo (Wang, 2019).

Varios estudios han investigado la interacción entre fracturas hidráulicas y fracturas naturales utilizando el método de discontinuidad de desplazamiento (DDM) (Taleghani and Olson, 2011; McClure and Horne, 2013; Sesetty and Ghassemi, 2017; Shrivastava and Sharma, 2018; Weng et al., 2011). El DDM es un tipo de método integral de límites que solo requiere discretización en los límites de las superficies de fractura, lo que lo hace computacionalmente eficiente en comparación con el método de elementos finitos (FEM) o el método de volumen finito (FVM). Sin embargo, el DDM está limitado a rocas frágiles porque sus suposiciones subyacentes se basan en la mecánica de fractura elástica lineal (LEFM). Experimentos de laboratorio (Sone and Zoback, 2013; Hull et al.,

2015) en muestras tipo shale de diversas formaciones en EE. UU. encontraron que la ductilidad de la muestra está fuertemente correlacionada con su contenido de materia orgánica y arcilla. Además, las rocas sedimentarias tienden a pasar de frágiles a dúctiles bajo una alta presión de confinamiento (Wong and Baud, 2012), por lo que puede que no sea apropiado utilizar DDM en yacimientos profundos o en formaciones shale con un contenido relativamente alto de arcilla o querógeno. Además, DDM asume propiedades homogéneas, lo que dificulta abordar casos desafiantes como diferentes propiedades de roca a lo largo del pozo horizontal, formaciones de múltiples capas y modelado de fracturas cerca del pozo (Wang, 2019). Además, los modelos DDM requieren un criterio de cruce predefinido basado en la condición de deformación plana, dominio elástico infinito, y la ley de Mohr-Coulomb local, lo que dificulta su aplicación en yacimientos naturalmente fracturados de manera completamente acoplada (Wang, 2019).

Este estudio emplea el método de zona cohesiva (CZM) para simular la propagación de fracturas hidráulicas, lo que proporciona un enfoque prometedor para modelar el crecimiento y la interacción complejos de fracturas en yacimientos con fracturas naturales, sin las limitaciones de trayectorias de propagación de fracturas predefinidas. El CZM fue introducido por primera vez por Barenblatt (1959, 1962) para materiales frágiles, y luego extendido por Dugdale (1960) para materiales dúctiles. Trabajos más recientes incluyen un modelo de zona cohesiva para rocas blandas por Mokryakov (2011), un modelo de fractura hidráulica para formaciones poroelásticas y poroplásticas por Wang et al. (2016a), un modelo de zona cohesiva para yacimientos estratificados por Guo et al. (2017), y un modelo de zona cohesiva 3D para la propagación múltiple de fracturas hidráulicas con heterogeneidad por Manchanda et al. (2018). Aunque ha habido implementaciones exitosas de CZM para fracturas hidráulicas planas y no planas, hay trabajos limitados sobre la modelización de fracturas hidráulicas que interactúan con fracturas naturales utilizando el CZM. Estudios anteriores de Guo et al. (2015), Chen et al. (2017), y Taleghani et al. (2018) requieren predefinir una trayectoria de propagación de fracturas dentro del dominio de roca intacta, lo que limita la generalidad de sus modelos al simular el crecimiento complejo de fracturas.

2.7 Esquema

La presente tesis se centra en la modelización de la estimulación de fracturas hidráulicas en yacimientos con fracturas naturales. La incorporación en el modelo de una fractura natural que puede sufrir deformaciones y conectarse a la red estimulada de fracturas para transportar fluido, en una región por lo demás continua, generalmente aumenta los grados de libertad del sistema. Sin embargo, incluir un gran número de discontinuidades en el modelo puede aumentar los grados de libertad del sistema hasta el punto de hacerlo intratable.

Para abordar estos desafíos, utilizamos Y-FRAC®, un simulador numérico de fracturación hidráulica diseñado para cómputo en paralelo. Este simulador nos permite modelar la estimulación hidráulica, incorporando la mecánica de fracturas y fluidos. Sin embargo, debido a los cálculos exigentes involucrados, solo se pueden incorporar un número limitado de fracturas naturales en las simulaciones de manera discreta.

En el Capítulo 3, analizamos la evolución de las variables fundamentales a lo largo de la vida de una fractura hidráulica, desde un gran retraso de fluido hasta uno pequeño, y abordamos varios regímenes de propagación. Este análisis es crucial para establecer parámetros de simulación de manera precisa. Además, exploramos la validez de un comportamiento universal aproximado que fue descrito previamente por Garagash (2006b) para los regímenes de tiempo temprano y tardío, y extendemos el resultado a una región más amplia en el dominio de los parámetros del sistema. También proporcionamos límites temporales cuantitativos para la aplicabilidad de cada régimen de propagación y un método para el mapeo cuantitativo de cantidades relacionadas.

En el Capítulo 4, presentamos un estudio sistemático para identificar factores de control en la interacción entre una fractura hidráulica y una fractura natural. Descubrimos que en el régimen con retraso de fluido, el modo de interacción está controlado por la tracción crítica y esencialmente independiente de la energía de fractura. Sin embargo, en el régimen sin retraso de fluido, los resultados no muestran una tendencia clara, y el modo de interacción depende en cierta medida del tipo de malla y del incremento de tiempo. Estos resultados resaltan la necesidad esencial de soluciones de referencia para la interacción en condiciones simplificadas.

El problema de encontrar soluciones de referencia para la interacción entre una fractura hidráulica en propagación y una fractura natural se divide en dos casos: desviación de la fractura hidráulica hacia la fractura natural (kink-in) y desviación fuera de la fractura natural (kink-out). Desafortunadamente, no hay soluciones analíticas conocidas para ninguno de los casos. En el Capítulo 5, nos enfocamos en el primer problema y comenzamos con el caso de propagación de fracturas en seco. Incluso en este caso, no hay soluciones analíticas, pero algunos estudios numéricos contribuyen al cuerpo de conocimientos sobre posibles soluciones de referencia.

Finalmente, en el Capítulo 6, proponemos un nuevo algoritmo de aceleración basado en la adaptación de la energía de fractura y lo probamos para simulaciones de fracturas hidráulicas con fracturas naturales.

Chapter 3

Propagation regimes and transition times in 2D hydraulic fracture

This chapter, with minimal modifications, was published as (Gutiérrez and Serebrinsky, 2021)

3.1 Introduction

Fluid-driven fracturing is a phenomenon involved in a variety of geoscience and civil engineering problems and applications. These include magma-driven cracks (Spence and Turcotte, 1985; Rubin, 1995), soil remediation (Murdoch, 2002; Frank and Barkley, 2005), carbon sequestration (Rudnicki, 2000) and cave preconditioning (As and Jeffrey, 2000). It has even been linked recently to biological processes (Arroyo and Trepat, 2017). But perhaps the most relevant application is in the stimulation of hydrocarbon reservoirs (fracking), mostly unconventional, to enhance productivity to economical levels (Economides and Nolte, 2000). Reservoir stimulation may be even associated with carbon sequestration (Middleton et al., 2014). Hydraulic fracking has also been proposed for enhanced geothermal systems (EGSs) (Legarth et al., 2005; Breede et al., 2013), the Habanero Project in Australia probably being the most prominent as of today.

From the standpoint of modeling and simulation, a variety of approaches are found in the literature. Analytical and semi-analytical solutions were developed for simple cases like straight cracks propagating in 2D (Geertsma and De Klerk, 1969; Detournay, 2004). These solutions provide significant qualitative and quantitative insight into the process, set a reliable benchmark for comparison, and guide the development of other techniques like Finite Elements (Kresse et al., 2013; Giovanardi et al., 2020), Extended Finite Elements (Salimzadeh and Khalili, 2015), Displacement Discontinuity Method (Wu and Olson, 2015), etc., that can deal with more complex cases, including simultaneous and/or interacting fractures. When using the analytical solutions as a benchmark for other calculations, it is essential to ensure that the hypotheses involved correspond with each other. Similarly, analyses were performed for penny-shaped cracks propagating in 3D (Spence et al., 1985; Detournay, 2016), which also served as benchmarks for more complex simulations Sousa et al. (1993).

Two dimensional models typically provide an easier ground to look for analytical or numerical solutions than the three dimensional counterparts, capturing many of the common essential features but also at the expense of a poorer or different description of other phenomena. For instance, when dealing with the interaction between an incident hydraulic fracture and a preexisting fracture, 2D models can account for the effect of remote stresses and interaction angle (Serebrinsky et al., 2017; Celleri et al., 2018), but they cannot provide for the mechanism of bypassing the fracture by surrounding it.

Another case in point, which relates specifically to the topic of the present work, is the analysis of the complete lifetime of a straight propagating crack, when a region about the crack tip not invaded by the fluid is allowed for. This analysis is crucial for setting up simulation parameters accurately. This so-called fluid lag was the subject of some debate in the literature since the proposal by Khristianovic and Zheltov (Khristianovic and Zheltov, 1955; Geertsma and De Klerk, 1969). Later on, it was directly observed in the laboratory (Medlin and Masse, 1984; Bunger et al., 2005), where a low confining stress that promotes the existence of a sizable fluid lag was applied. This was also observed in field experiments (Warpinski, 1985). The evolution of a plane strain fracture with fluid lag is known to be controlled by two non-dimensional parameters, only one of which evolves in time (Zhang et al., 2005; Garagash, 2006a). In connection with this parameter, a time scale can derived. On the other hand, the evolution of a penny-shaped crack with fluid lag is controlled by two evolutionary parameters, which in turn give rise to two different time scales (Bunger and Detournay, 2007). This phenomenology is well understood at this point. Nevertheless, few models endeavored inclusion of the fluid lag, either under rather controlled circumstances as straight propagation (Zhang et al., 2005; Garagash, 2006a;

Lecampion and Detournay, 2007; Bunger and Detournay, 2007) or under more general conditions (Hunsweck et al., 2013; Shen, 2014; Vahab and Khalili, 2018; Smilovich et al., 2021). Overall, results for the 3D case are scarcer than those for 2D.

Several works have provided before solutions that can be used as practical methods to evaluate the evolution of some variables (Geertsma and De Klerk, 1969), including their usage as a starting point for more elaborate solutions (Garagash, 2006a). In particular, Garagash (2006a) focused on the early-time of the fracture life. In the same spirit, we perform here an analysis of the evolution of the fundamental variables across the whole life of a fracture, covering the range from large to small fluid lag with various propagation regimes. We explore the validity of an approximate universal behavior, which was described before exclusively for the early and late time regimes (Garagash, 2006a). We extend here the result to a larger region in the domain of system parameters. In addition, we provide quantitative time bounds for the applicability of each of the propagation regimes, and a method for the quantitative mapping of related quantities.

In Sec. 3.2 we describe the basic equations of the model, which are in line with standard literature. In Sec. 3.3 we present some essential results on the structure of the solution that motivates the analysis of this paper, shown in Sec. 3.4. In Sec. 3.5 we summarize the conclusions.

3.2 Hydraulic fracture model

A 2D hydraulic fracture is allowed to propagate in a straight line, normal to the confining stress σ_0, under plane strain conditions, as shown in Fig. 3.1a. The medium is considered homogeneous and isotropic linearly elastic with Young modulus E, Poisson ratio ν, and mode I fracture toughness K_{Ic}. Other fracture modes and corresponding toughness values are not relevant under the present hypotheses, although they may be relevant for problems with deflecting cracks. An incompressible newtonian fluid with viscosity μ is injected at a constant rate Q, producing a symmetric crack with half-wing length ℓ and opening profile w by pressurizing the crack with the fluid pressure p_f. Fluid is not allowed to leak off into the solid, and a region about the crack tips where fluid is absent is considered. The fluid lag region between the fluid front at ℓ_f and the crack front is assumed to have no pressure. For most cases of interest, the actual pressure can be neglected as compared to σ_0.

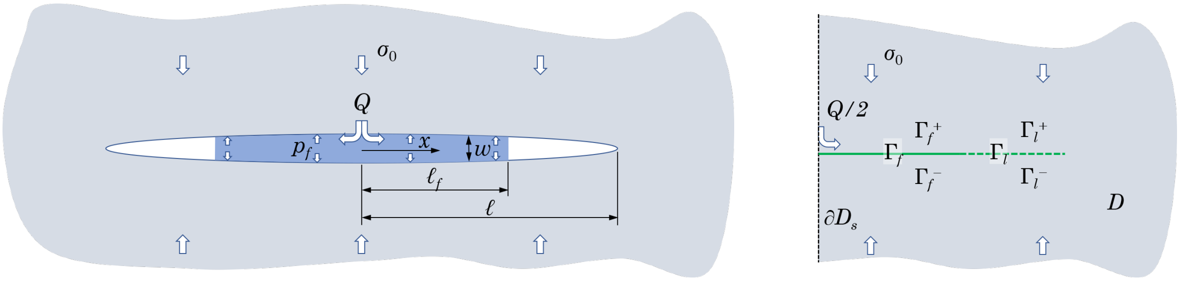

(a) Schematics of a symmetric 2D hydraulic fracture, including the fluid lag.

(b) Half-infinite model and notation.

Figure 3.1: Hydraulic fracture model.

The solution of the (symmetric) problem consists of finding the time evolution of the following quantities: $\ell(t)$, $\ell_f(t)$, $w(x,t)$ in Γ, and $p(x,t)$ in Γ_f, where x is the distance from the fluid inlet, $\Gamma_f = [0, \ell_f]$ is the fluid domain, $\Gamma_l = [\ell_f, \ell]$ is the fluid lag, $\Gamma = \Gamma_f \cup \Gamma_l = [0, \ell]$ is the crack domain, and $p = p_f - \sigma_0$ is the net pressure, which drives crack propagation. Each interface domain has its corresponding top (+) and bottom (−) counterparts in the solid. The stress $\boldsymbol{\sigma}$, strain $\boldsymbol{\varepsilon}$ and displacement $\mathbf{u}$ distributions in the solid D are not of interest as part of the solution in many cases, although depending on the method used to solve the problem they might be computed and available. The following parameters are usually considered, which allow for a cleaner formulation of the equations

$$E' = \frac{E}{1-\nu^2} \quad , \quad K' = 4\left(\frac{2}{\pi}\right)^{1/2} K_{Ic} \quad , \quad \mu' = 12\mu \quad . \tag{3.1}$$

3.2.0.1 Elasticity

The general elasticity equations for the semi-infinite domain of Fig. 3.1b are

$$\left\{ \begin{array}{rcll} \nabla \cdot \boldsymbol{\sigma} & = & \mathbf{0} & \text{in } D \\ \boldsymbol{\sigma} \cdot \mathbf{n} & = & -p\mathbf{n} & \text{on } {\Gamma_f}^+ \cup {\Gamma_f}^- \\ \boldsymbol{\sigma} \cdot \mathbf{n} & = & \mathbf{0} & \text{on } {\Gamma_l}^+ \cup {\Gamma_l}^- \\ \mathbf{u} \cdot \mathbf{n} & = & 0 & \text{on } \partial D_s \\ \mathbf{t} \cdot \boldsymbol{\sigma} \cdot \mathbf{n} & = & 0 & \text{on } \partial D_s \\ \mathbf{u} & = & \mathbf{0} & \text{for } r \to \infty \end{array} \right. \tag{3.2}$$

$$\boldsymbol{\sigma} = E\boldsymbol{\varepsilon} \tag{3.3}$$

$$\boldsymbol{\varepsilon} = \operatorname{sym}(\nabla \mathbf{u}) \quad , \tag{3.4}$$

where $\Gamma_s = \partial D_s$ is the symmetry line. The mechanics convention (and not the geomechanics convention) for the stresses is implied, namely, compression stress is negative. Note that, due to symmetry, one quarter of the domain is also enough to describe the problem. For our specific case of an infinite, homogeneous and lineal elastic isotropic solid, alternative integral formulations to relate p and $w = [\![\mathbf{u}]\!] \cdot \mathbf{n} = (\mathbf{u}|_{\Gamma^+} - \mathbf{u}|_{\Gamma^-}) \cdot \mathbf{n}$ are available ($[\![\cdot]\!]$ is the jump operator), e.g., Detournay (2004). Numerical methods can embody both formulations.

3.2.1 Crack propagation

It is assumed that crack propagates under the hypotheses of LEFM (Kanninen and Popelar, 1985). Therefore, the applied stress intensity factor is always just enough to keep the crack running

$$K = K_{Ic} \quad . \tag{3.5}$$

This implies the following asymptotic condition in the fracture about the crack tip

$$w \sim \frac{K'}{E'}(\ell - x)^{1/2} \quad \text{for } (\ell - x) \ll \ell \quad . \tag{3.6}$$

3.2.2 Cohesive zone model

The concept of cohesive zone modeling came from the original work of Dugdale (1960) and Barenblatt (1962). The objective of these works was different, but the final result was the same: the stress singularity about the crack tip in an elastic body was removed. Instead of dissipating the whole fracture energy at a mathematical crack tip and instantaneously as soon as the crack opens, as dictated by LEFM, the fracturing process is replaced by a gradual decohesion between the separating crack faces. Such process now takes place across a cohesive zone with a finite size ℓ_c, as illustrated in Fig. 3.2a. The cohesive length is the distance from the crack tip, where interface tractions have just essentially vanished, to the point where the decohesion process is just starting. Often times, the maximum cohesive traction is attained close to or at this point.

The interface bonding can be regarded as a distribution of tractions that vary across the cohesive zone as a function of the separation between the two surfaces, according to a traction-separation law (TSL) $\boldsymbol{T} = \boldsymbol{T}(\boldsymbol{\Delta}, \boldsymbol{\zeta})$. This constitutive behaviour relates the separation $\boldsymbol{\Delta}$ and the traction $\boldsymbol{T}$ across the faces of the cohesive zone, incorporating

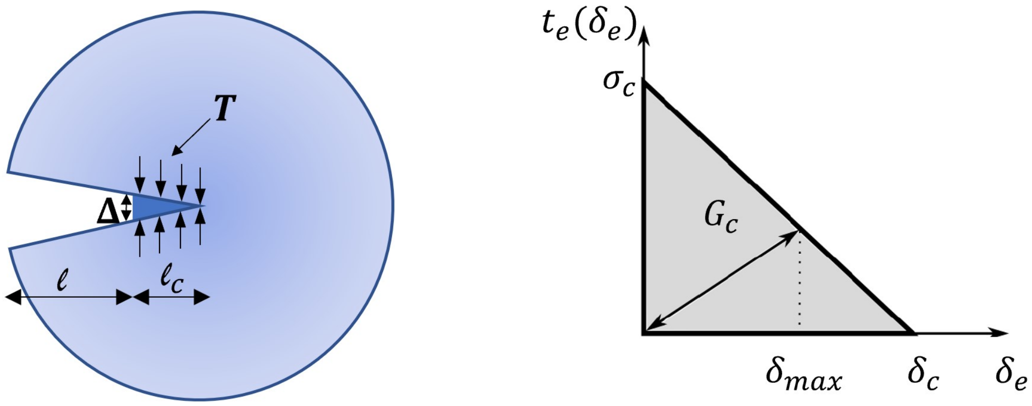

(a) Scheme of a cohesive fracture. Cohesive traction, fracture length ℓ, cohesive length ℓ_c and separation can be identified.

(b) Triangular traction-separation law scheme. Cohesive effective traction t_e on the x-axis and effective separation (δ_e) on the y-axis. Fracture energy G_c is the area under the traction-separation law, critical traction is σ_c and critical separation is δ_c.

Figure 3.2: Cohesive Model Description.

a suitable set $\boldsymbol{\zeta}$ of internal variables, which have their corresponding hardening laws. Similarly as in LEFM, such mathematical interface would typically embody a region with a finite width in actual materials, where energy dissipation takes place. Fig. 3.2b shows an often used example of a TSL.

For the decohesion process to advance, the local stress across the interface must attain the interface cohesive strength or critical traction (the peak stress in the traction separation law σ_c), and the total energy supplied to the crack tip must be equal to the interface toughness (the area under the traction-separation law, G_c). In other words, the toughness and strength criteria must be met simultaneously.

In terms of the normal and tangential components, we have

$$\boldsymbol{\Delta} = \delta_n \boldsymbol{n} + \delta_t \boldsymbol{m} \quad , \tag{3.7}$$

$$\boldsymbol{T} = t_n \boldsymbol{n} + t_t \boldsymbol{m} \quad . \tag{3.8}$$

We further specialize to an effective TSL $t_e(\delta_e, \boldsymbol{\zeta})$ between an effective traction t_e and an effective separation

$$\delta_e = \sqrt{\delta_n^2 + \beta^2 \delta_t^2} \quad , \tag{3.9}$$

also including $\boldsymbol{\zeta}$, where β is the mode weighting factor (Ortiz and Pandolfi, 1999). This typically implies that $\boldsymbol{T}$ can be derived from a potential, and

$$\boldsymbol{T} = \frac{t_e}{\delta_e}\left(\delta_n \boldsymbol{n} + \beta^2 \delta_t \boldsymbol{m}\right) \quad . \tag{3.10}$$

For the effective TSL we choose the usual linear softening irreversible law

$$t_e(\delta_e, \delta_{\max}) = \begin{cases} \sigma_c \left(1 - \dfrac{\delta_e}{\delta_c}\right) & \text{if } \dot{\delta}_e \geq 0 \text{ and } \delta_e = \delta_{\max} \quad , \\ \sigma_c \left(1 - \dfrac{\delta_{\max}}{\delta_c}\right) \dfrac{\delta_e}{\delta_{\max}} & \text{if } \dot{\delta}_e < 0 \text{ or } \delta_e < \delta_{\max} \quad . \end{cases} \tag{3.11}$$

shown in Fig. 3.2b. Here, σ_c is the critical traction for which the TSL becomes operational, and δ_c is the separation beyond which there is no further traction between the crack faces as observed in Fig. 3.2. The resulting fracture energy is

$$G_c = \frac{1}{2}\sigma_c \delta_c \quad . \tag{3.12}$$

Based on scaling arguments, it can be shown that this new characteristic length is

$$\ell_c = f_n \frac{E' G_c}{{\sigma_c}^2} = f_n \frac{{K_{Ic}}^2}{{\sigma_c}^2} \quad , \tag{3.13}$$

where we have used the relation

$${K_{Ic}}^2 = E' G_c \quad , \tag{3.14}$$

valid for the case of a single G_c value for any propagation mode. The numerical constant f_n depends on the shape of the cohesive law and the configuration of the sample. For instance, for a flat cohesive law and and infinite sample under plane stress loading (thus replacing E' with E), Dugdale (1960) gives the exact value $f_n = \pi/8 = 0.393$. In this work we use $f_n = 0.53$.

A more detailed explanation of the cohesive zone model described here can be found in Radovitzky et al. (2011) and Ortiz and Pandolfi (1999).

3.2.3 Lubrication

Upon assuming the lubrication approximation for the fluid flow in the fracture, the set of equations that provide the net pressure field are

$$\begin{cases} \frac{\partial q}{\partial x} & = & -\frac{\partial w}{\partial t} & \text{in } \Gamma_f \\ p & = & -\sigma_0 & \text{in } \Gamma_l \\ q & = & Q/2 & \text{at } x = 0 \\ \dot{\ell}_f & = & -\frac{w^2}{\mu'}\frac{\partial p}{\partial x} & \text{at } x = \ell_f \end{cases} \tag{3.15}$$

$$q = -\frac{w^3}{\mu'}\frac{\partial p}{\partial x} \quad , \tag{3.16}$$

which is cast in a form analogous to Eq. (3.2). No leak-off term is included here. The governing field equation that is derived from Eqns. (3.15) and (3.16) is the Reynolds lubrication equation

$$\frac{\partial w}{\partial t} = \frac{\partial}{\partial x}\left(\frac{w^3}{\mu'}\frac{\partial p}{\partial x}\right) \quad , \tag{3.17}$$

which does not contain the Couette part of the flow.

3.3 Scaling and solutions

A solution method is usually based on the scaling of the problem variables, recasting the equations into non-dimensional form. For this purpose, a length scale $L(t)$ and a small parameter $\varepsilon(t)$ are introduced, such that non-dimensional variables are

$$\text{Crack length: } \ell(t) = L(t)\gamma(t) \tag{3.18}$$

$$\text{Fluid length: } \ell_f(t) = L(t)\gamma_f(t) \tag{3.19}$$

$$\text{Net pressure: } p(x,t) = \varepsilon(t)E'\Pi(\xi,t) \tag{3.20}$$

$$\text{Opening: } w(x,t) = \varepsilon(t)L(t)\Omega(\xi,t) \quad , \tag{3.21}$$

where $\xi = x/\ell \in [0,1]$ is the non-dimensional location along the crack. In addition, the fluid fraction of the crack length is

$$\xi_f = \frac{\ell_f}{\ell} = \frac{\gamma_f}{\gamma} \quad , \tag{3.22}$$

This set of equations is an extension of that applied for the case of a fully invaded fracture (Detournay, 2004).

The factor ε is of the order of p/E', as per elasticity considerations. With these definitions, and yet-to-be-defined $L(t)$ and $\varepsilon(t)$, most of the non-dimensional variables would be typically of the order of 1. The approximate relation between average quantities is expected $\langle p\rangle/E' \sim \langle w\rangle/\ell_f$ (cf. $\langle p\rangle/E' \sim \langle w\rangle/\ell$ for a wet crack tip). If $L(t)$ is chosen as the approximate fluid length, Eq. (3.21) is implied.

Introducing the scaling equations into the field equations (Sec. 3.2), four non-dimensional groups emerge, along with the non-dimensionalized equations, which we will not reproduce here. Two of these groups can be arbitrarily set to one. This procedure yields generally the dependence of L and ε and two other non-dimensional parameters on the physical parameters and time. Two convenient choices are usually identified, called the "viscosity" and "toughness" scaling. Each of these is most useful when global energy dissipation is dominated by the viscosity of the fluid or the toughness of the solid, respectively. Subscripts m, k are usually added to various quantities to indicate that the viscosity or toughness scaling was selected. We will consider here the viscosity scaling, and we typically omit the subscript.

In the viscosity scaling we have

$$L(t) = \left(\frac{E'Q^3t^4}{\mu'}\right)^{1/6} \tag{3.23}$$

$$\varepsilon(t) = \left(\frac{\mu'}{E't}\right)^{1/3} \tag{3.24}$$

$$\mathcal{K} = \frac{K'}{E'^{3/4}Q^{1/4}\mu'^{1/4}} \tag{3.25}$$

$$\mathcal{T} = \frac{\sigma_0}{E'}\left(\frac{E't}{\mu'}\right)^{1/3} \quad , \tag{3.26}$$

where $\mathcal{K}$ is a non-dimensional toughness, and $\mathcal{T}$ is a non-dimensional remote stress. $\mathcal{T}$ was also called the non-dimensional tip underpressure, based on $\sigma_0 - p_{f(tip)}$, but the fact that the pressure in the fluid lag $p_{f(tip)}$ is typically negligible compared to σ_0 justifies the usual expression in Eq. (3.26). It is apparent in Eq. (3.25) that for the specific case of a 2D plane-strain fracture, the parameter $\mathcal{K}$ does not evolve in time, and $\mathcal{T}$ remains as the only evolutionary parameter. For a penny-shape crack this is not the case (Detournay, 2016).

Eq. (3.26) can be recast as

$$\mathcal{T} = \left(\frac{t}{t_{om}}\right)^{1/3} = \tau^{1/3} \quad , \tag{3.27}$$

where

$$t_{om} = \frac{E'^2 \mu'}{{\sigma_0}^3} \tag{3.28}$$

is a time scale for the propagation process and τ is a non-dimensional time.

The complete solution of the problem is given by the set $\mathcal{F} = \{\Omega, \Pi, \gamma_f, \xi_f\}$, which depends on $\mathcal{P} = (\mathcal{K}, \mathcal{T})$.

3.3.1 Parametric space and propagation regimes

The non-dimensional system parameters are $\mathcal{K} \in [0, \infty)$ and $\mathcal{T} \in [0, \infty)$. A schematic (quarter-infinite) rectangular parametric space $P = \{(\mathcal{K}, \mathcal{T})\} = [0, \infty) \times [0, \infty)$ can be envisioned, as shown in Fig. 3.3a. Nevertheless, the solution for $\mathcal{K} \to \infty$ was shown to be self similar for all $\mathcal{T}$, with a vanishingly small fluid lag $1 - \xi_f \sim 0.129 \exp\left(-\frac{3\pi}{32}\mathcal{K}^4\right)$ (Garagash, 2006a). Therefore, the prospective edge between the points $(\mathcal{K}, \mathcal{T}) = (\infty, 0)$ and $(\mathcal{K}, \mathcal{T}) = (\infty, \infty)$ degenerates into a point, named the K-vertex. The parameter space is then a triangle, with the two other vertices $O = (0, 0)$ and $M = (0, \infty)$, as shown in Fig. 3.3b and usually represented.

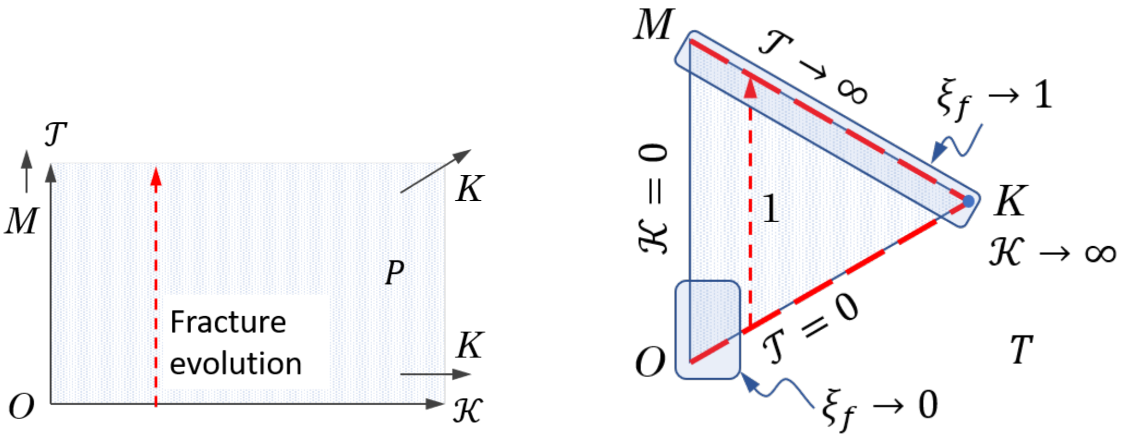

(a) Rectangular parametric space P for a 2D hydraulic fracture with fluid lag.

(b) Triangular parametric space for a 2D hydraulic fracture with fluid lag.

Figure 3.3: Parametric space for a 2D hydraulic fracture with fluid lag.

For low values of ξ_f, Garagash (2006a) obtained the implicit dependence of the fluid fraction on the two parameters $(\mathcal{K}, \mathcal{T})$

$$\left(\frac{9\pi}{56}\right)^{1/4} \left(\ln \frac{2}{\xi_f}\right)^{3/4} \frac{\mathcal{K}}{{\xi_f}^{1/2}} + \left(\frac{144\pi}{7}\right)^{1/3} \left(\ln \frac{2}{\xi_f}\right)^{2/3} \frac{\mathcal{T}}{\xi_f} = 1 \tag{3.29}$$

The central role played by Eq. (3.29) stems from the fact that, in the low ξ_f approximation, all quantities and fields (Ω, Π, etc.) in the boundary layer depend on a single variable, e.g., ξ_f. Given the assumption that the crack propagates under equilibrium conditions, the conclusion above also implies that the crack length is controlled by the same variable. The dependence is

$$\gamma = \frac{1}{\xi_f}\left(\frac{9\epsilon_f}{28}\right)^{1/6} \quad , \tag{3.30}$$

$$\Pi_0 = \frac{5}{6}\left(\frac{18\epsilon_f}{7}\right)^{2/3} \quad , \tag{3.31}$$

$$\Omega_0 = \left(\frac{7}{144\epsilon_f}\right)^{1/6} \quad , \tag{3.32}$$

where all quantities were written in terms of

$$\epsilon_f = \frac{\pi}{8\ln\left(2/\xi_f\right)} \quad . \tag{3.33}$$

Explicit expressions in terms of ξ_f can be obtained simply.

We analyze in the following section some variations and commonalities in the behavior of the fracture across the MKO triangle. The present work is not focused on the computational method itself but on the results describing the behaviour of the system. We used for most of our calculations the staggered algorithm for finite elements simulations described in detail in Smilovich et al., 2021, which was verified against known solutions. In addition, we have also performed evaluations based on the equations presented by Garagash, 2006a , and obtained some data from Lecampion and Detournay, 2007 . Unless relevant, we omit specification of the method used for obtaining each of the reported results, as they are in line with each other.

As we provide a comparison of the behavior among early, intermediate and late time regimes, and we suggest a practical application, it is most relevant to identify specific time bounds for the development of each regime. This is in contrast with the usual application of a time scale t_{om} (Eq. (3.28)) to describe solely limiting conditions in the form, e.g., $t \ll t_{om}$, or similarly for a penny-shaped crack (Bunger and Detournay, 2007). Analogous identifications for transition times were more frequently carried out for the bounds in $\mathcal{K}$ for viscosity or toughness dominated propagation regimes, in plane strain (Detournay, 2004) and penny shaped hydraulic fractures (Savitski and Detournay, 2002).

3.4 Present results and discussion

Fig. 3.4 shows the general form of the evolution of the fluid fraction with $\mathcal{T}$, for a range of $\mathcal{K}$ values. For low $\mathcal{K}$ values (up to about $\mathcal{K} = 0.05$), Eq. (3.29) can be used. According to the hypothesis involved in its derivation, we expect the computed ξ_f to be accurate at low values. Note that the evolution for $\mathcal{K} = 0$ acts as an envelop of all curves.

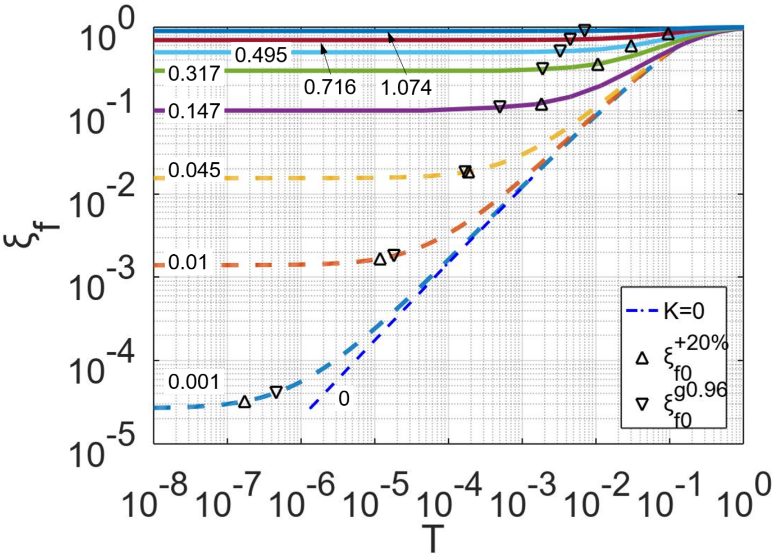

Figure 3.4: Evolution of the fluid fraction ξ_f for a range of $\mathcal{K}$ values. Dashed lines: $\mathcal{K} < 0.05$, Eq. (3.29). Solid lines: $\mathcal{K} > 0.05$, data from the work of Lecampion and Detournay (2007). Symbols: $\triangle$, ∇: two possible threshold values for the onset of the intermediate regime, see text.

We first provide specific parametrizations of the schematic parametric space (Fig. 3.3), which allow for a quantitative (instead of qualitative) representation of data. Then we analyze conditions for the transition among regimes, taking advantage of the parametrization. Finally we evaluate the approximate universality proposed, focusing on the intermediate regime.

3.4.1 Parametrization of the MKO diagram

Representation of data in the corresponding parametric space (Fig. 3.3 here) is often performed in a qualitative manner. Such data is typically the path traced by the history of a propagating crack, but it could also be the locus of some specific condition, e.g., threshold $(\mathcal{K}, \mathcal{T})$ conditions for the transition among propagating regimes. We propose here a quantitative parametrization of the MKO diagram which allows for a more definite representation.

A transformation between P (Fig. 3.3a) and the MKO triangle (Fig. 3.3b) can be carried out by considering the intermediate variables $\bar{\mathcal{K}} = (\log \mathcal{K} + b_k)/a_k$ and $\bar{\mathcal{T}} = (\log \mathcal{T} + b_t)/a_t$, with $\bar{\mathcal{P}} = (\bar{\mathcal{K}}, \bar{\mathcal{T}}) \in \bar{P} = (-\infty, \infty) \times (-\infty, \infty)$. This intermediate transformation "symmetrizes" the prevalence in the parameter space of low vs. high values of $\mathcal{K}$ and $\mathcal{T}$. Equivalently, it symmetrizes the prevalence of M vs. K, and M vs. O, vertex behavior. The arbitrary constant a_k controls the prevalence of limiting (OM edge and K vertex) vs. transient behavior in the representation, in terms of $\mathcal{K}$. Similarly, a_t controls the prevalence of limiting (OK and MK edges) vs. transient behavior in terms of $\mathcal{T}$. Constants b_k and b_t control the $(\mathcal{K}, \mathcal{T})$ values that would appear centered in the triangle. A second intermediate transformation that preserves the symmetrization above, and which leads to the rectangle $P^* = [0, 1] \times [0, 1]$, is given by

$$\mathcal{K}^* = \frac{1}{2} + \frac{1}{\pi} \tan^{-1}\left(\bar{\mathcal{K}}\right) = \frac{1}{2} + \frac{1}{\pi} \tan^{-1}\left(\frac{1}{a_k}(\log \mathcal{K} + b_k)\right) \quad , \tag{3.34}$$

$$\mathcal{T}^* = \frac{1}{2} + \frac{1}{\pi} \tan^{-1}\left(\bar{\mathcal{T}}\right) = \frac{1}{2} + \frac{1}{\pi} \tan^{-1}\left(\frac{1}{a_t}(\log \mathcal{T} + b_t)\right) \quad , \tag{3.35}$$

Other alternatives for this four-parameter family of transformations can be considered, preserving the symmetrization above or not.

The "symmetric" choice $\mathcal{M}^* = 1 - \mathcal{K}^*$ leads to

$$\mathcal{M}^* = \frac{1}{2} + \frac{1}{\pi} \tan^{-1}\left(\bar{\mathcal{M}}\right) = \frac{1}{2} + \frac{1}{\pi} \tan^{-1}\left(\frac{1}{a_m}(\log \mathcal{M} + b_m)\right) \quad , \tag{3.36}$$

with $a_m = 4a_k$ and $b_m = -4b_k$. The MKO triangle $T = \{(x, y)\}$ can be obtained from P^* trivially with, e.g.,

$$x = \frac{\sqrt{3}}{2}\mathcal{K}^* \quad , \quad y = \frac{1}{2} + (1 - \mathcal{K}^*)(\mathcal{T}^* - \frac{1}{2}) \quad . \tag{3.37}$$

Thus, equations (3.34), (3.35) and (3.37) provide a four-parameter family of parametrizations of the MKO triangle with specific symmetry properties between early/late time and viscosity/toughness regimes, and therefore physically motivated. Fig. 3.6 below illustrates the effect of the four parameters on the representation of data (cf. Fig. 3.5b). Note that this could be also used for the mapping of propagating penny shaped hydraulic fractures. Analogous parametrizations, with similar symmetry properties, could also be taken advantage of when analyzing results over domains representing other physical phenomena.

3.4.2 Propagation regimes and transition times

The life of the propagating hydraulic fracture can be divided into three regimes: early, intermediate or transient, and late time. Correspondingly, two different transition times can be evaluated, one as an upper limit for the approximate validity of the early time solution t_{ei}, and another as a lower limit for the approximate validity of the late time solution t_{il}. The time scale t_{om} might provide a reference value for the transition times, as often used, but it is insufficient per se for practical applications. Little attention has been devoted in the literature to the variation of both transition times, and this section helps bridging that gap.

In the early time regime, the fluid fraction remains constant in time at $\xi_{f,OK}(\mathcal{K})$, and the crack propagates with its corresponding fields evolving self-similarly. The time scale for the onset of the intermediate regime t_{ei} was derived before from the consideration of a small value of the non-dimensional remote stress $\mathcal{T} \ll 1$ (Garagash, 2006a; Hunsweck et al., 2013). In particular, a limit $\mathcal{T} \leq \mathcal{T}_{ei} = 0.01$ was chosen (Garagash, 2006a), which implies

$$t \leq t_{ei} \approx 10^{-6} \frac{\mu' E'^2}{{\sigma_0}^3} \; . \tag{3.38}$$

Nevertheless, according to Fig. 3.4, it is apparent that a constant value of $\mathcal{T}_{ei}$ is unable to capture the transition point for all values of $\mathcal{K}$. We computed alternative, $\mathcal{K}$-dependent threshold values, as shown in Figs. 3.4 and 3.5, in both the usual representation and in the parametrization proposed in Sec. 3.4.1, here with $a_k = 0.5$, $a_t = 2$, $b_k = 0$ and $b_t = 1$.

Two options were considered here. The first criterion is based on the time at which the fluid fraction ${\xi_f}^{+20\%}(\mathcal{K})$ is 20% larger than the early-time value $\xi_{f,OK}(\mathcal{K})$. This threshold can be fit for low $\mathcal{K}$ as

$${\mathcal{T}_{ei}}^{+20\%}(\mathcal{K}) = 0.0554 \; \mathcal{K}^{1.84} \; . \tag{3.39}$$

For increasing values of $\mathcal{K}$ this threshold loses its meaning, as ${\xi_f}^{+20\%}$ approaches 1. Moreover, for $\mathcal{K} > (1/1.2)$ it does not even exist.

An alternative threshold which can be used for all values of $\mathcal{K}$ is given by a weighted geometric mean between $\xi_{f,OK}(\mathcal{K})$ and $\xi_{f,MK}(\mathcal{K}) = 1$. For a weight of 0.96 this fluid fraction is ${\xi_f}^{g0.96}(\mathcal{K}) = (\xi_{f,OK}(\mathcal{K}))^{0.96}$, and the corresponding threshold is

$${\mathcal{T}_{ei}}^{g0.96}(\mathcal{K}) = 0.0218 \; \mathcal{K}^{1.55} \; . \tag{3.40}$$

A simplified threshold can also be obtained considering the $\mathcal{K} = 0$ curve in Fig. 3.4

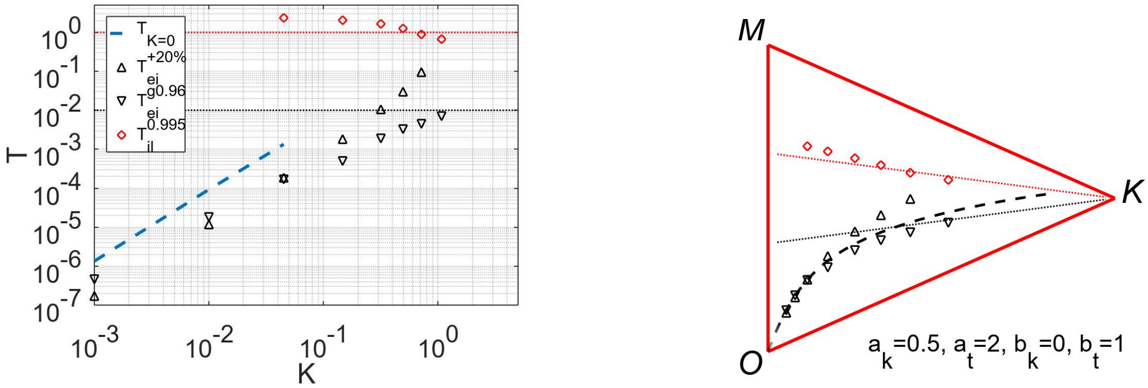

(a) Usual representation .

(b) MKO representation of data in Fig. 3.5a, as per Sec. 3.4.1. A plot of Eq. (3.40) (beyond its applicability region) is included instead of Eq. (3.44), for illustration purposes.

Figure 3.5: $\mathcal{K}$-dependent threshold values of the non-dimensional remote stress, for the transition between early and intermediate times $\mathcal{T}_{ei}$ and between intermediate and late times $\mathcal{T}_{il}$. Symbols: △ and ▽ are two threshold values for the intermediate regime. The first one, based on the time at which the fluid fraction $\xi_f{}^{+20\%}(\mathcal{K})$ is 20% larger than the early-time value $\xi_{f,OK}(\mathcal{K})$. The second, based on the weighted geometric mean (for a weight of 0.96) between $\xi_{f,OK}(\mathcal{K})$ and $\xi_{f,MK}(\mathcal{K}) = 1$.

as an approximate intermediate regime behaviour for all $\mathcal{K}$. Thus, for each $\mathcal{K}$ value the intersection between the early time and this approximate intermediate behavior signals the transition to the intermediate regime,

$$\xi_{f,OK}(\mathcal{K}) = \xi_{f,OM}(\mathcal{T}) \quad . \tag{3.41}$$

For low ξ_f, (3.29) reduces to

$$\xi_{f,OK}\left(\mathcal{K}\right) = 2\left[\tilde{\mathcal{K}}^{-1}\mathcal{W}\left(\tilde{\mathcal{K}}\right)\right]^{3/2} \quad \text{with } \tilde{\mathcal{K}} = \left(\frac{243\pi}{1792}\right)^{-1/3}\mathcal{K}^{-4/3} \tag{3.42}$$

and

$$\xi_{f,OM}\left(\mathcal{T}\right) = 2\left[\tilde{\mathcal{T}}^{-1}\mathcal{W}\left(\tilde{\mathcal{T}}\right)\right]^{2/3} \quad \text{with } \tilde{\mathcal{T}} = \left(\frac{8\pi}{7}\right)^{-1/2}\mathcal{T}^{-3/2} \quad , \tag{3.43}$$

where $\mathcal{W}$ is the Lambert product logarithm function. Eqs. (3.41), (3.42) and (3.43) lead to

$$\mathcal{T}_{\mathcal{K}=0}(\mathcal{K}) = 0.381\ \mathcal{K}^{1.82} \ , \tag{3.44}$$

which is about 7 times larger than $\mathcal{T}_{ei}{}^{+20\%}$. Regardless of the choice, any of these values provides an apparently better option for t_{ei} than $\mathcal{T}_{ei} = 0.01$.

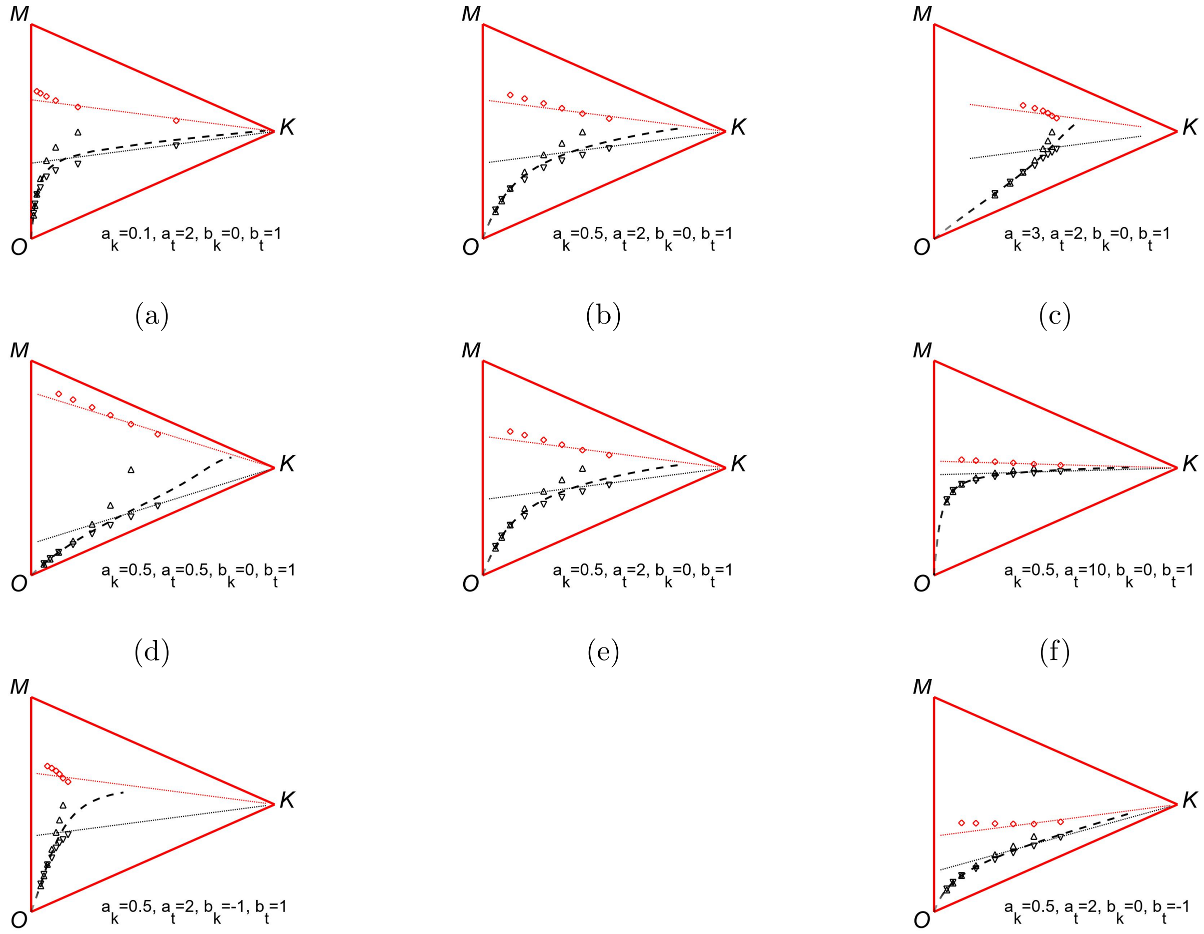

(a) (b) (c)

(d) (e) (f)

(g) (h)

Figure 3.6: Effect of the parameters of the transformation $P \to T$ on the resulting loci, cf. Fig. 3.5b. Increasing a_k: first row (a), (b), (c); increasing a_t: second row (d), (e), (f); increasing b_k: (g), (e); increasing b_t: (h), (e).

As for the time scale t_{il}, it was quoted as (Lecampion and Detournay, 2007; Hunsweck et al., 2013)

$$t_{il} \approx \frac{\mu' E'^2}{{\sigma_0}^3} \quad ; \quad \mathcal{T}_{il} \approx 1 \ . \tag{3.45}$$

Fig. 3.5 includes the more accurate values of $\mathcal{T}_{il}$ computed numerically at a threshold $\xi_f = 0.995$ (Lecampion and Detournay, 2007). It is worth noting that at $\mathcal{K} = 1$ the intermediate time regime spans about one order of magnitude in $\mathcal{T}$. For increasing $\mathcal{K}$, both early and late time regimes converge, and the concepts of intermediate regime and transition times become ill-defined.

We analyze in the following the variation of $\mathcal{F}_0 = \mathcal{F}(\xi = 0) = \{\Omega_0, \Pi_0, \gamma, \xi_f\}$, with a focus on this intermediate regime.

3.4.3 Intermediate regime and approximate universality

As mentioned above, both early and late time evolutions in $\mathcal{F}_0$-space lay essentially on a single curve $\mathcal{C}$. This was already pointed out by Garagash (2006a), albeit the reduced space $\tilde{\mathcal{F}}_0 = \{\Omega_0, \Pi_0, \gamma\}$ was specified. It was also suggested that this universality would not apply for the transient regime, below a threshold $\mathcal{K} \approx 1.31$. We consider here the departure from $\mathcal{C}$ of the evolution during this transient. If such departure is small, then $\mathcal{C}$ can be taken as a reasonable approximation of the complete propagation history. The analysis is based on the consideration of projections of $\mathcal{F}_0$ on pairwise relations between the main variables.

Fig. 3.7 shows some relations between those variables. We describe here the contents of each of the figures. Solid lines (blue in color) represent the self-similar solution on the MK edge. Dotted lines (red in color) represent the numerically computed self-similar solution on the OK edge (Garagash, 2006a). In each of the figures, the overlapping part of these two curves correspond to $\mathcal{K} \gtrsim 1.3$. The opposite extreme of the OK curves correspond to the limit $\mathcal{K} \to 0$. Dashed lines (cyan in color) represent the asymptotic solution in the vicinity of the O vertex, see Sec. 3.2. Symbols (several colors) represent calculations performed in the present work, with the method described in the work of Smilovich et al. (2021). In Fig. 3.7a, symbols were replaced by trend lines (colors matching substituted symbols) for an easier visualization. Long/short dashed lines (green in color) represent the numerically computed values for $\mathcal{K} = 0.317$ (Lecampion and Detournay, 2007), which closely match our calculations for the same $\mathcal{K}$.

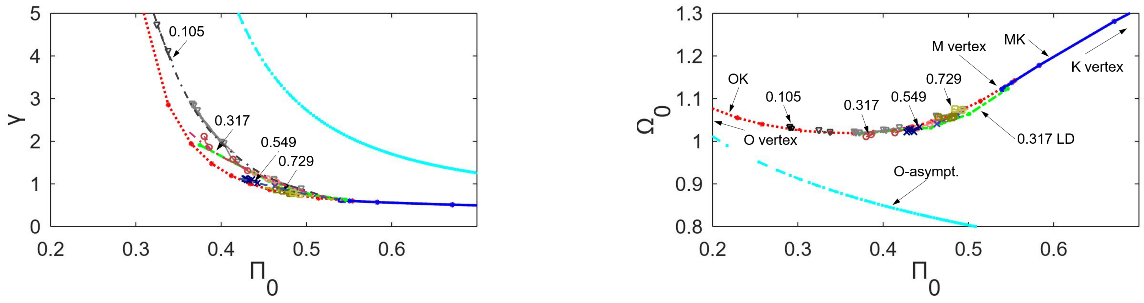

(a) Non-dimensional length γ vs. non-dimensional pressure Π_0 at the inlet. Dash-dotted lines: trend lines in lieu of data points from data calculated here, for a more convenient visualization.

(b) Non-dimensional opening Ω_0 vs. non-dimensional pressure Π_0, at the inlet.

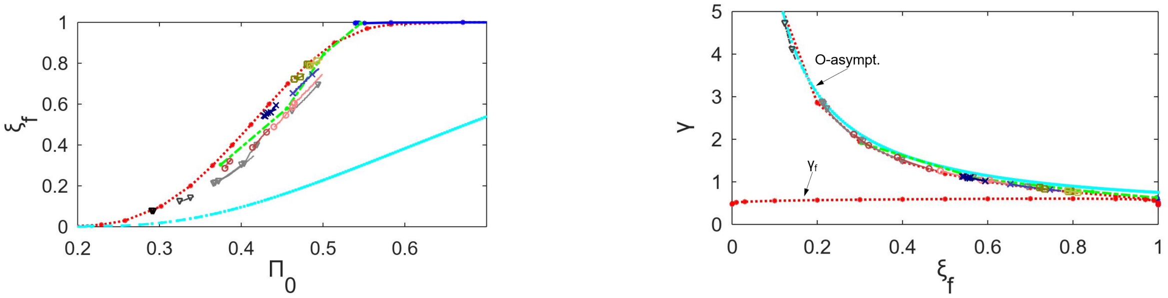

(c) Fluid fraction ξ_f vs. non-dimensional pressure Π_0 at the inlet.

(d) Non-dimensional length γ vs. fluid fraction ξ_f. The non-dimensional fluid length γ_f is included as a reference.

Figure 3.7: Relation between non-dimensional quantities in $\mathcal{F}_0$. Dotted line: self-similar OK edge solution Garagash (2006a). Solid line: self-similar MK edge solution Lecampion and Detournay (2007), overlapping the OK solution. Dashed line: transient OK→MK solution for $\mathcal{K} = 0.317$ Lecampion and Detournay (2007). Symbols: transient OK→MK solution for several $\mathcal{K}$ values, calculated here; $\triangledown$ 0.105, $\circ$ 0.317, $\times$ 0.549, $\square$ 0.729. Our data essentially overlaps data from Lecampion and Detournay (2007) for $\mathcal{K} = 0.317$. Dashed line: asymptotic solution for the O-vertex.

A few points can be gleaned from the figure, as follows. For Ω_0 vs. Π_0 and γ vs. ξ_f, the relations appear essentially collapsed onto a single curve, down to at least $\mathcal{K} = 0.1$. This is well below the threshold quoted above. We considered the respective asymptotic solutions for the O vertex. These would apply as a possible bound for the departure of the trajectory in $\mathcal{F}_0$-space from $\mathcal{C}$, in particular for low $\mathcal{K}$. It is remarkable that in the case of γ vs. ξ_f the O-asymptote almost overlaps the OK edge curve, thus providing an explanation for the universality observed. Moreover, the overlap covers the whole ξ_f range, which is somewhat unexpected given the O-asymptote applies essentially for low ξ_f values. It remains to be clarified whether these findings are somewhat fortuitous, or they have a physical basis. A similar analysis for Ω_0 vs. Π_0 would not justify the approximate universality observed. It is not clear at this point whether this lower bound is not strict (even far from the M vertex), or it would be rigorously attained for lower $\mathcal{K}$ values.

As for γ vs. Π_0 and ξ_f vs. Π_0, the deviations are more marked, even though still moderate. In both cases, it appears that lowering $\mathcal{K}$ further below 0.1 keeps shifting both relations closer to the O-asymptote. From all the data just analyzed it appears that the relation in $\mathcal{F}_0$-space that applies for the OK and MK edges is also a good approximation for the transient regime, at least for $\mathcal{K} \gtrsim 0.3$, and possibly above 0.1. The usability of such an approximation for specific cases (numerical program + physical conditions) was not evaluated.

Nevertheless, as an exercise and assuming estimations from the plane strain model are applicable, consider a reservoir with $E = 30\,\mathrm{GPa}$, $\nu = 0.25$, $G_c = 60\,\mathrm{Pa\,m}$, and a stimulation treatment with $\mu = 0.013\,\mathrm{Pa}$, flow $Q = 0.02\,\mathrm{m}^3/\mathrm{s}$. Then, the non-dimensional variables are $\mathcal{K} \approx 0.44$, $\xi_{f,OK} \approx 0.44$, $\gamma_{OK} = 1.35$, $\gamma_{f,OK} = 0.59$, and the transition times are $\tau_{ei} \approx 1.3 \times 10^{-7}$ and $\tau_{il} \approx 3.4$. With these values, the dimensional conditions at the two transition points are $t_{ei} \approx 20\,\mathrm{ns}$, $\ell_{ei} \approx 80\,\mu\mathrm{m}$, $t_{il} \approx 0.5\,\mathrm{s}$, $\ell_{il} \approx 7.2\,\mathrm{m}$. So, if one wanted to start a simulation at any time below t_{il}, the present results indicate the approximate universal curves provide reasonable initial conditions for the simulations, even if out of the OK edge.

Fig. 3.8 provides a complementary appraisal, showing the variation of several quantities which, according to Sec. 3.3, are expected to be of the order of 1. Fig. 3.8b shows what we call here the (non-dimensional) total and fluid volume ratios

$$\lambda = \frac{2\ell w_0}{Qt} = 2\gamma\Omega_0 \quad , \quad \lambda_f = 2\gamma_f\Omega_0 \quad . \tag{3.46}$$

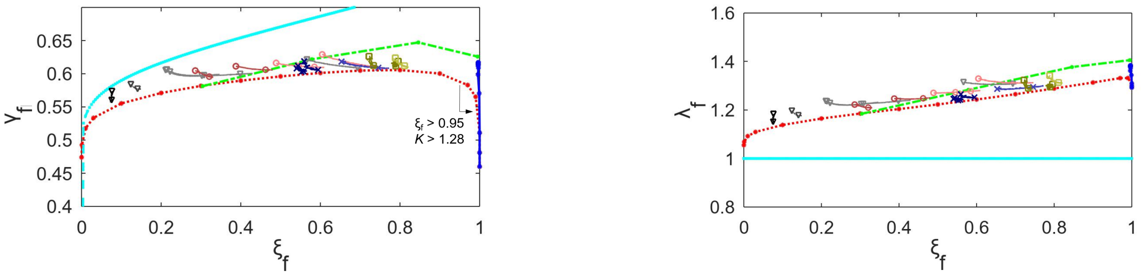

(a) Non-dimensional fluid length γ_f vs. fluid fraction ξ_f.

(b) Non-dimensional fluid volume ratio λ_f vs. fluid fraction ξ_f.

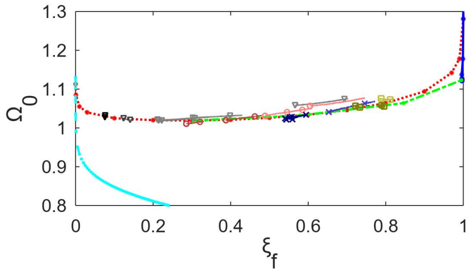

(c) Non-dimensional opening at the inlet Ω_0 vs. fluid fraction ξ_f.

Figure 3.8: Relation between non-dimensional quantities derived from $\mathcal{F}_0$. References are the same as in Fig. 3.7.

It is seen that the O-asymptote value of λ_f is exactly 1, according to the scaling selected. The milder variation of both γ_f and λ_f across the whole range of ξ_f, as compared to Π_0 (cf. Fig. 3.7c), is in line with the description above.

3.5 Conclusions

The problem of a two-dimensional hydraulic fracture propagating in an elastic medium, with consideration of the fluid lag, was analyzed. It is known that the life of such a crack spans three distinct regimes, early, transient and late time, each covering a different part of the MKO triangle. The focus here was on the possible relations among the essential variables that describe the crack configuration, that is $\mathcal{F}_0 = \{\Omega_0, \Pi_0, \gamma, \xi_f\}$, across the three regimes and for the whole range of the non-dimensional toughness $\mathcal{K}$.

The first finding was a $\mathcal{K}$-dependent value $\mathcal{T}_{ei}(\mathcal{K})$ for the transition from early to transient regime. This, along with the transition value from transient to late time regime $\mathcal{T}_{il}(\mathcal{K})$, provides a more clear picture of the actual regime for any $\mathcal{P} = (\mathcal{K}, \mathcal{T})$ crack condition.

When analyzing the evolution of $\mathcal{F}_0$ across the MKO triangle, an approximate single curve $\mathcal{C}$ contains the cases of the OK and MK edges. The conclusion derived from the present work is that, for a large part of the whole MKO triangle (say, $\mathcal{K} \gtrsim 0.3$), $\mathcal{F}_0$ lays on a thin bundle about $\mathcal{C}$.

A method for the graphical representation of these quantities, which could also be applied to other considered physical phenomena, was further provided.

All these conclusions may have practical applications, including readily setting up the initial conditions for more refined calculations of hydraulic fracture propagation, e.g., via finite elements. They can also be useful as a test of the performance of algorithms that neglect the fluid lag, when used in the intermediate regime, thus failing consideration of $\xi_f < 1$. If the computed values for an appropriate range of cases fall within the expected bundle about the universal curve (projected onto the reduced space $\tilde{\mathcal{F}}_0 = \{\Omega_0, \Pi_0, \gamma\}$), then one can regard the method to provide reliable results.

The results presented herein can be taken as guidelines for quick estimations in some field applications, where measurements of crack geometry (width and length) are not readily available, and/or have significant uncertainties, well beyond the $\approx 20\%$ deviation from a strict universal behaviour found here. The particular differences between the 2D and 3D cases indicate a possible extension of the present results to 3D deserves further attention.

Chapter 4

Controlling factors in the interaction between a hydraulic fracture and a natural fracture: strength vs. toughness

4.1 Introduction

As explained in Chapter 1, hydraulic fracturing is especially necessary in low-permeability unconventional source rocks such as shales, where hydrocarbon production is not economical without fracturing (Warpinski et al., 2009). Shale formations often contain natural fractures (NF), and complex hydraulic-fracture networks may form during stimulation. The complex fracture network is strongly influenced by the interaction between the hydraulic fracture (HF) and the pre-existing natural fractures (Gu et al., 2012). This influence was verified by field observations and microseismic measurements (Warpinski et al., 2009; Taleghani and Olson, 2011; Roshankhah et al., 2019).

The nature and degree of this complexity must be understood clearly to optimize stimulation design and completion strategy (Weng et al., 2011). Most fracture propagation models assume an oversimplified single planar geometry of fracture propagation (Valkó and Economides, 1995). However, in highly heterogeneous and naturally fractured formations, this simplified mode doesn't represent the reservoir complexity (Chuprakov et al., 2014) and poses significant challenges for numerical models to simulate (Roshankhah et al., 2018).

Diverse ways of interactions are studied in the literature. As the most basic alternatives, the propagating HF may cross the discontinuity or deflect towards it. In this last case, the hydraulic fracture may propagate along the NF, or alternatively, it may kink out of the interfaces at a distance ℓ_{offset}, whose value plays an important role in the generation of the complex fracture network in the reservoir. Another important parameter that influences the propagation of HF is the presence of a fluid lag, previously analyzed in Chapter 3.

In this Chapter, the mechanical conditions under which the hydraulic fracture deviates, or kink out of the natural fracture, is analyzed through the mechanical factors influencing the size ℓ_{offset}, in both fluid lag and fluid lag-free regimes. We limit the discussion to the fracture energies and interface strengths of the bulk and the natural fracture.

We address this problem using a cohesive zone model methodology as described in section 3.2.2. The CZM departs from usual linear elastic fracture mechanics treatments in a way that naturally allows for the incorporation of both parameters, strength and toughness. The existence of strength and toughness parameters in the mechanical model induces a characteristic length, ℓ_c, in the material which is of a similar magnitude as the fracture process zone size.

The primary focus of this study is to comprehensively analyze the mode of interaction and the offset size ℓ_{offset} in relation to intersection angles ω. Additionally, an evaluation of the impact of confining (compressive) stresses on the subsurface, referred to as crustal stresses, is carried out. It is important to note that our approach adheres to the geomechanical convention, where compressive stresses are regarded as positive.

Within the framework of a 2D model, acting as a representative stand-in for typical fractures propagating along vertical planes, these stresses encompass both the minimum stress (σ_h) perpendicular to the crack, and the maximum stress (σ_H) parallel to the direction of crack propagation within the subsurface crust. This arrangement leads us to define the differential horizontal stress as $\Delta\sigma = \sigma_H - \sigma_h$. This exploration enables a comprehensive understanding of the mechanics at play.

The model and physical parameters utilized in this study are comprehensively defined in Section 4.2. A parametric analysis has been undertaken to establish the range of applicability of the finite element model within both fluid lag and fluid lag-free regimes, as discussed in Sections 4.2.2 and 4.2.3 respectively. In Section 4.3, a systematic study is conducted to ascertain whether the interaction between a hydraulic and a natural fracture is governed by factors such as toughness, critical traction, or a combination of both. Ultimately, our findings are summarized and discussed in Section 4.4

4.2 Model and physical parameters definition

The FEM formulation used on this study is based on the Cohesive Zone Model approach (Dugdale, 1960; Barenblatt, 1962), one of the most commonly used tools to investigate interfacial fracture, which assumes that a cohesive damage zone develops near the crack tip. This approach links the microstructural failure mechanism to the continuum fields governing bulk deformations, thus, is characterized by the properties of the bulk material, the crack initiation condition, and the crack evolution function (Turon et al., 2007).

In a FEM using the CZM approach, the complete material description is separated into fracture properties captured by the constitutive model of the cohesive surface and the properties of the bulk material, captured by the continuum regions. To obtain a successful FEM simulation using CZM (Falk et al., 2001), two conditions must be met: (a) The cohesive contribution to the global compliance before crack propagation should be small enough to avoid the introduction of a fictitious compliance to the model (Rice, 1992; Rice and Beltz, 1994), and (b) the element size must be less than the cohesive zone length (Camacho and Ortiz, 1996; Ruiz et al., 2001).

In this dissertation, a simple cohesive-zone model has been used to describe the bonding across an interface. The model was described in Section 3.2.2 and the geometry and FEM model is described in Section 4.2.1.

4.2.1 Geometry and finite element model

The geometry of the simulation domain is shown in Fig. 4.1. The distance between the injection point and the fracture tip is ℓ, the distance from the tip to the natural fracture (or interface) is ℓ_{HF-IN}. The total length of the natural fracture is $2\ell_{IN}$, with equal lengths spanned to each side of the intersection. The angle between the propagation direction and the natural fracture is ω.

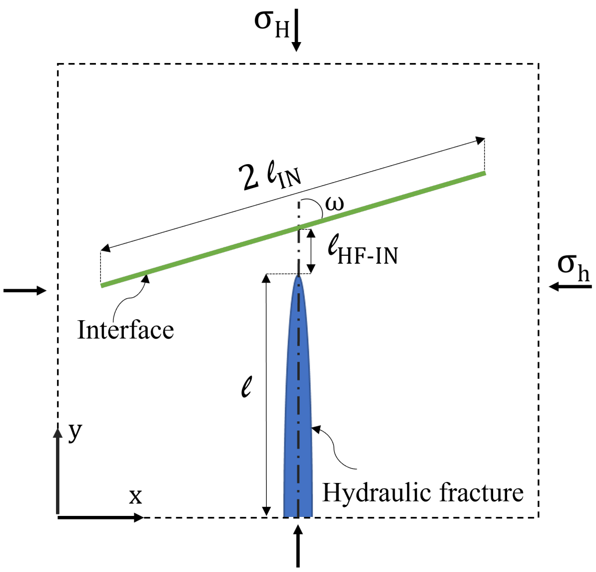

Figure 4.1: Schematics of the simulation domain.

The Young modulus of the volume is E, the Poisson ratio is ν, and the plane strain Young modulus is $E' = E/(1-\nu^2)$.

In the following, a subscript b stands for 'bulk' (i.e., the impinging hydraulic fracture), and subscript i stands for 'interface' (i.e., the natural fracture). The properties of the hydraulic fracture and natural fracture are, respectively, critical traction $\sigma_{c,b}$ and $\sigma_{c,i}$, and fracture energy $G_{c,b}$ and $G_{c,i}$.

The approximate respective cohesive zone sizes are determined by

$$\ell_c = 0.53\frac{E'G_c}{{\sigma_c}^2} \quad , \tag{4.1}$$

(Eq. (3.13), repeated here for convenience). Their ratio is

$$r_c = \frac{\ell_{c,b}}{\ell_{c,i}} = \frac{r_{G_c}}{{r_{\sigma_c}}^2} \ , \tag{4.2}$$

where $r_{G_c} = G_{c,b}/G_{c,i}$ and $r_{\sigma_c} = \sigma_{c,b}/\sigma_{c,i}$.

Similarly as in usual analyses of single fracture propagation, for the present case of an interaction we will work under the prescription that process zone sizes (i.e., cohesive zone sizes) are small compared to structural lengths, i.e.,

$$\ell, \ell_{IN} \gg \ell_{c,b}, \ell_{c,i} \ . \tag{4.3}$$

Given the taxingly large parameter space, in this chapter we consider equal bulk and interface cohesive lengths ($\ell_{c,b} = \ell_{c,i} = \ell_c$). The bulk/interface strength ratio is fixed

($\sigma_{c,b}/\sigma_{c,i} = 10$) so the interface toughness is determined by

$$G_{c,i} = \frac{(\sigma_{c,i})^2 \ell_c}{0.53E'}. \tag{4.4}$$

All other physical and geometrical parameters are held constant, with the following values: $E' = 22\,\mathrm{GPa}$, $\mu' = 0.0156\,\mathrm{Pa\,s}$, $Q = 0.096\,\mathrm{m^3/s}$, $\ell = 2\,\mathrm{m}$, $\ell_e = 7.8\,\mathrm{mm}$. This value of Q is double what is prescribed in our half-plane model.

Considering the fracture length and fluid lag, we can define two propagation regimes:

1) Fluid lag regime: There is a delay in the fluid front with respect to the fracture tip as shown in Fig. 4.2a and 4.2b.

2) Zero fluid lag regime: The fluid front coincides with the fracture tip as shown in Fig. 4.2c.

Including the cohesive length into the analysis, we can subdivide the fluid lag regime into two cases:

1a) $\ell_c < \ell_{lag}$: The cohesive length develops in the dry fracture tip (Fig. 4.2a).

1b) $\ell_c > \ell_{lag}$: The cohesive length comprises both fluid lag and non-fluid lag zones (Fig. 4.2b).

In this particular work we are going to focus on cases *1a* and *2*. The case *1b* is left for future work and from now on, when we talk about the fluid lag regime we will refer to the case *1a*.

Both the cohesive zone and the fluid lag (whenever it is explicitly included) have to be resolved by the finite elements mesh. This requirement induces restrictions on the maximum size of the finite elements, ℓ_e, which must be taken into account when designing the mesh of the numerical model, given the physical parameters, or when determining the suitable range of physical parameters when the mesh is available. These restrictions will be analyzed separately for each of the studied regimes in Sections 4.2.2 and 4.2.3.

4.2.2 Fluid lag regime parameters and admissible zone

In this section we consider a propagation regime in which the fluid lag is not negligible, and it is thus properly resolved. According to the analysis carried out in Chapter 3, in

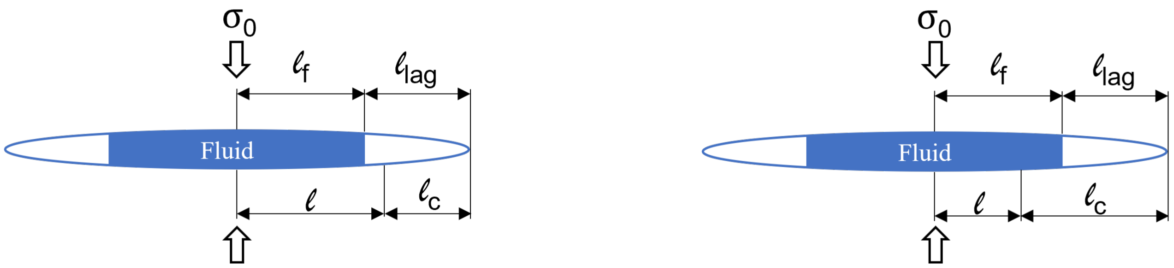

(a) Fluid lag regime and $\ell_c < \ell_{lag}$.

(b) Fluid lag regime and $\ell_c > \ell_{lag}$.

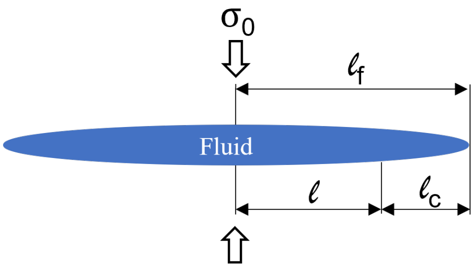

(c) Zero fluid lag regime.

Figure 4.2: Propagation regimes.

order to favor the presence of a sizable fluid lag $\mathcal{T}$ has to be small enough. To ensure this condition is satisfied, the simulations were carried out with no confining stress, $\sigma_0 = 0$, such that $\mathcal{T} = 0$ (see Eq. (3.26)) and thus the simulations are on the OK edge (see Fig. 3.3b). It's worth noting that σ_0, representing the stress perpendicular to the advancing fracture, corresponds to what was earlier identified as the minimum crustal stress, denoted as σ_h.

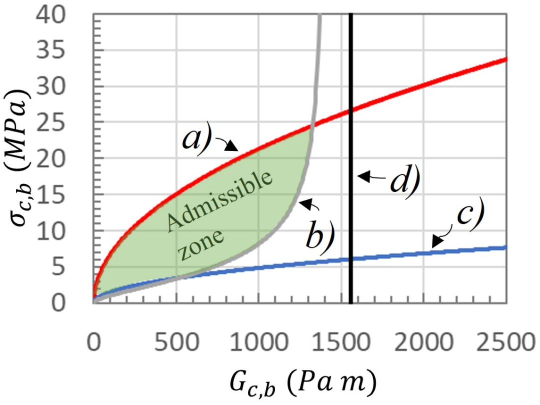

Figure 4.3: Region in the $(\sigma_{c,b}, G_{c,b})$-space where reliable simulations with fluid lag can be performed (highlighted green area), stemming from various requirements on mesh resolution and others. The requirements are: $a)$ $\ell_c \geq 3.3\ell_e$, $b)$ $\ell_{lag} \geq 1.2\ell_c$, $c)$ $\ell \geq 4\ell_c$, $d)$ $\ell_{lag} = (1-\xi_f)\ell \geq 2\ell_e$. Condition $\mathcal{T} = 0$ is not visible in this plot. Values of physical and geometrical parameters are quoted in the text body.

The criteria that impose restrictions on the region in the $(G_{c,b}, \sigma_{c,b})$-space where reliable simulations with fluid lag can be performed are the following:

a) $\ell_c \geq 3.3\ell_e$. This criterion is introduced in order to capture the stress gradient observed in the cohesive zone with sufficient precision. When the cohesive zone is discretized with too few elements, the distribution of stresses ahead of the crack tip is not represented accurately. Therefore, a minimum number of elements, N_e, is needed in the cohesive zone to get reliable results. There is some consensus in the literature about the value of N_e. Falk et al. (2001) used between 2 and 5 elements in their simulations and Turon et al. (2007) used $N_e = 3$. Many other author cite values within this range. There are nevertheless some exceptions, e.g., Moës and Belytschko (2002), based on the work of Carpinteri et al. (2003), suggested using more than 10 elements. At an extreme, Pro et al. (2018) conclude that N_e above 100 is needed. In this work we use $N_e = 3.3$, which is within the range of most bibliography. This restriction leads, via Eq. (4.1), to the upper bound for $\sigma_{c,b}$

$$\sigma_{c,b} \leq 0.401\sqrt{\frac{E'G_{c,b}}{\ell_e}} \quad . \tag{4.5}$$

Fig. 4.3 illustrates with a red curve the present case. The smaller the element size, the larger the upper bound and thus the admissible region.

b) $\ell_{lag} \geq 1.2\ell_c$. This restriction imposes the non-penetration of the fluid in the cohesive length. As described on the previous section, in this work we are considering the fluid lag regime as illustrated in Fig. 4.2. The length ℓ_{lag} can be computed as (Garagash, 2006a)

$$\ell_{lag} = (1 - \xi_{f,OK}(\mathcal{K}))\ell \quad , \tag{4.6}$$

where ℓ is the total hydraulic fracture length at the moment of the interaction and $\xi_{f,OK}$ is the fluid fraction on the OK edge, see Figs. 3.3 and 3.4. For estimating $\xi_{f,OK}$, we use the implicit Eq. (3.29) (Section 3.4.2).

By combining Eq. (4.6) with the cohesive length definition in Eq. (4.1) we get the lower bound

$$\sigma_{c,b} \geq 0.797\sqrt{\frac{E'G_{c,b}}{(1 - \xi_{f,OK}(\mathcal{K}))\ell}} \quad . \tag{4.7}$$

In order to consider explicitly $\xi_{f,OK}(\mathcal{K})$, we obtain from Eqs. (3.25), (3.1) and (3.14)

$$\mathcal{K} = \left(\frac{32}{\pi}\right)^{1/2} \frac{{G_{c,b}}^{1/2}}{(E'Q\mu')^{1/4}} \quad . \tag{4.8}$$

Then we can use Eq. (3.29) to derive the dependence of $\sigma_{c,b}$ on $G_{c,b}$. Given that asymptotically as $G_{c,b} \to \infty$, $\mathcal{K} \to \infty$ and (Garagash, 2006a)

$$1 - \xi_{f,OK} \sim 0.129 \exp\left(-\frac{3\pi}{32}\mathcal{K}^4\right) \quad , \tag{4.9}$$

this lower bound has a steep increase for large $G_{c,b}$, instead of the parabolic shape as curve (a). This requirement ensures that, in addition to being on the OK edge, the configuration is far enough from the K-vertex.

Fig. 4.3 illustrates with a grey curve the present case. This criterion is independent of the element size. The admissible region can be expanded downwards by increasing the fracture length.

c) $\ell \geq 4\ell_c$. This criterion imposes that the cohesive length is fully developed before the FH-IN interaction occurs, and it is an embodiment of Eq. (4.3). Using Eq. (4.1) we get the lower bound

$$\sigma_{c,b} \geq 1.456\sqrt{\frac{E'G_{c,b}}{\ell}} \quad . \tag{4.10}$$

Fig. 4.3 illustrates with a blue curve the present case. This criterion is independent of the element size. The admissible region can be expanded downwards by increasing the fracture length.

d) $\ell_{lag} \geq 2\ell_e$. This criterion is introduced to ensure the fluid lag is properly resolved. Similarly as in item (b) above, Eqs. (4.6) and (4.9) imply

$$\mathcal{K} \leq \left(\frac{32}{3\pi}\right)^{1/4}\left(\ln\frac{0.129}{2}\frac{\ell}{\ell_e}\right)^{1/4} \quad . \tag{4.11}$$

The more accurate and implicit Eq. (3.29) could be used instead of Eq. (4.9). With the current values we have $\mathcal{K} \leq 1.65$, which along Eq. (4.8) gives an upper bound, the vertical black line in Fig. 4.3.

This criterion is automatically satisfied given (a) and (b) above. This is evident in Fig. 4.3 as well for the present case. It is nevertheless instructive to make it explicit, and it is also useful for the case *1b* above (Fig. 4.2b, not advanced further in this work), where it has to be explicitly taken into account.

For each angle of approach, $\Delta\sigma$ was chosen in order to have a transition in the interaction mode inside the admissible zone. The systematic experiments carried out by

Blanton (1982), whose results are shown in Fig. 4.4, indicated that hydraulic fractures tend to cross preexisting fractures only under high differential crustal stresses ($\Delta\sigma$) and high angles of approach. At intermediate and low-differential stresses and angles of approach preexisting fractures tend either to open or arrest. Therefore, for smaller ω, higher $\Delta\sigma$ values were needed to observe the transition.

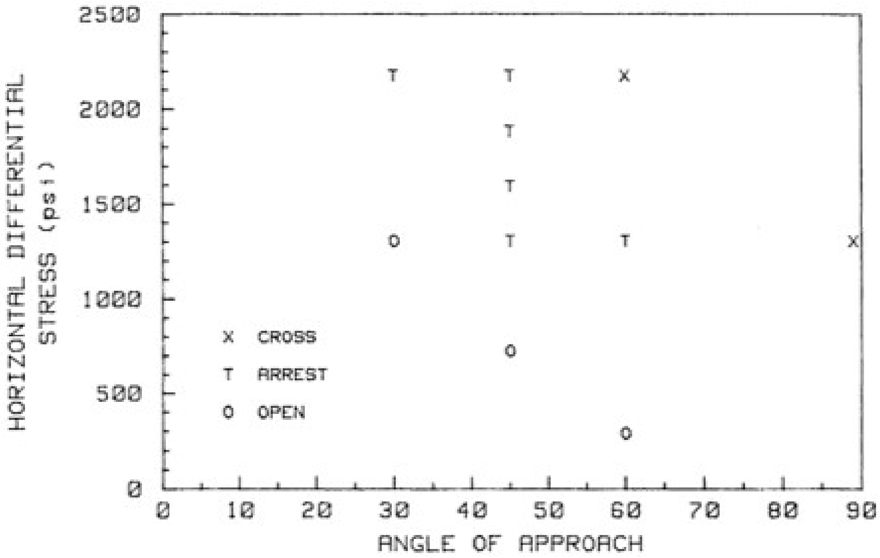

Figure 4.4: Type of interaction (Cross, Arrest or Open) observed at different combinations of differential stress $\Delta\sigma$ and angle of approach ω. Extracted from Blanton (1982).

4.2.3 Fluid lag-free regime parameters and admissible zone

Similarly as in previous section, we determine here the requirements to carry out reliable simulations under conditions of negligible fluid lag.

For the cohesive length to be fully developed and resolved with at least $3.3\ell_e$, criteria (a) and (c) in Sec. 4.2.2 above must also be met. Both criteria are shown again in Fig. 4.5.

The size of the fluid lag is dealt with above by criteria (b) and (d). They ensure that the system configuration meets two requirements, namely, being on the OK edge, and far enough from the K-vertex, see Fig. 3.3b for the MKO parameter space. Here, we will provide two alternative conditions that break one or the other requirement, so ξ_f is close enough to 1. According to the analysis performed in Chapter 3 these are:

e) $\mathcal{K} \geq 2$ (close to the K-vertex): According to Lecampion and Detournay (2007), $\mathcal{K} \gtrsim\approx 2$ ensures the lag is negligible. This threshold is similar to what is obtained with the analysis of item (d) above and gives a lower bound, the vertical black line in Fig. 4.5

f) $\mathcal{K} < 2$ and $t_{ini} > t_{il}$ (close to the MK line; t_{ini} is the initial simulation time): If $t > t_{il}$ the system is in the late time regime (see Eq. (3.45)), and $\xi_f \approx 1$ (see Eq. (3.43)), regardless of the $\mathcal{K}$ value. Therefore, for $\mathcal{K} < 2$, $t_{ini} > t_{il}$ ensures that $\xi_f \approx 1$ across the simulation. This imposes a condition on the initial simulation time as

$$t_{ini} > \frac{E' {\mu'}^3}{\sigma_0} \quad . \tag{4.12}$$

Simulations in the fluid lag-free regime were designed to fulfill one of the two conditions mentioned above. Simulations with $\mathcal{K} \geq 2$ do not have any restrictions on the initial time, and simulations with $\mathcal{K} < 2$ have an initial time estimated with Eq. (4.12).

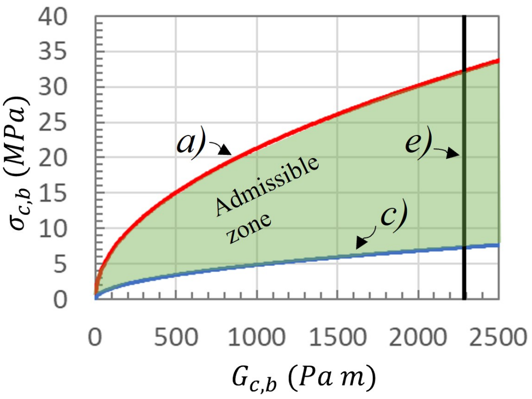

Figure 4.5: Region in the $(\sigma_{c,b}, G_{c,b})$-space where reliable simulations in fluid lag-free regime can be performed (highlighted green area), stemming from various requirements on mesh resolution and others. The requirements are: *a)* $\ell_c \geq 3.3\ell_e$, *c)* $\ell \geq 4\ell_c$, *e)* $\mathcal{K} \geq 2$ or *f)* $\mathcal{K} < 2$ and $t_{ini} > t_{il}$ (not visible in this plot). Values of physical and geometrical parameters are quoted in the text body.

4.3 Systematic study: strength vs. toughness

After having described the model and allowed zones in the $(G_{c,b}, \sigma_{c,b})$ space for both fluid lag and fluid lag-free regimes we performed a systematic study by modifying $G_{c,b}$ and $\sigma_{c,b}$ independently. The complete set of physical parameters of the system is E, ν, $G_{c,b}$, $\sigma_{c,b}$, β_b, $G_{c,i}$, $\sigma_{c,i}$, β_i, ω, ℓ, ℓ_{HF-IN}, D, Q, μ, σ_h, σ_H.

In our simulations, we have observed that the hydraulic fracture often diverts into the natural fracture, and after propagating across some length ℓ_{offset} along the natural fracture, it kinks out again into the bulk material, continuing its propagation essentially perpendicular to σ_h, as expected. An offset in the hydraulic fracture is thus formed. This type of interactions was also observed in experimental hydraulic fracture test with discontinuities performed by Warpinski (2011). One photograph showing an experimental offset is shown in Fig. 4.6.

Figure 4.6: Fracture growth across discontinuities forming an offset, obtained during hydraulic fracture experimental tests, performed by Warpinski (2011).

Sometimes, the fracture runs across the whole length of the natural fracture, and only then it kinks out in its original direction, so $\ell_{offset} = \ell_{IN}$. In these cases, it is not clear what would the actual value of ℓ_{offset} be for a long enough interface. There might even be conditions under which $\ell_{offset} \to \infty$. We generally consider these cases as (full) opening.

In the following, we analyze quantitatively several aspects of the offset formation and length, and we develop the corresponding 'interaction offset maps'. Then we proceed with a qualitative consideration of features of these maps.

Fig. 4.7 shows two example offsets formed in an interaction of a HF with an interface with incident angle $\omega = 75°$.

In our simulations four interaction regimes were identified:

- Crossing: $\ell_{offset} = 0\,\mathrm{m}$
- Crossing with an offset: $0 < \ell_{offset} < \ell_{IN}$
- Opening (i.e., crossing with maximum offset): $\ell_{offset} = \ell_{IN}$

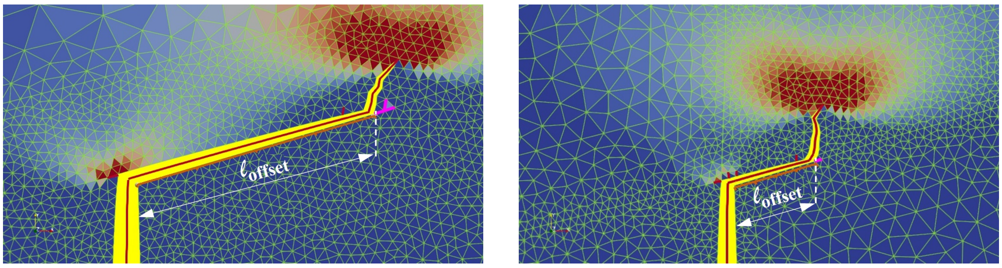

(a) $\ell_{offset} = 0.356\,\text{m}$. (b) $\ell_{offset} = 0.173\,\text{m}$.

Figure 4.7: Typical offsets formed with an incident angle $\omega = 75°$ and $\ell_{IN} = 1\,\text{m}$.

The selected non-dimensional parameters for our study are:

- $r_{G_c} = 100$
- $r_{\sigma_c} = \sqrt{r_{G_c}} = 10$.

According to Eq. (4.2), this leads to a ratio of $r_c = 1$ between the cohesive zone lengths within the bulk and along the interface, throughout our simulations.

The dimensional system parameters employed in the simulations are as follows:

- Elastic properties: $E = 21\,\text{GPa}$, $\nu = 0.2$.
- Injection / fluid parameters: Injection flow rate $Q = 0.096\,\text{m}^3/\text{s}$, viscosity $\mu = 0.0013\,\text{Pa s}$.
- Cohesive law mode weighting factor (see Eq. (3.9)): $\beta_b = \beta_i = \beta = 10$.

4.3.1 Fluid lag regime results

In this section, we undertake an analysis of the outcomes derived from simulations conducted in the fluid lag regime, as described in Sec. 4.2.2. These simulations were executed employing the algorithm detailed by Smilovich et al. (2021).

Fig. 4.8 illustrates the combined influence of $G_{c,b}$ and $\sigma_{c,b}$ on the nature of interaction for varying angles of approach $\omega = 45°, 60°, 75°, 90°$. An overall pattern is apparent from the figure: when $\sigma_{c,b}$ is held constant (variations on a horizontal line) the nature of the interaction varies little. In contrast, with $G_{c,b}$ maintained at a constant value (variations on a vertical line), the interaction type shifts from a crossing pattern observed at lower $\sigma_{c,b}$ values to an offset configuration as $\sigma_{c,b}$ increases, reaching the limiting condition of a

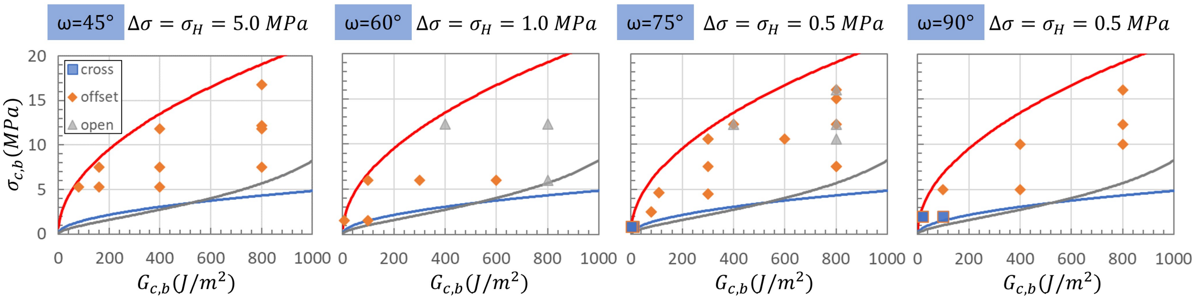

Figure 4.8: Maps of interaction type in the $(G_{c,b}, \sigma_{c,b})$-space: cross ($\ell_{offset} = 0$), offset ($0 < \ell_{offset} < \ell_{IN}$) or open ($\ell_{offset} = \ell_{IN}$) for simulations in the fluid lag regime, cf. Fig. 4.11.

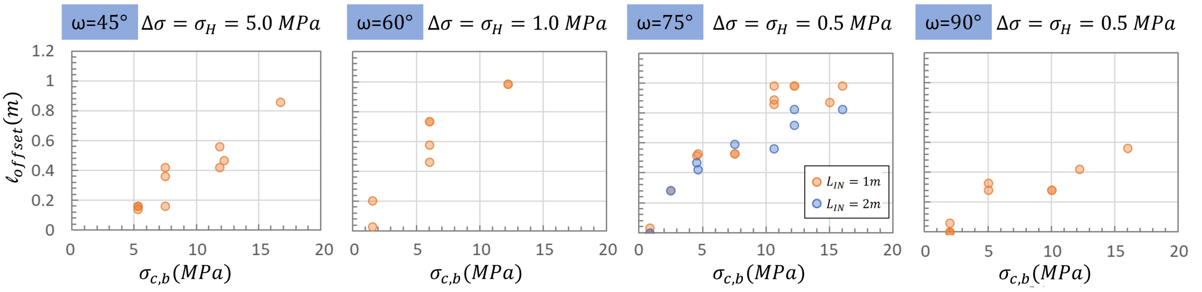

Figure 4.9: ℓ_{offset} vs $\sigma_{c,b}$ for the simulations in the fluid lag regime with different interaction angles and corresponding σ_H.

full open interaction. This trend becomes more evident when examining interfaces with increasing ω.

For a more quantitative analysis, we turn our attention to inspecting the results for the offset length, as shown in Fig. 4.9. This figure includes data from all the simulations in Fig. 4.8, irrespective of the value of $G_{c,b}$. With some slight scatter in data, ℓ_{offset} shows an increasing trend with $\sigma_{c,b}$ across all studied ω values. For $\omega = 75°$, two different values of ℓ_{IN} were used to test for a potential impact of that geometrical parameter. No discernible effect was observed. This robust dependency is an empirical finding, for the range of properties under consideration.

A further analysis is provided by plotting the same ℓ_{offset} data as a function of $G_{c,b}$. As Fig. 4.9 suggests, data would not collapse onto a single approximate curve for each ω, so we plot data for each $\sigma_{c,b}$ separately, in Fig. 4.10. We only plot data for $\omega = 45°, 75°$, given that for $\omega = 60°, 90°$ data is scarcer. Here it is more clearly apparent that, within some scatter, ℓ_{offset} is essentially independent of $G_{c,b}$, and it is fully controlled by $\sigma_{c,b}$.

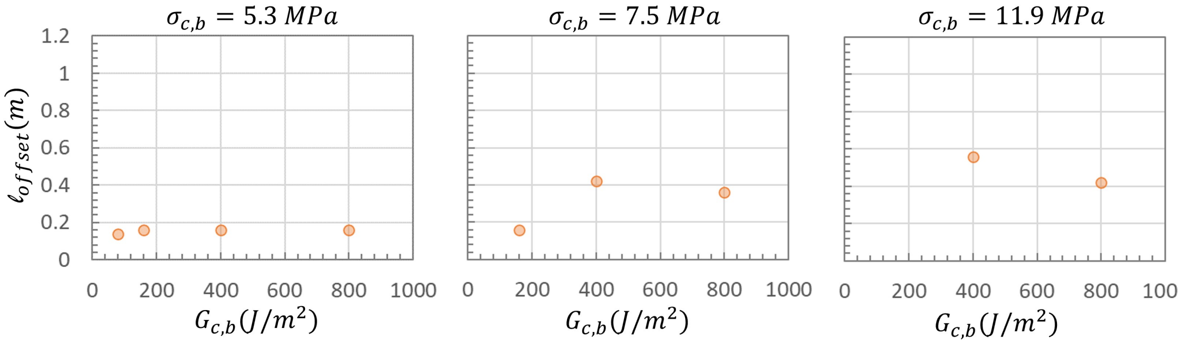

(a) $\omega = 45°$, $\Delta\sigma = \sigma_h = 1.0\,\mathrm{MPa}$.

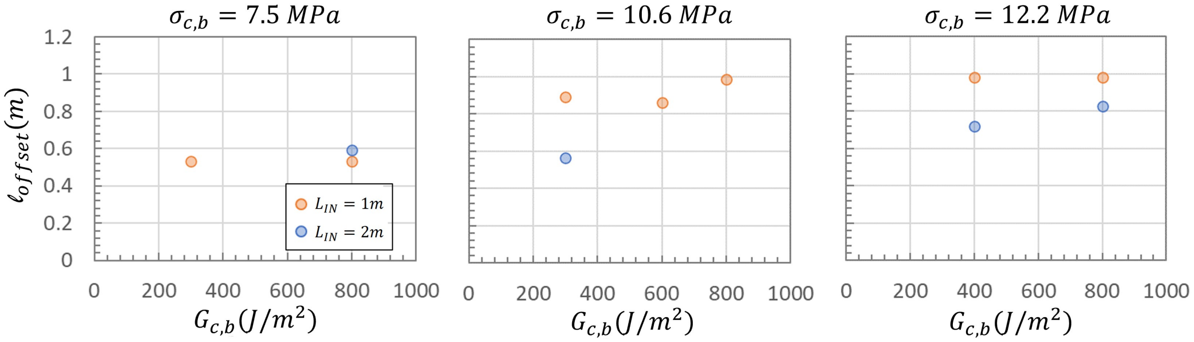

(b) $\omega = 75°$, $\Delta\sigma = \sigma_h = 0.5\,\mathrm{MPa}$.

Figure 4.10: ℓ_{offset} vs $G_{c,b}$ for the simulations in the fluid lag regime with different interaction angles, at constant $\sigma_{c,b}$.

4.3.2 Fluid lag-free regime results

In this section we analyze the results from the simulations in the fluid lag-free regime, as described in Sec. 4.2.3. These simulations were performed with the algorithm described by Smilovich et al. (2023). Among other distinctive features as compared to the fluid lag algorithm, the present one allows for a prescribed time step, which is fixed in this section at $\Delta t = 2.0 \times 10^{-3}$ s.

Fig. 4.11 shows the combined effect of G_c and σ_c on the type of interaction (crossing, offset or opening) for angles of incidence $\omega = 45°, 60°, 75°, 90°$. The results are qualitatively the same as shown in Fig. 4.8 for the case of an existing fluid lag, namely, a strongly G_c-controlled interaction.

A similar analysis as provided in Figs. 4.9 and 4.10, for the present case, is shown in Figs. 4.12 and 4.13, respectively. Fig. 4.12 shows a very steep dependence of ℓ_{offset} on $G_{c,b}$, with a slope apparently increasing with increasing ω. For $\omega = 90°$ we see an extreme case, with no offset-type interactions, but either cross or open. It is not clear at this point whether using a longer natural fracture would lead to a sizable $\ell_{offset} < \ell_{IN}$. Fig. 4.13 confirms the values of ℓ_{offset} are nearly independent of $G_{c,b}$, for $\omega = 60°, 75°$.

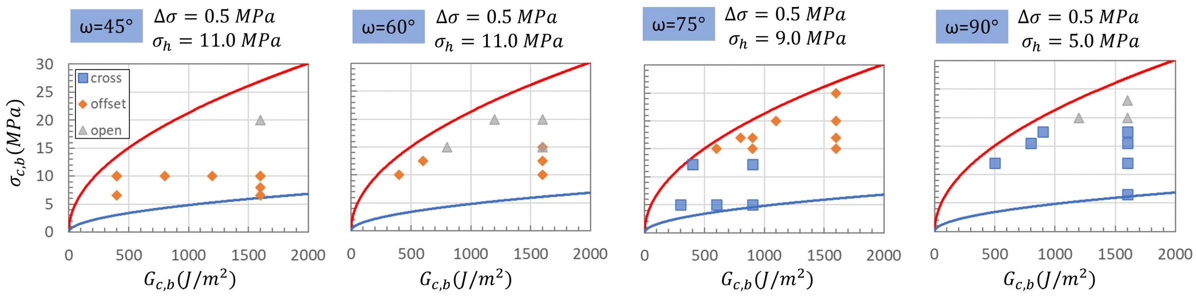

Figure 4.11: Maps of interaction type in the $(G_{c,b}, \sigma_{c,b})$-space: cross ($\ell_{offset} = 0$), offset ($0 < \ell_{offset} < \ell_{IN}$) or open ($\ell_{offset} = \ell_{IN}$) for simulations in the fluid lag-free regime, cf. Fig. 4.8.

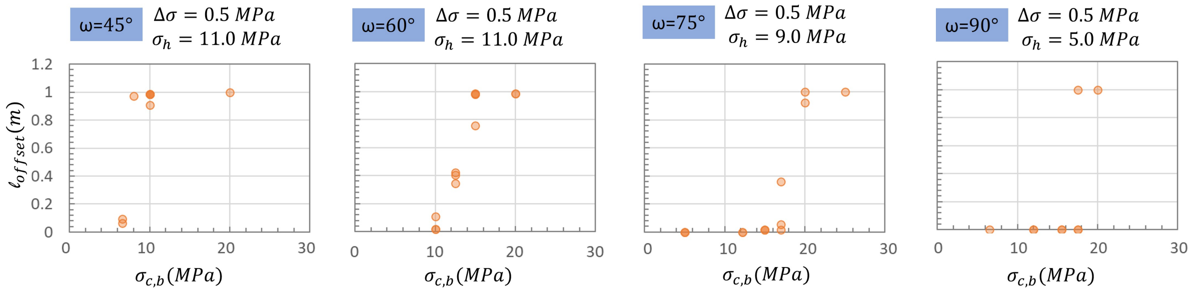

Figure 4.12: ℓ_{offset} vs $\sigma_{c,b}$ for simulations in the fluid lag-free regime with different interaction angles and corresponding σ_h, σ_H.

4.3.2.1 Time increment and mesh variation analysis

Given some incidental observations during our testing program, we endeavored the analysis of the effect of some numerical variables on the resulting interaction. As a starting point, we focused on the fluid lag-free algorithm, dealing with the impact of the time increment and mesh type on ℓ_{offset}. To examine the temporal convergence of the algorithm, we reduced Δt across a range from 2.0×10^{-3} s (as employed in previous section simulations) to 1.0×10^{-4} s. Additionally, adjustments were made to the mesh configuration by altering two parameters: the geometric propagation path aligned with the hydraulic fracture direction, and a bounding box enveloping the natural fracture area with uniform mesh sizing.

- Mesh configuration 1: Incorporates a geometric propagation line and excludes a bounding box around the natural fracture, shown in Fig. 4.14a.

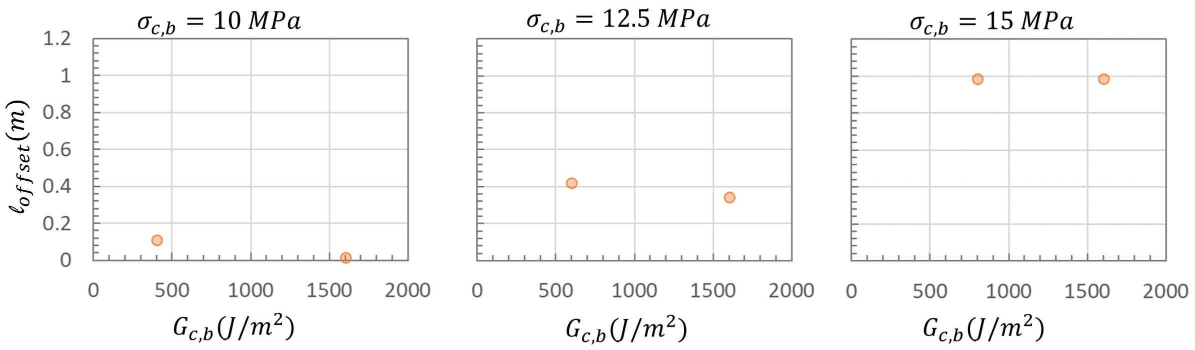

(a) $\omega = 60°$, $\Delta t = 1.0 \times 10^{-3}$ s, $\sigma_h = 11.0$ MPa.

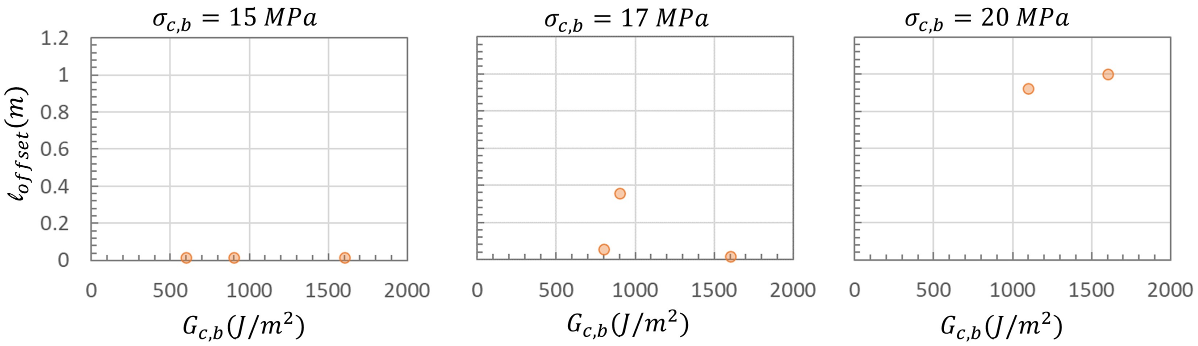

(b) $\omega = 75°$, $\Delta t = 2.0 \times 10^{-3}$ s, $\sigma_h = 9.0$ MPa.

Figure 4.13: ℓ_{offset} vs $G_{c,b}$ for the simulations in the fluid lag regime with different interaction angles, at constant $\sigma_{c,b}$.

- Mesh configuration 2: Omits a geometric propagation line while employing a uniform-sized bounding box around the natural fracture area, shown in Fig. 4.14b.

- Mesh configuration 3: Encompasses both a geometric propagation line and a uniform-sized bounding box around the natural fracture, shown in Fig. 4.14c.

Fig. 4.15a shows the combined effect of the mesh type and Δt on ℓ_{offset}. In the case of Mesh 1, reducing Δt led to a nearly 100% increase in ℓ_{offset}, as illustrated in Fig. 4.14a. However, the values calculated did not attain convergence in terms of Δt within the examined parameter range. At any rate, the qualitative behaviour did not change with Δt. In contrast, for Mesh 2, a decrease in Δt resulted in a change of interaction type, from crossing to offset, which implies an increase in ℓ_{offset}. Mesh 3, the opposite trend was observed. Reducing Δt led to a shift in the interaction type from offset (with a small ℓ_{offset}) to crossing.

For illustrative purposes, Figs. 4.15b through 4.15d present snapshots captured from simulations conducted at $\Delta t = 1.0 \times 10^{-3}$ s, showcasing the interaction outcomes. These

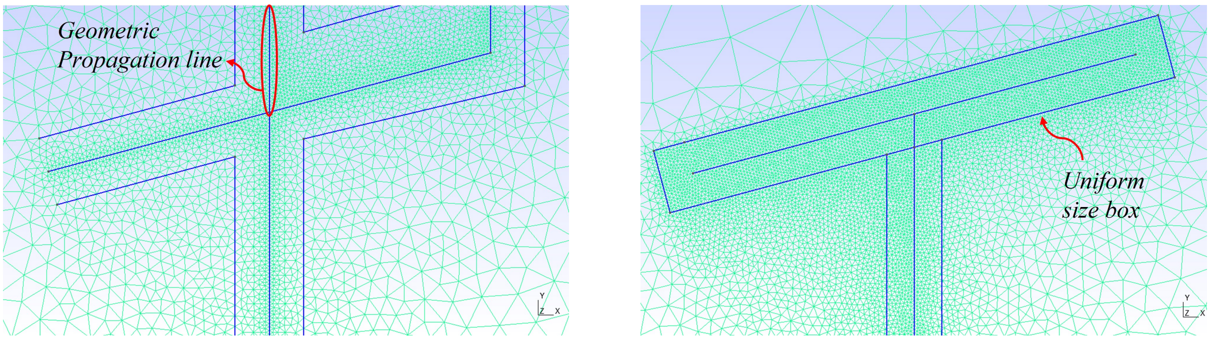

(a) Mesh configuration 1: With geometric propagation line and no bounding box around the natural fracture.

(b) Mesh configuration 2: No geometric propagation line and uniform size bounding box around the natural fracture.

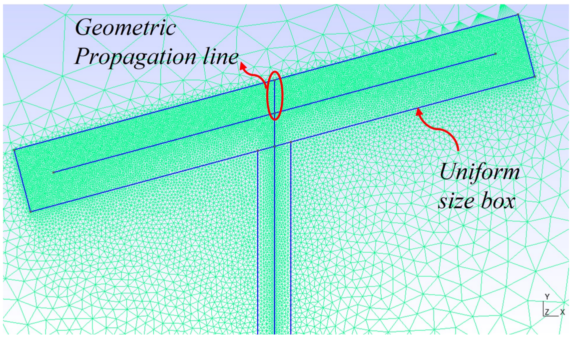

(c) Mesh configuration 3: With geometric propagation line and a uniform size bounding box around the natural fracture.

Figure 4.14: Different mesh configurations analyzed.

images highlight that some scatter in the results can be obtained with some variations in non-physical parameters.

4.4 Discussion and Conclusions

We conducted a comprehensive examination of key factors governing the interaction between a hydraulic fracture and a natural fracture, covering a large part of the MKO diagram for the impinging hydraulic fracture. The investigation delved into the mechanical circumstances that lead to the deflection or kinking out of the hydraulic fracture from the natural fracture. This analysis focused on understanding the mechanical variables that influence the resulting offset length ℓ_{offset}. To our knowledge, this is the first time such an analysis was performed for hydraulic fractures.

The parameter space for the present problem is extremely large. Within the section of

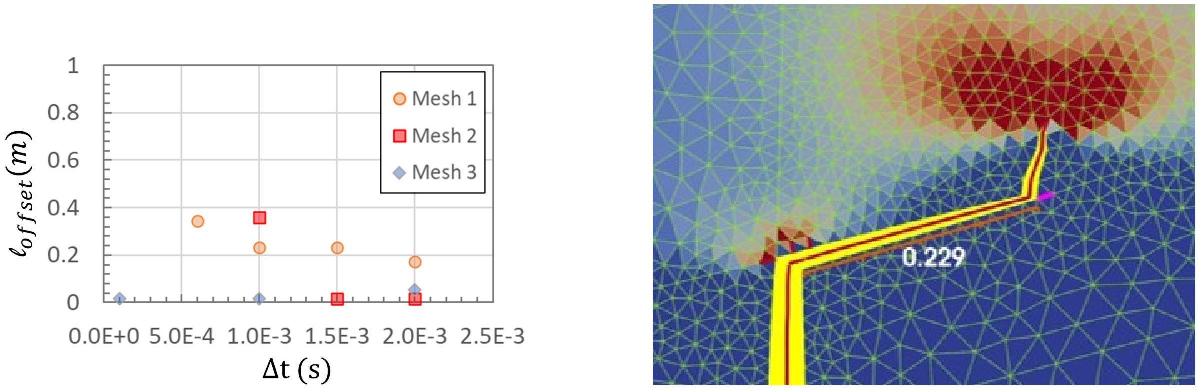

(a) ℓ_{offset} variation with Δt for simulations with three different meshes and $\omega = 75°$, $\sigma_h = 9\,\text{MPa}$, $\sigma_{c,b} = 17\,\text{MPa}$.

(b) Simulation with mesh configuration 1, $\ell_{offset} = 0.229\,\text{m}$.

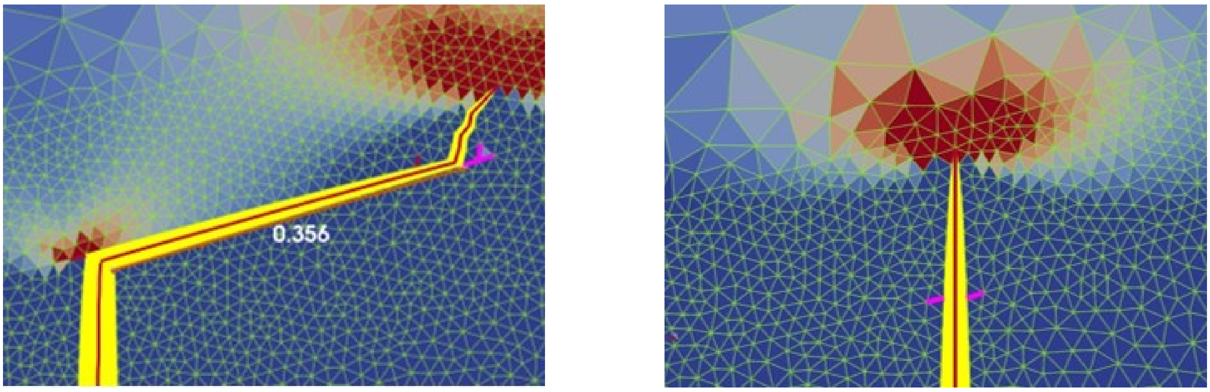

(c) Simulation with mesh configuration 2, $\ell_{offset} = 0.356\,\text{m}$.

(d) Simulation with mesh configuration 3, $\ell_{offset} = 0\,\text{m}$.

Figure 4.15: Mesh and time increment analysis in fluid-lag-free regime.

that parameter space currently covered, the present results support an interaction mode essentially controlled by the critical traction $\sigma_{c,b}$, and insensitive to $G_{c,b}$. These results are counter to what is known from LEFM for the dry propagation of a single fracture, where there does not exist a critical traction. They also diverge from results from cohesive zone modeling of a dry propagating fracture, whenever the size of the cohesive zone is small compared to structural length scales. In these cases, again given the cohesive zone is properly resolved by the finite elements mesh (condition (a) of Sec. 4.2.2), the critical traction $\sigma_{c,b}$ does not have any effect on the results, other than modifying the stress environment about the crack tip as the fundamental theory prescribes. Moreover, as we will see in Chapter 6, this lack of dependence of results on $\sigma_{c,b}$ has been taken advantage of to accelerate cohesive zone model simulations of crack propagation (Turon et al., 2007; Smilovich et al., 2018).

When contrasting our results with possible effects of the cohesive law (i.e., essentially of the critical traction) on propagation of single hydraulic fractures, there is only one reference available. Garagash (2019) analyzed this effect on propagation regimes for a 3D penny shaped fracture. He concluded that, in addition to the two non-dimensional parameters $(\mathcal{K}, \mathcal{T})$ that characterize the state of the system, a new non-dimensional parameter $\Sigma_c = \sigma_{c,b}/\sigma_0$ is relevant. The case $\Sigma_c \gg 1$, which again implies that the size of the cohesive zone is negligible, this time in comparison with the fluid lag, also has vanishing cohesive effects. Even if Garagash (2019) found conditions for which $\sigma_{c,b}$ has an effect on crack propagation, the inherent differences between the 3D fracture (Detournay, 2016) and the present 2D KGD fracture (Garagash, 2006a) preclude further comparisons at this point.

In addition to the conclusion above, an additional analysis showed that there is some effect of numerical factors as the time step and mesh structure. Even if the qualitative conclusion about the dominant role of $\sigma_{c,b}$ appears robust, this finding prompts for the need of having reliable benchmarks that can be used for quantitative comparisons.

Following the completion of this study, several crucial conclusions can be drawn:

1) Our findings demonstrate that the offset length is primarily governed by the critical traction, exhibiting a notable degree of independence from fracture energy within the investigated range of parameters in hydraulic fracture simulations.

2) The interaction mode and offset length exhibit some variability when influenced by the mesh type and the time increment employed in fluid lag-free regime simulations.

3) A more comprehensive study is required to validate the accurate resolution of kink-in and kink-out phenomena, which are pivotal determinants of the offset length. This forms the central objective of Chapter 5.

In closing, we give some possible venues for additional work: 1) Expanding the region in the parameter space analyzed, including a dimensional analysis, 2) Extending the analysis of Garagash (2019) to cohesive effects in 2D hydraulic fractures.

Chapter 5

Controlling factors in the interaction between a propagating dry fracture and an interface: strength vs. toughness

This chapter, with minimal modifications, is under preparation for submission of two papers.

5.1 Introduction

In Chapter 4 we analyzed the effect of strength and toughness on hydraulic fracture interaction with discontinuities. We found that, in the analyzed properties range, strength controls the interaction. Further analysis prompted the need for reliable benchmarks that can be used for quantitative comparisons. Given that hydraulic fracturing under those conditions involved an extremely rich problem and parameter space, we decided to tackle the simpler problem of a dry cohesive fracture. To develop benchmarks for the offset length ℓ_{offset}, this problem is in turn composed of the following problems, with increasing complexity:

1) Dry fracture propagation and deflection or kinking into an interface.

2) Dry fracture propagation on an interface and kinking out of it.

3) Incorporation of a constant internal pressure into problems (1) and (2) above.

There are currently no analytical or semi-analytical research on kink-in or kink-out in hydraulic fracturing, but there are some studies for dry fracturing, items (*1*) and (*2*), that can be taken as a reference for the analysis. These analyze two fundamentally different cracking scenarios. In the first, the possible crack paths are determined a priori: the crack can only penetrate into the substrate or deflect at a pre-defined angle into the interface (Hutchinson et al., 1987; Hutchinson and Suo, 1991; Parmigiani and Thouless, 2006; Parmigiani, 2007; Foulk III et al., 2008; Strom and Parmigiani, 2014; Alam et al., 2016). In the second, the crack path selection is part of the problem: the crack can kink out of the interface and therefore the kink angle is part of the solution (He and Hutchinson, 1989b; He et al., 1991; Pro et al., 2018). The latter problem is not analyzed here, but has been analyzed with a cohesive zone approach by Pro et al. (2018).

In this Chapter we will focus on obtaining a fracture penetration versus deflection benchmark for kink-in in dry fracture. We leave the other two problems for future studies. We will first begin with a brief literature review of the problem of penetration (P) of versus deflection (D) into an interface (PD problem), and in particular of the consideration of strength and toughness.

The interaction between the mechanical properties of materials, strength and toughness, which determines the conditions under which a fracture will nucleate, propagate and interact with discontinuities, has been discussed in the literature (Leguillon, 2002; Parmigiani and Thouless, 2006, 2007; Pro et al., 2018). One field of study where such interactions play a prominent role is in hydraulic fracturing problems with application to unconventional oil reservoirs. Whether hydraulic fractures impinging on natural interfaces activate them (deflection) or cross them (penetration) is a relevant effect on the effective permeability and productivity of the reservoir (Chuprakov et al., 2014; Garagash, 2019). But, for example, both properties play an important role in determining the interaction mechanism that arises between propagating (dry) fractures in a solid medium impinging on adhesive interfaces (Parmigiani and Thouless, 2006).

Methods for predicting fracture penetration versus deflection can be classified into three categories according to the material properties used in the criteria: traction-based methods, energy-based methods and combined (traction and energy) methods. Historically, methods based on traction were the first to be developed and methods combining traction and energy are the most recent.

Traction-based methods are predicated on comparing the traction field at the tip of the incident fracture with the resistances of the interface and the substrate on the other side of the interface. The most sophisticated of these is the work of Gupta et al. (1992) in which the mode of propagation is determined by the ratio of the maximum opening normal traction on the other side of the interface to the maximum opening normal traction along the interface. For a system with materials having identical elastic properties on either side of the interface, the transition is predicted at a strength ratio of substrate to the interface $r_\sigma = \sigma_{c,s}/\sigma_{c,i}$ of approximately 3.5.

Energy-based methods apply linear elastic fracture mechanics to fractures with short kinks extending from the fracture tip (e.g., Hutchinson et al., 1987; Thouless et al., 1989; Martinez and Gupta, 1994; He and Hutchinson, 1989a; Lu and Erdogan, 1983; Tullock et al., 1994). Penetration is usually modeled by a kink that extends directly ahead of the initial fracture tip and crosses the interface. Deflection can be modeled as a separate case in a second geometry by kinks extending laterally from the initial fracture tip along the interface. In these methods, the penetration behavior versus deflection is determined from a comparison of the energy release rates G in the various configurations with the corresponding critical values $G_{c,s}$ of the matrix or substrate (s) and $G_{c,i}$ of the interface (i), respectively. Similarly, the stress intensity K_I and the toughness K_{Ics} and K_{Ici} can be considered. The best known of the energy approaches is that of He and Hutchinson (1989a), with corrections (Martinez and Gupta, 1994; He et al., 1994). One result of that work is that the transition will occur when the ratio between the critical fracture energies of the substrate and the interface, $r_G = G_{c,s}/G_{c,i}$, is about 4.0 given a system with substrates having identical elastic properties on both sides of the interface, and normal incidence on the interface.

Mixed methods, which consider the strength and toughness of the substrate and interface, typically use a cohesive zone model. Parmigiani and Thouless (2006) showed that the penetration versus deflection criterion is, in general, a function of both critical values. They also showed by way of verification that, in appropriate limits, the cohesive zone model reproduces the above result in that the transition ratio between modes is $G_{c,s}/G_{c,i} \approx 4.0$. Subsequently, Foulk III et al. (2008) applied the cohesive zone approach to the transgranular/intergranular fracture mode transition (i.e., grain penetration versus grain boundary deflection) of a high-strength, low-toughness material system. Moreover, Strom and Parmigiani (2014) complemented the work of Parmigiani and Thouless (2006) by quantifying the results in terms of the applied load, and Alam et al. (2016) extended the analysis of Parmigiani and Thouless (2006) to fracture incidence angles on the interface less than 90°.

Among the aforementioned works, probably Foulk III et al. (2008) analyze the mechanics of the transition in most detail. The transition is described as occurring by competing process zones; one along the interface in the deflection direction with length $\ell_{c,i}$, and one across the interface in the penetration direction with length $\ell_{c,s}$. The importance of both process zones in the interaction mechanism precludes the use of solely energy-based or solely strength-based criteria to describe the transition event. This is characterized as unstable in the sense that the driving force rises as both process zones are created. Once a propagation mode emerges, the other tends to reduce its driving force, with a collapsing process zone. It is explained that a mixed criterion is needed to determine the mode of interaction (penetration or deflection). However, propagation proceeds by the usual LEFM criteria once the interaction is well defined.

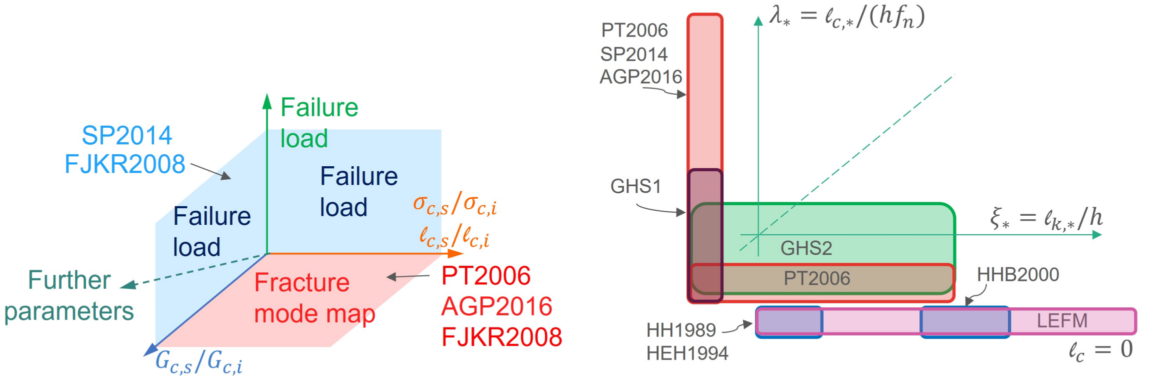

(a) (b)

Figure 5.1: Illustration of the main parameters involved in the problem, and regions in the parameter space that were considered by several authors: He and Hutchinson (1989a) (HH1989), He et al. (1994) (HEH1994), He et al. (2000) (HHB2000), Parmigiani and Thouless (2006) (PT2006), Foulk III et al. (2008) (FJKR2008), Strom and Parmigiani (2014) (SP2014), Alam et al. (2016) (AGP2016) and our work, Sec. 5.4 (GHS1) and 5.5 (GHS2).

Fig. 5.1a shows a schematics of the parameter space for the present problem, see next section for more details. Following other's analyses (see figure caption), the ratios r_G and r_σ stand out as main parameters, and they are thus represented explicitly. The cohesive length ratio $r_\lambda = \ell_{c,s}/\ell_{c,i} = r_G/{r_\sigma}^2 = \lambda_s/\lambda_i$ (see also Eq. (4.2) and definitions of λ_s, λ_i below) is an alternative parameter, and any pair among the three provides an equivalent description. The output of the analysis and simulations can be represented in alternative forms. When considering sections of the parameter space (e.g., the $r_G - r_\sigma$ plane), interaction mode maps are obtained, where the regions of mode dominance and the lines dividing those regions are represented. Calculations are aimed at establishing those lines. When considering output variables (e.g., the critical load, measured cohesive zone lengths, etc.), some additional insight can be provided into the mechanics of the fracture and competition process.

Several authors considered one or the other aspect of the problem, and/or limited sections of the parameter space, as indicated in the figure using colors for enhanced clarity. To consider in more detail what regions of the parameter space were covered, we define two pairs of additional non-dimensional parameters. First we have the non-dimensional form of the process zone sizes, $\lambda_s = (\ell_{c,s}/f_n)/h$ for the bulk and $\lambda_i = (\ell_{c,i}/f_n)/h$ for the interface, using some structural length h. Then we have $\xi_* = \ell_{k*}/h$, where ℓ_k is the length of the initial kink (if present), and the subscript $*$ stands for either substrate or interface regions. Fig. 5.1b shows in a sketchy form the regions covered by various authors. The horizontal axis includes both ξ, so there is some minor ambiguity which does not impair the description. Similarly for the values of λ_* in the vertical axis. Energy-based (LEFM) analyses (e.g., He and Hutchinson, 1989a; He et al., 1994, 2000) correspond to $\lambda_* = 0$. They invoke a preexisting kink along the interface, which has to be very small in comparison to any other characteristic dimension of the problem, so that asymptotic solutions for the crack-tip stress field can be used (Parmigiani and Thouless, 2006). Parmigiani and Thouless (2006) analyze the effect of kink size on fracture deflection by extending ℓ_k to values not necessarily negligible, and also reproducing the energy-based analysis of He and Hutchinson (1989a) and He et al. (1994) in the proper limit.

Fig. 5.2 shows in more detail available works that dealt with cohesive fracture, with no kinks. The two values λ_s and λ_i are now not collapsed onto a single axis. In this work (GHS1), we restrict the cohesive length to being much smaller than structural lengths, $\ell_{c,*} < 0.1h$, similar to the works of Strom and Parmigiani (2014) and Foulk III et al. (2008). On the other hand, it is seen that Parmigiani and Thouless (2006) covered regions where the cohesive length is not small compared to some structural length ($\ell_{c,*} \geq h$).

The objective of the present Chapter is to provide a more comprehensive analysis than what is currently available, in terms of simultaneously available data (interaction maps plus output variables) and the region in the parameter space covered, including the interaction angle.

In Section 5.4 we analyze the effect of strength and toughness of the substrate and interface on the interaction mode, using a cohesive zone model. We do not consider the presence of an initial kink. This analysis is labeled as $GHS1$ in Fig. 5.1b. In Section 5.5, we consider the effect of an initial defect or kink ($\ell_k > 0$), either on the interface or in bulk, on the interaction map. This analysis is labeled as GHS2 in Fig. 5.1b.

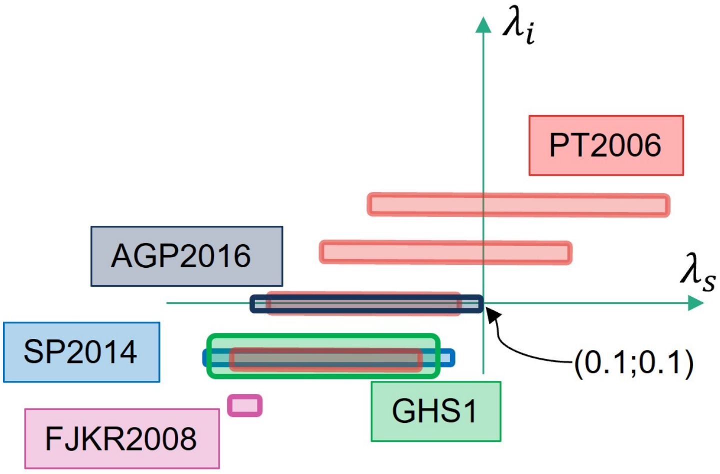

Figure 5.2: Schematic graph showing the ranges of non-dimensional cohesive lengths (on the interface λ_i and substrate λ_s) analyzed in the literature: Parmigiani and Thouless (2006) (PT2006), Foulk III et al. (2008) (FJKR2008), Strom and Parmigiani (2014) (SP2014), Alam et al. (2016) (AGP2016), Section 5.4 in this work (GHS1).

5.2 Model and geometry

This work is somewhat based on the study of Parmigiani and Thouless (2006), which is oriented to the analysis of the deflection vs. penetration problem, in a system that consists of a substrate with a deposited film of thickness h. A fracture crosses the film and impinges on the interface at an incidence angle ω with respect to the initial fracture. The original work considers a plane strain model with different substrate and film materials, as shown in Fig. 5.3, but we will restrict here consideration to the homogeneous case.

Therefore, the Young moduli are $E_s = E_f = E$ and the Poisson coefficients are $\nu_s = \nu_f = \nu$, so that the Dundurs' parameters (Dundurs, 1969) are $\alpha = \beta = 0$.

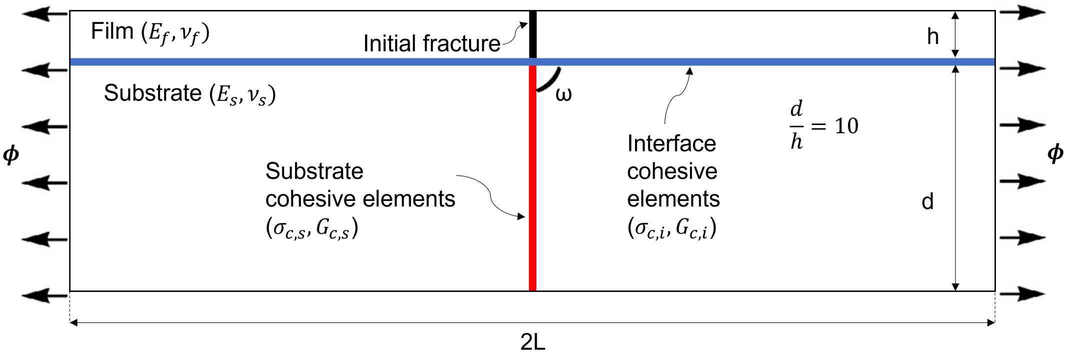

Figure 5.3: Model geometry (adapted from (Strom and Parmigiani, 2014)) showing the location of cohesive zone elements along the interface (blue) and ahead of the initial fracture in the substrate (red).

When a suitable remote loading σ is applied, both the interface and the substrate will be under traction that will tend to propagate the fracture. The dominant mode of propagation (substrate versus interface) and the value of applied load at which failure occurs depend on several parameters.

5.3 Energy-based analysis

The energy-based method of He and Hutchinson (1989a) and He et al. (1994) compares the energy release rates for a kink that extends by penetrating (P) the substrate across the interface, G_p, with that of a kink that deflects (D) along the interface, G_d. The condition for fracture deflection along the interface can be written as

$$r_{G_c} = \frac{G_{c,s}}{G_{c,i}} > \frac{G_p}{G_d} \quad . \tag{5.1}$$

This relation implies that, whenever the interface attains the critical state, the substrate did not do so yet. It can be applied to the configuration of Fig. 5.3, where the mode I stress intensity is (Tada et al., 1973)

$$K_I = 1.197\sigma\sqrt{\pi h} \quad , \tag{5.2}$$

with applied remote stress σ and initial fracture length h. Inserting in Eq. (5.2) the relation ${K_{Ics}}^2 = E' G_{c,s}$, i.e., the critical value of K_I for propagation in the substrate, where $E' = E/(1-\nu^2)$ is the Young's modulus in plane strain, at the critical point it will be

$$\sqrt{E' G_{c,s}} = 1.197 \sigma_{0p} \sqrt{\pi h} \quad . \tag{5.3}$$

A non-dimensional critical traction for propagation of a kink in the substrate will be

$$\phi_p = \sigma_{0p} \sqrt{\frac{h}{E' G_{c,i}}} = \frac{1}{1.197\sqrt{\pi}} \sqrt{\frac{G_{c,s}}{G_{c,i}}} \quad . \tag{5.4}$$

The non-dimensional critical traction for propagation of a kink in deflection ϕ_d depends on the angle of incidence, and it can be obtained by combining Eq. (5.2) with the expression given by He and Hutchinson (1989a) for the ratio G_d/G_p. In the particular case of $\omega = 90°$, analyzed in detail by Strom and Parmigiani (2014),

$$G_d = 0.2608 {K_I}^2 / E' \quad . \tag{5.5}$$

Since $G_{c,i} = G_d$ during propagation, we have

$$\phi_d = \sigma_{0d} \sqrt{\frac{h}{E' G_{c,i}}} = 0.923 \quad . \tag{5.6}$$

This quantity can be calculated similarly for other angles of incidence.

According to He and Hutchinson (1989a), fracture propagation occurs in the mode requiring the lowest applied stress. The transition between modes for increasing values of the ratio $r_G = G_{c,s}/G_{c,i}$, from the penetration mode to the deflection mode, occurs at the transition value $r_{Gt} = 3.84$. The values of $\sigma_{c,s}$ and $\sigma_{c,i}$ are irrelevant in this analysis, as expected in LEFM.

5.4 LEFM vs. cohesive model solutions for crack deflection at interfaces

In this section we study the main differences on fracture deflection between energy-based methods and mixed-methods, by using the cohesive model described in section 3.2.2.

Both the interface and the substrate ahead of the initial crack are populated with cohesive elements. The complete set of physical parameters of the system is E, ν, $G_{c,s}$, $\sigma_{c,s}$, β_s, $G_{c,i}$, $\sigma_{c,i}$, β_i, ω, h, L, d, σ. As compared to the hydraulic fracturing case of Ch. 4, in addition to the simpler phenomenology and equations involved here, it is readily apparent that we are dealing also with a simpler parameter space, albeit yet with too many variables. Using the fully developed cohesive zone lengths $\ell_{c,s} = f_n E' G_{c,s}/{\sigma_{c,s}}^2$ and $\ell_{c,i} = f_n E' G_{c,i}/{\sigma_{c,i}}^2$, the following non-dimensional groups are considered: r_{G_c}, r_{σ_c}, β_s, β_i, $\lambda_i = \ell_{c,i}/f_n h$, $G_{c,i}/E'h$, d/h, L/h, $\phi = \sigma\sqrt{h/E'G_{c,i}}$. Throughout this work $G_{c,i}/E'h = 1 \times 10^{-6}$, $\beta_s = \beta_i = 1$, and $d/h = 10$.

To ensure accurate results, a minimum of five finite elements were employed to resolve the fully developed cohesive zones on both the substrate and interface ($\ell_c \geq 5\ell_e$). In order to satisfy this criterion, the finite element size ranged from 2×10^{-4} m to 2×10^{-3} m.

We used two different methods to apply loading on the sample. The first method replicated work by Parmigiani and coworkers (e.g., Parmigiani and Thouless, 2006), whereby uniform displacement on the lateral faces was increased in small steps, until the first element is fully decohered, either at the interface or at the substrate. This is regarded as the critical point with its associated failure load. The sample dimensions also replicated the cited work, with $L/h = 220$. This way, we closely reproduced the overall configuration and conditions of Parmigiani and coworkers.

Once we verified that our initial results (BC-u in Fig. 5.4 below) matched those of Parmigiani and Thouless (2006) (comparison not shown here), we shifted to a different combination of boundary conditions, loading method and sample configuration, leading to several enhancements, enumerated in what follows, in the simulation of crack propagation. Instead of uniform lateral displacement boundary conditions, we applied displacements associated with the so-called modified boundary layer (BC-MBL, (e.g., Anderson, 2017)), described in detail in Sec. A.1.1. This allowed for (1) precisely controlled values of K_I and K_{II} across propagation. The new loading algorithm is described in detail in Sec. A.1.2. This algorithm provides the following improvements: (2) more stable propagation across longer crack extensions, and (3) better identification and isolation of causes for discontinuous propagation. Finally, we changed to a configuration with $L/h = d/h = 10$, i.e., less elongated. This shape is (4) more versatile for changing configuration, e.g., the incidence angle.

A first series of simulations, with varying r_{G_c} and $\lambda_s = \lambda_i = 0.01$, were performed to compare the old and new setups just described. The results are shown in Fig. 5.4. The curves represent predictions of failure loads in both penetration and deflection modes as outlined by He and Hutchinson (1989a) based on LEFM, given by Eqs. (5.4) and (5.6) for interfaces at $\omega = 90°$. The point at which the curves intersect signals the transition. Symbols show results from calculations under BC-u and BC-ML configurations, also showing deflection or penetration modes.

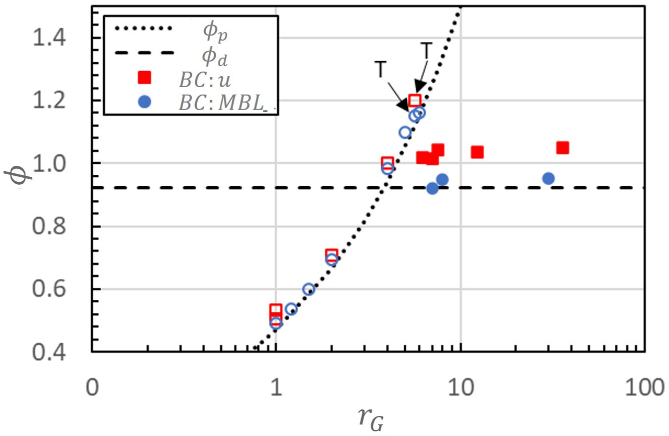

Figure 5.4: Non-dimensional critical load ϕ as a function of the ratio of substrate to interface toughness r_G. Lines correspond to predictions from LEFM, dotted curve for penetration, horizontal dashed line for deflection. Symbols correspond to simulations with $G_{c,i}/E'h = 10^{-6}$, $\lambda_i = \lambda_s = 0.01$, with displacement boundary condition (squares) and MBL-type boundary conditions (circles). Filled symbols indicate deflection, empty symbols penetration, and the letter T indicates transition.

The first observation is that the results with both configurations were similar, as expected. Moreover, failure loads for the deflection mode were in slightly better agreement with results from LEFM. Therefore, after verifying that the new setup and loading algorithm provided similar results as the original one, we kept using the new one for the remainder of the work. Second, it was observed that the transition point moved away from predictions of LEFM. Next to the transition point, there is a range of conditions r_{G_c} that change the propagation mode, from deflection to penetration, when changing the crack tip process from purely elastic (LEFM) to cohesive (CZM). This change has an associated increase in failure load within that range of r_{G_c}, and an increase in ϕ and r_G at transition. This agrees qualitatively with the results obtained by Strom and Parmigiani (2014). From the mechanistic point of view, in the transition region both propagation modes compete, and during the incremental application of the remote load both process zones develop simultaneously, which implies a higher energy consumption. Away from the transition zone, the dominant propagation mode is essentially the only one that develops a process zone, and the required load values match those predicted by the LEFM.

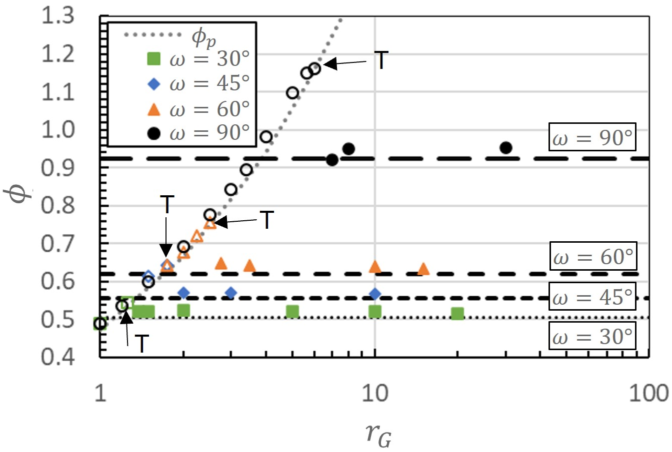

Figure 5.5: Non-dimensional critical load ϕ as a function of the ratio of substrate to interface fracture energy r_G for interaction angles 30°, 45°, 60°, and 90°, with $G_{c,i}/E'h = 10^{-6}$, $\lambda_i = \lambda_s = 0.01$, and MBL boundary conditions. Lines show predictions from LEFM. Filled symbols indicate deflection, empty symbols penetration, and T, transition.

We then replicated the analysis for other interaction angles. The results for critical load as a function of r_G are shown in Fig. 5.5. The respective intersections signal the corresponding mode transition points. Filled symbols indicate deflection, empty symbols penetration, and the letter T indicates transition. The result for all angles of incidence is qualitatively the same as described above in connection with Fig. 5.4, namely, the peak load and r_{G_c} at transition increase with respect to LEFM predictions.

From Fig. 5.5 we extracted the values r_{Gt} and ϕ_t at the transition point for each angle of incidence. These results are shown in Fig. 5.6, along with the available results from Parmigiani and Thouless (2006); Foulk III et al. (2008); Strom and Parmigiani (2014). The qualitative behavior is in all cases the same. As the incident angle decreases, the toughness ratio r_{Gt} required to promote deflection is reduced, approaching the value predicted by LEFM, $r_{Gt,LEFM}$. A similar trend is observed for the failure load ϕ_t, as compared to the corresponding values $\phi_{t,LEFM}$ from LEFM. Similar results where obtained for several interaction angles in the work by Grimm (2012). The quantitative differences among the various calculations may be due to the different cohesive laws used. The figure shows that our study provides more complete data, including simultaneously r_{Gt} and ϕ_t.

Since the cause of the deviation of the results from those predicted by LEFM is the development of cohesive zones, we examined the effect of the relative sizes of the cohesive zones $\ell_{c,s}$ and $\ell_{c,i}$ at the substrate and interface, respectively. For that sake, we vary

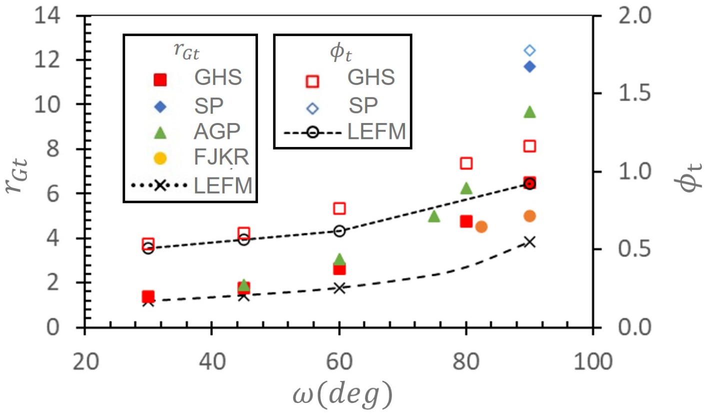

Figure 5.6: Comparison of data for the ratio r_{Gt} and non-dimensional critical load ϕ_t at transition, as a function of incidence angle between, from various sources; results of this work (GHS), (Strom and Parmigiani, 2014) (SP), (Alam et al., 2016) (AGP), (Foulk III et al., 2008) (FJKR) and linear elastic fracture mechanics (LEFM) (He and Hutchinson, 1989a).

the characteristic length λ_s covering a range of values $r_\lambda = \lambda_s/\lambda_i = \ell_{c,s}/\ell_{c,i} = 0.1, 1, 10$, thus expanding the analysis of Fig. 5.5. Since the cohesive zone is a concept unrelated to LEFM, this variation does not impact its predictions.

The results are shown in Fig. 5.7. It can be seen that when $\lambda_s/\lambda_i \gg 1$ there is a considerable increase in the transition ratio r_{Gt} with respect to the value predicted by LEFM. From a mechanistic point of view, when the cohesive zone in the substrate is elongated ($\ell_{c,s}/\ell_{c,i}$ increases), this eventually inhibits propagation in the deflection mode, even though from an energy point of view it would be favorable ($\phi_d < \phi_p$). The penetration mode is stabilized with respect to deflection in this condition. On the other hand, when $\lambda_s/\lambda_i \ll 1$, r_G is less than the value predicted by LEFM. When the cohesive zone in the substrate is shortened ($\ell_{c,s}/\ell_{c,i}$ decreases), this inhibits propagation in the penetration mode, even though from an energy point of view it would be favorable ($\phi_d > \phi_p$). The deflection mode is stabilized. This general trend is observed for all angles of incidence.

To better understand the competition between the evolving actual cohesive lengths in the substrate and interface as obtained in the simulations ($L_{c,s}$ and $L_{c,i}$ respectively), we analyzed their evolution as loading proceeds. $L_{c,s}$ and $L_{c,i}$ were calculated in each simulation step as the sum of the length of the damaged elements (i.e. elements with $\delta_{max} > 0$) but not completely decohered (i.e. elements with $\delta_{max} < \delta_c$). Non-dimensional values are obtained by normalizing with the respective theoretical, fully developed co-

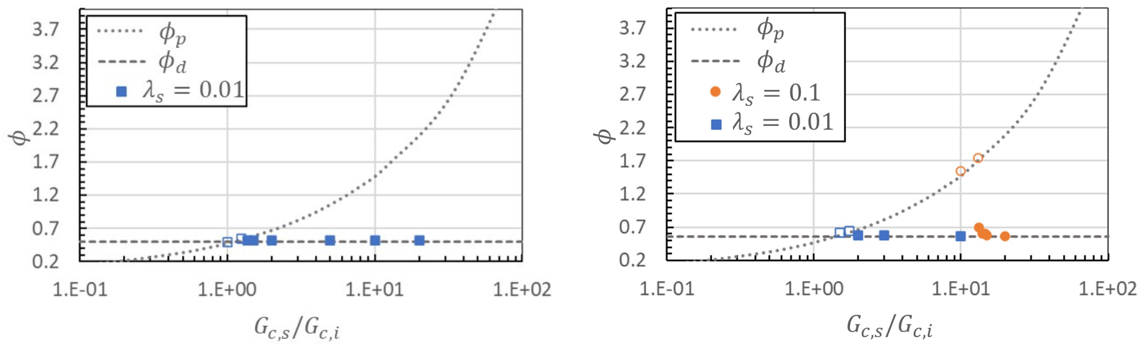

(a) $\omega = 30°$.

(b) $\omega = 45°$.

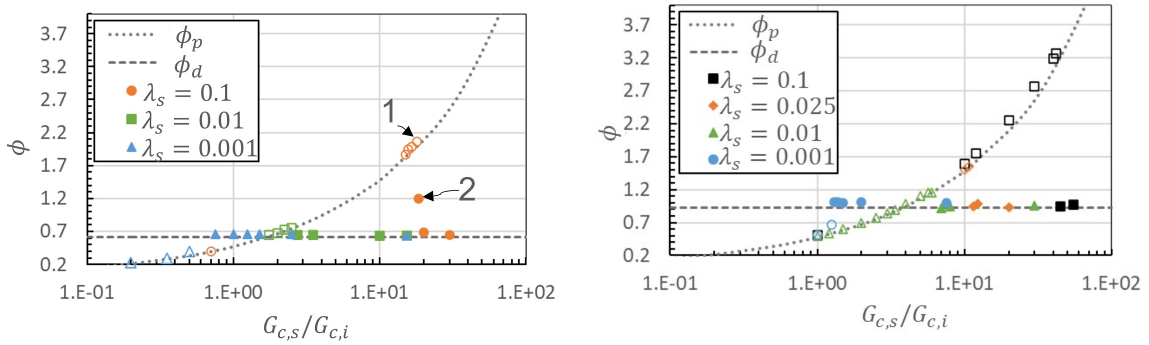

(c) $\omega = 60°$.

(d) $\omega = 90°$.

Figure 5.7: Non-dimensional critical load as a function of the ratio of fracture energies of the substrate to the interface (r_G) for simulations at different interaction angles. $G_{c,i}/E'h = 10^{-6}$, $\lambda_i = 0.01$, and varying the parameter $\lambda_s = [0.001, 0.01, 0.025, 0.1]$. Empty symbols indicate penetration, filled symbols deflection.

hesive zone lengths (Eq. (4.1)) $r_{Ls} = L_{c,s}/\ell_{c,s}$ and $r_{Li} = L_{c,i}/\ell_{c,i}$, so the values can be visualized simultaneously in a single plot. For this analysis two simulations were selected, at either side of the transition point as marked with numbers 1 and 2 in Fig. 5.7c, in order to evaluate the differences between seemingly similar conditions.

Fig. 5.8 shows the results for r_{Ls} and r_{Li}, for cases 1 and 2, as a function of the remote non-dimensional load ϕ. The initial part of the decohesion process is quite similar up until a remote load $\phi \approx 1.1$, with a sizable fraction of both cohesive zones already developed. Beyond that point, growth of the cohesive zone on the interface in case 1 (where deflection is the LEFM preferred mode) stagnates. The concurrent growth of the cohesive zone in the substrate moves the stress peak away from the interface, thus decreasing the driving force for further extension along the interface. This process continues, leading to final shrinkage of the cohesive zones on the interface and in bulk in simulations 1 and 2, respectively. A few other points are revealed by Fig. 5.8.

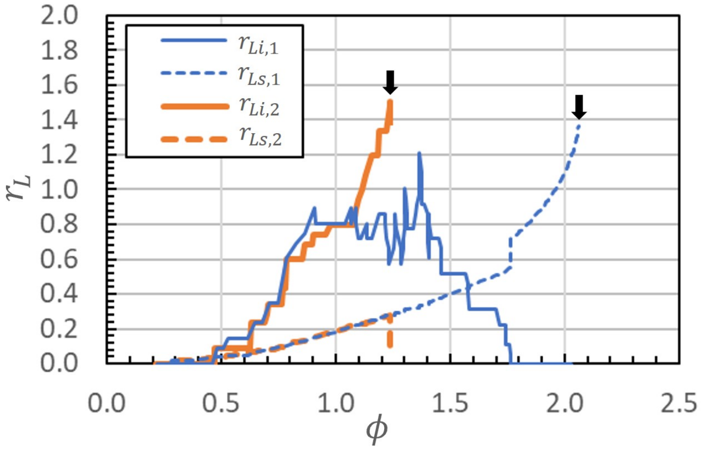

Figure 5.8: Comparison of the calculated to theoretical cohesive length ratio for substrate ($r_{Ls} = L_{c,s}/\ell_{c,s}$) and interface ($r_{Li} = L_{c,i}/\ell_{c,i}$) for simulations with $\omega = 60°$ and $r_\lambda = 10$. The arrows show the propagation load for each simulation.

First, there appears to be a difference between cases 1 and 2 in the way the non-dominant cohesive zone recedes. In case 2 the cohesive zone in the substrate appears to snap closed at its critical load $\phi_t \approx 1.23$. This points to a possible instability in the evolution of the system, a topic that was barely mentioned in the literature. On the other hand, in case 1 the cohesive zone on the interface gradually shrinks as the load is increased. Only at the point of its final closure there appears to be a minor snap in the progressively opening cohesive zone in the substrate. Moreover, this final closure takes place at a load well below the critical value $\phi_t \approx 2.1$. We defer further discussion on this topic to a later section.

Second, and even if it is not completely evident from Fig. 5.8, there is some propagation after the critical point that takes place at essentially constant load and cohesive length of the dominant mode. From preliminary tests, this initial propagation appears to involve small snaps in both cases, pointing again at some instability of crack propagation.

Third, crack propagation in either of the dominant modes appears to proceed at the same approximate ratio 1.4-1.5, consistent with the idea that whenever the interaction is resolved, crack propagation features are determined by the local conditions.

To further analyze the implications of our simulation results, we present a diagram that explores the interplay between critical traction and toughness ratios. Using the simulations presented in Fig. 5.7, we derived values for r_G and r_σ, which were then used

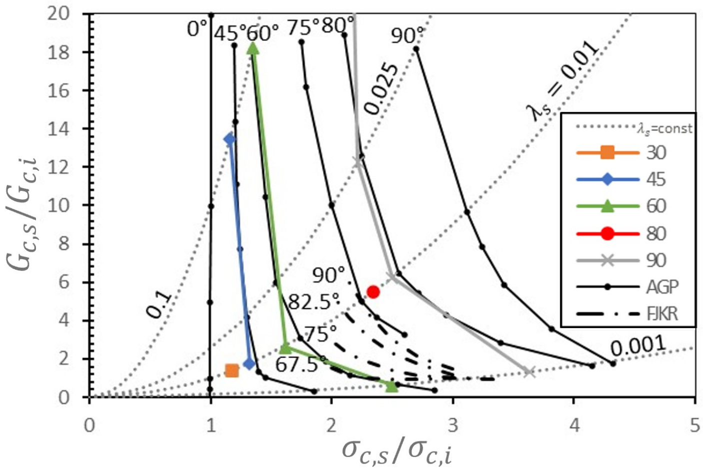

Figure 5.9: Ratio of substrate fracture energies over the interface ($G_{c,s}/G_{c,i}$) as a function of the ratio of substrate resistances over the interface ($\sigma_{c,s}/\sigma_{c,i}$) for simulations at different angles of incidence (30°, 45°, 60° and 90°). The parameters $\lambda_i = E'G_{c,i}/{\sigma_{c,i}}^2 h = 0.01$ and $G_{c,i}/E'h = 10^{-6}$ were kept constant, and the values of the parameter $\lambda_s = E'G_{c,s}/{\sigma_{c,s}}^2 h$ are indicated on the λ_s iso-lines. The results of the transitions are indicated with colored symbols according to the angle of incidence. The results of Alam et al. (2016) (AGP) and Foulk III et al. (2008) (FJKR) are represented with filled lines and with lines and dots, respectively.

to create the propagation mode diagram shown in Fig. 5.9. This diagram also includes the results of Alam et al. (2016) and Foulk III et al. (2008), all showing qualitative agreement.

Similarly as in Fig. 5.7, our results are in between those from literature, with larger discrepancies for high incidence angles. Foulk III et al. (2008) explored a limited range of the parameter space ($r_\sigma = \sigma_{c,s}/\sigma_{c,i}$ between 2 and 3.5). For an angle of 60° they only observed intergranular propagation (i.e., deflection). This figure illustrates in an alternative way the result described above, i.e., by varying the ratio of critical tractions r_σ at constant r_G (which implies varying the ratio of cohesive lengths), the dominant mode of propagation can be altered. This result is in contrast to LEFM predictions.

In addition to the effect on the dominant mode of propagation, the presence of process zones in conditions of interaction between a propagating fracture and an interface can increase the propagation load, and hence the toughness of the structure, even for fractures propagating in the substrate, again in contrast to LEFM predictions. This increase does not appear when there is a process zone in propagation in the substrate with no other competing cohesive zone. In the following section we analyze the effect of increasing the size of the substrate cohesive zone while keeping constant the size of the interface cohesive zone.

5.4.1 Effect of cohesive length mismatch

In this section we analyze in detail the effect of modifying the substrate to interface cohesive length ratio on the interaction mode. To this purpose, we selected three simulations with interface angle $\omega = 60°$, $r_G = 15$, and varied the non-dimensional cohesive length on the substrate by 2 orders of magnitude ($\lambda_s = 0.1$, 0.01 and 0.001) keeping $\lambda_i = 0.01$, see Fig. 5.7c.

Fig. 5.10 shows the ratios of calculated to theoretical cohesive lengths for the substrate ($r_{Ls} = L_{c,s}/\ell_{c,s}$) and the interface ($r_{Li} = L_{c,i}/\ell_{c,i}$). We divided the interface lengths into upward ($L_{c,i,up}$) and downward ($L_{c,i,dn}$) to see more clearly which branch of the interface is opening. On the next paragraph we analyze simulations results one by one.

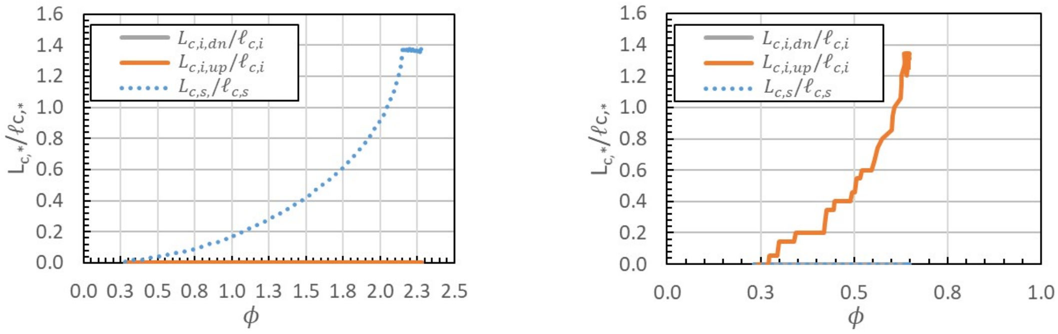

(a) $\lambda_s = 0.1$, $r_\lambda = 10$.

(b) $\lambda_s = 0.01$, $r_\lambda = 1$.

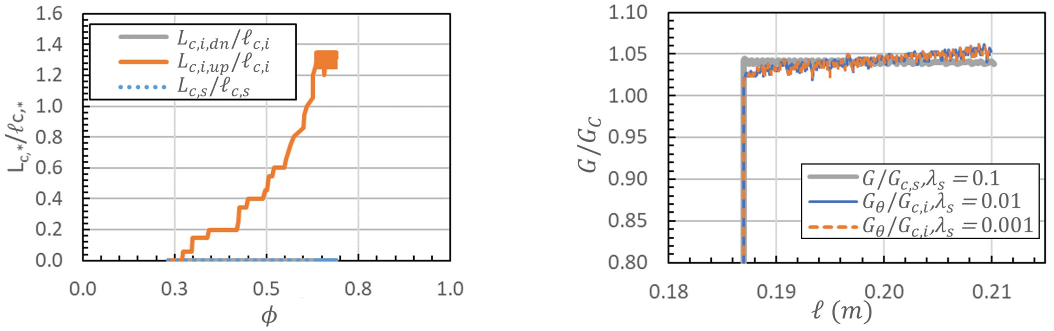

(c) $\lambda_s = 0.001$, $r_\lambda = 0.1$.

(d) Energy ratio.

Figure 5.10: *a)*, *b)* and *c)* Cohesive lengths development at the interface, upward ($L_{c,i,up}$), and downward ($L_{c,i,dn}$) and on the substrate ($L_{c,s}$). *d)* Energy ratio (G/G_c) for three simulations with $\ell_{c,s} = 0.001$, 0.01 and 0.1. Energy ratios are calculated as $G/G_{c,s}$ for the simulation propagating on the substrate ($\ell_{c,s} = 0.1$) and as $G_\theta/G_{c,i}$ for the simulations propagating on the interface ($\ell_{c,s} = 0.01, 0.001$).

On simulation (*b*), with $\lambda_s = 0.01$, both substrate and interface theoretical cohesive lengths are equal ($r_\lambda = 1$). In Fig. 5.10b is shown that the cohesive length is only developed on the upward interface, indicated with an orange line. $L_{c,i,up}$ increases its size as the applied load increases, up to a value 30% higher than the theoretical length, then the fracture propagates at constant $L_{c,i,up}$. Similar results were obtained on simulation (c), with $r_\lambda = 0.1$ as shown in Fig. 5.10c. In this simulation, also the upward interface cohesive length was developed. To sum up, decreasing the cohesive length of the substrate by an order of magnitude did not change the deflection behavior.

Now, going to simulation (a), when we increase $\ell_{c,s}$ an order of magnitude with respect to $\ell_{c,i}$, the interaction mode changes to penetration, as shown in Fig. 5.10a. Here we can see that the cohesive length is only developed on the substrate and $L_{c,i}$ is kept at zero during the entire simulation.

We can calculate the Energy Release Rate for the fracture, or G, by Irwin's relationship (Irwin, 1957) as

$$G = \frac{{K_I}^2 + {K_{II}}^2}{E'}, \tag{5.7}$$

where E' is the young modulus in plane strain. And we can estimate the Energy Release Rate on the interface with the expression for the ERR on a kink oriented at an angle θ as

$$G_\theta = \frac{\cos^2\frac{\theta}{2}[{K_I}^2 + 5{K_{II}}^2 + ({K_I}^2 - 3{K_{II}}^2)\cos\theta - 4K_I K_{II}\sin\theta]}{2E'} \quad , \tag{5.8}$$

where K_I and K_{II} are the stress intensity factors of the main fracture, in mode I and II respectively. Te derivation of this equation can be found in the Appendix.

Fig. 5.10d shows the evolution of the ratios of the energy release rate for the three cases, calculated as $G/G_{c,s}$ for the case of penetration mode (c) and as $G_\theta/G_{c,i}$ for the other two cases of deflection mode (a and b). Here we see that propagation occurs at $G = G_c$ with about 4% error in the three cases. One fact to note is that propagation over interfaces has a small increase in G during propagation. A similar effect was found in simulations without geometric propagation line. These results are shown in the Appendix.

Fig. 5.11 shows contour pots of effective stress for the three cases analyzed, in two stages of the simulations: when the load is such that the first cohesive element opens ($\phi = 0.32$) and when the load reaches the critical value on the interface according to LEFM ($\phi = 0.61$). The fractured and cohesive zones are colored in magenta and yellow lines, respectively. The effective stress is calculated as

$$\sigma_e = \frac{1}{\sqrt{2}}\left[(\sigma_1 - \sigma_2)^2 + (\sigma_1 - \sigma_3)^2 + (\sigma_2 - \sigma_3)^2\right]^{1/2} \quad , \tag{5.9}$$

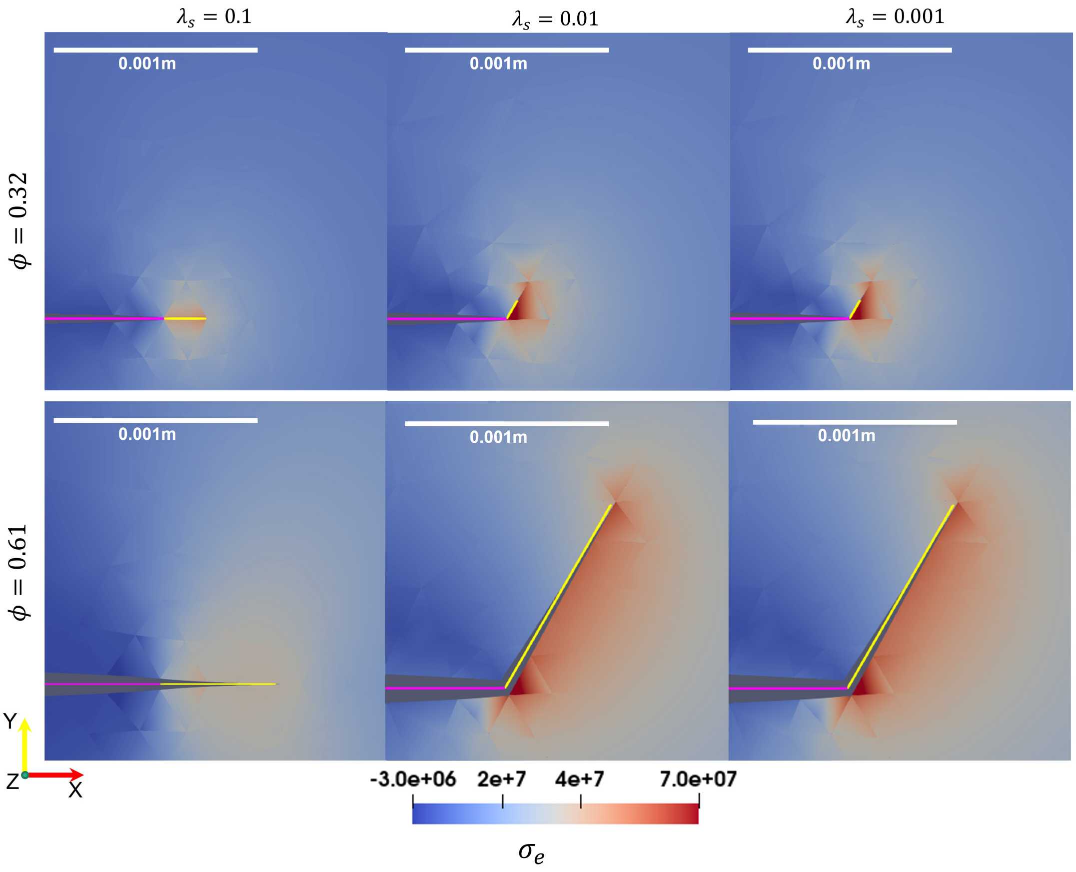

Figure 5.11: Effective von Mises Stress distribution for three simulations with different cohesive substrate length $\lambda_s = 0.1, 0.01, 0.001$ with a remote non-dimensional load $\phi = 0.32$ and $\phi = 0.61 = \phi_d$. The scale indicates the length of the cohesive zone of the interface, $\ell_{c,i} = 1.0 \times 10^{-3}$ m.

where σ_1, σ_2 and σ_3 are the three principal stresses, and σ_e is the effective von Mises Stress (Anderson, 2017).

By inspecting the cohesive zones at $\phi = 0.32$, we see the stress redistribution from the interface towards the substrate by increasing $\ell_{c,s}$ one order of magnitude from $\ell_{c,s} = 0.01$ to $\ell_{c,s} = 0.1$. This shows that already at low loads, at the beginning of the development of the cohesive zone, the cohesive length of the substrate inhibits propagation across the interface. This remarks the effectiveness of the cohesive lengths ratio in modifying the interaction mode.

To see this effect more clearly, we plotted the normal, tangential and effective traction (t_n, t_t and t_e respectively), the normal, tangential and effective separation (δ_n, δ_t and δ_e respectively), on the cohesive zones, and the tangent to normal ratios (or the tangent of the phase angles), $\tan(\Phi) = t_t/t_n$ and $\tan(\Psi) = \delta_t/\delta_n$ in Fig. 5.12 for $\phi = 0.32$, and in Fig. 5.13 for $\phi = 0.61$. The results for the simulation (c), with $\lambda_s = 0.001$ are not shown because they are identical to simulation (b), with $\lambda_s = 0.01$.

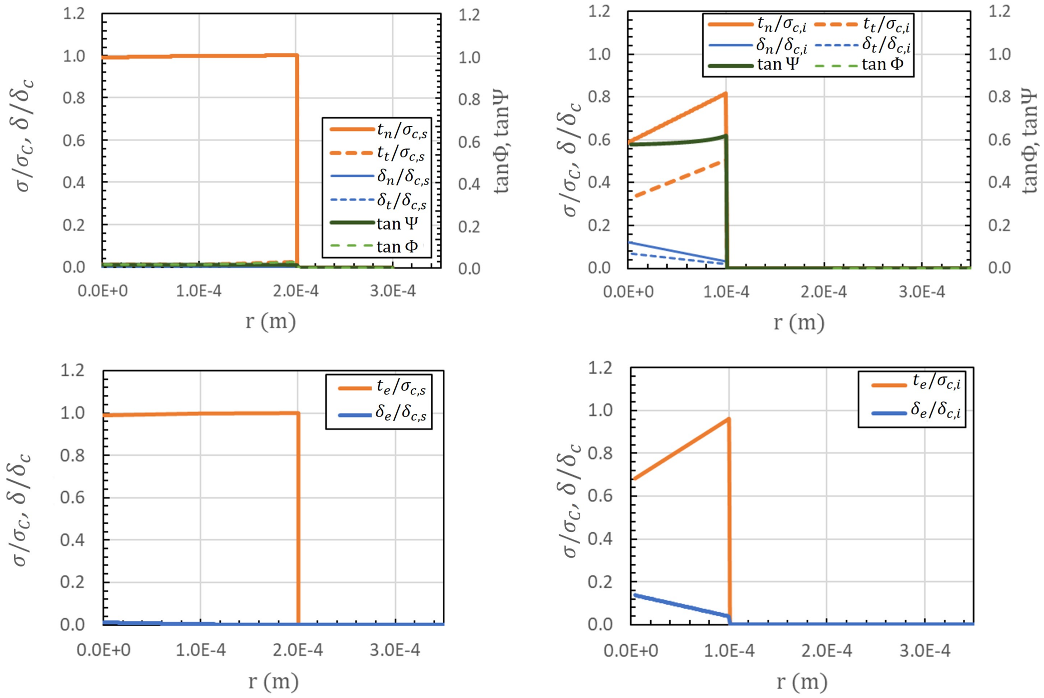

(a) $\lambda_s = 0.1$.

(b) $\lambda_s = 0.01$.

Figure 5.12: Traction-separation parameters with remote load $\phi = 0.32$. In upper graphs are the normalized cohesive separation and traction in normal and tangential directions for two simulations with cohesive substrate length: $\lambda_s = 0.1$ and 0.01 normalized with substrate and interface critical values respectively. In lower graphs are the normalized effective traction and separation. In all plots r is the coordinate axis with zero at the initial fracture tip on the propagation line: on the substrate for $\lambda_s = 0.1$ and on the interface for $\lambda_s = 0.01$.

In simulation (a), the cohesive zone is developed on the substrate, so the traction is normalized with $\sigma_{c,s}$, and the separation with $\delta_{c,s}$. In simulation (b), the dominant cohesive zone is on the interface, so the traction is normalized with $\sigma_{c,i}$, and the separation with $\delta_{c,i}$.

In Fig. 5.12 we can compare the initial stage of the cohesive zones in both cases. In simulation (a), on the left, the separation on the substrate is almost zero and the normal traction reach the critical value $\sigma_{c,s}$. As expected for a fracture propagating in a straight line, tangential traction and separation are zero, and therefore $\tan(\Phi) = \tan(\Psi) = 0$, and the effective traction and separation are identical to the normal traction and separation, respectively. The same behavior can be observed at a higher remote load in Fig. 5.13.

In simulation (b), at the right of Fig. 5.12, the separation on the interface decreases from a maximum value on the fracture tip ($r = 0$) to zero at the end of the cohesive zone ($r = L_{c,i} = 1.0 \times 10^{-4}$ m). This cohesive zone is not fully developed, as the maximum

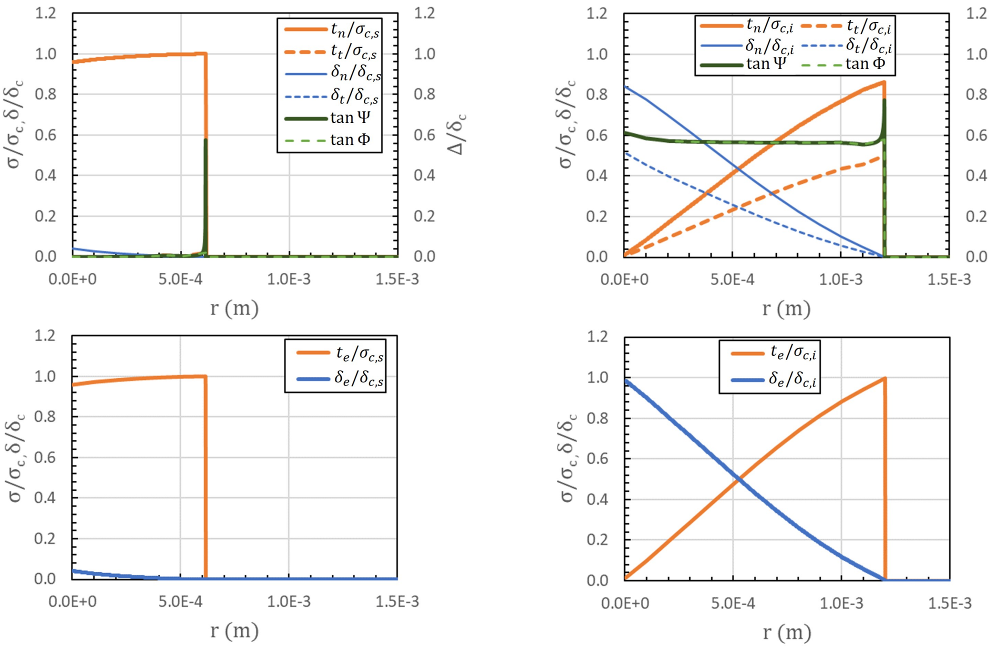

(a) $\lambda_s = 0.1$.

(b) $\lambda_s = 0.01$.

Figure 5.13: Traction-separation parameters with remote load $\phi = 0.61$. In upper graphs are the normalized cohesive separation and traction in normal and tangential directions for two simulations with cohesive substrate length: $\lambda_s = 0.1$ and 0.01 normalized with substrate and interface critical values respectively . In lower graphs are the normalized effective traction and separation. In all plots r is the coordinate axis with zero at the initial fracture tip on the propagation line: on the substrate for $\lambda_s = 0.1$ and on the interface for $\lambda_s = 0.01$.

separation did not reach the critical value $\delta_{c,i}$. The normal and tangential traction have the maximum value at $r = \ell_{c,i}$, being the effective traction close to $\sigma_{c,i}$, and decrease linearly with r. Both phase angles $\tan(\Phi) = \tan(\Psi) \approx 0.6$ are equal and constant on the cohesive zone, this will be discussed further below.

By increasing the remote load to $\phi = 0.61 \approx \phi_d$, according to LEFM, the fracture should propagate through the interface. In Fig. 5.13 we can appreciate that on simulation (b) the cohesive length is fully developed, $t_e = \sigma_{c,i}$ in $r = L_{c,i}$ and $\delta_e = \delta_{c,i}$ in $r = 0$. Both phase angles $\tan(\Phi) = \tan(\Psi) \approx 0.6$ are equal and constant on the cohesive zone. The fact that they are equal is a consequence of the effective cohesive law (non demonstrated here).

In simulation (a), on the left of Fig. 5.13, the cohesive length is not completely developed and the separation is small compared to $\delta_{c,s}$. This occurs because the theoretical cohesive length on the substrate is 10 times greater than on the interface, and the neces-

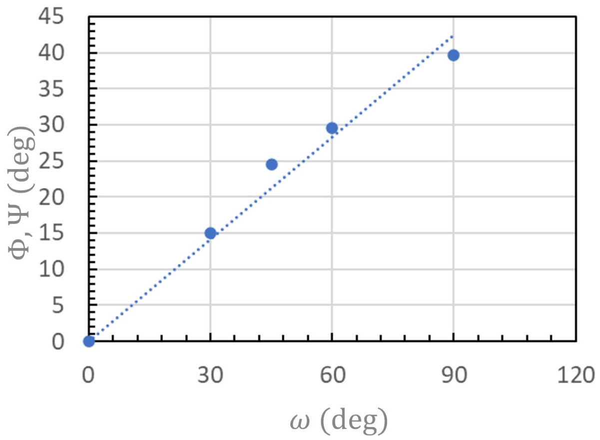

Figure 5.14: Phase angles Φ and Ψ obtained for various interface angles ω.

sary remote load to penetrate into the substrate is greater too. In this case, phase angles are both zero at all remote load values, because there are not a tangential component on the traction nor the separation.

We studied the effect of the interface angle on phase angles. Fig. 5.14 shows the phase angles ($\Phi = \Psi$) obtained for various interface angles, and it is shown that the phase angle increase as the interface angle increases with a linear upward trend. This is as expected, since the tangential component is greater as the interface angle increases. Also, it has to pass through the point (0,0) since in a straight propagation fracture it has no tangential components of the traction and separation.

Finally, after the detailed analysis on the cohesive lengths mismatch, we can conclude that the relative size of interface and substrate cohesive zones can modify the interaction mode. It is remarkable how the increase in substrate cohesive length can inhibit deflection at the interface to such an extent that there is no competition between the two cohesive zones, but rather, once the cohesive zone begins to develop in the substrate, it increases in length until it reaches a constant value. Summarizing, by increasing substrate cohesive length with respect to the interface cohesive length, deflection is inhibited. The opposite occurs when interface cohesive length is increased with respect to the substrate cohesive length.

Another important conclusion is that phase angles are constant on the cohesive length and depend linearly on the interface angle and do not depend on the remote load.

5.4.2 Approximate universality of toughness ratio and propagation load at transition

We have seen above that the relative sizes of cohesive zones r_λ can have an impact on the dominant propagation mode for cohesive fractures, as opposed to what LEFM dictates. In this section we explore systematically such differences, as regards toughness transition ratios and non-dimensional transition load. For this study we include the results obtained in this work and the results available in the literature.

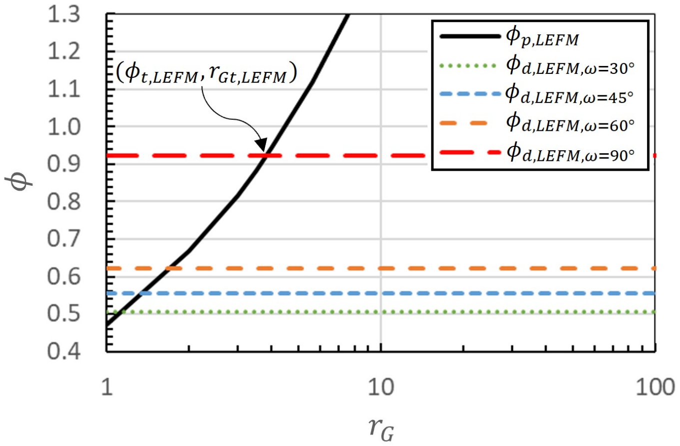

Figure 5.15: Non dimensional propagation load for deflection and penetration as a function of toughness ratio predicted by LEFM. In deflection the non dimensional load depends on the interface angle ω. The transition non dimensional load ($\phi_{t,LEFM}$) and toughness ratio ($r_{Gt,LEFM}$) for an interface at $\omega = 90°$ is indicated.

As described in the previous section, LEFM predicts a transition mode, from deflection to penetration at a certain toughness ratio, $r_{Gt,LEFM}$, and non dimensional load, $\phi_{t,LEFM}$. This is shown in the plot of Fig. 5.15. The intersection for an interface with angle $\omega = 90°$ is indicated as an example. On the other hand, we obtained values for the transition toughness, r_{Gt}, and non dimensional load, ϕ_t, via cohesive zone modeling.

Fig. 5.16a shows a summary of data for r_{Gt} from our work and the literature, covering a wide range of conditions. Fig. 5.16b shows corresponding data for ϕ_t. In both cases, a general trend according to the analysis above is observed, but variations across sources, and in particular as affected by the incidence angle, are noticeable.

Given that tilting the interface, with other physical parameters keeping constant, affects in a qualitatively similar manner the results from LEFM and cohesive modeling (see Fig. 5.6), we evaluate this variation more quantitatively. Normalizing r_{Gt} with the

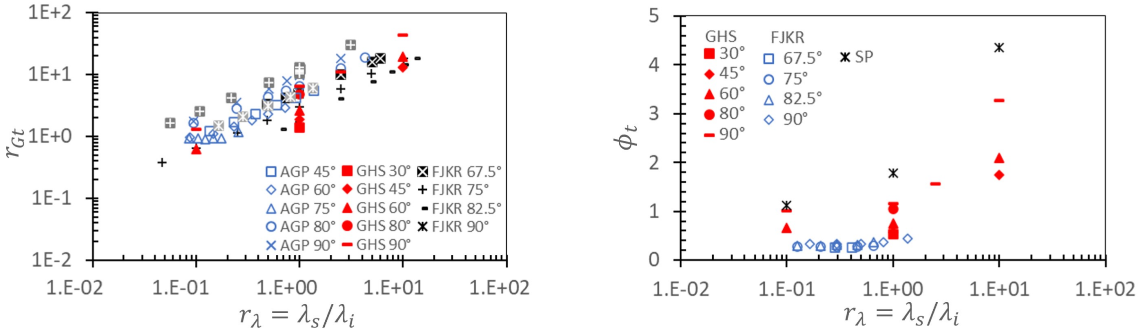

(a) Transition toughness ratio. (b) Transition non-dimensional load.

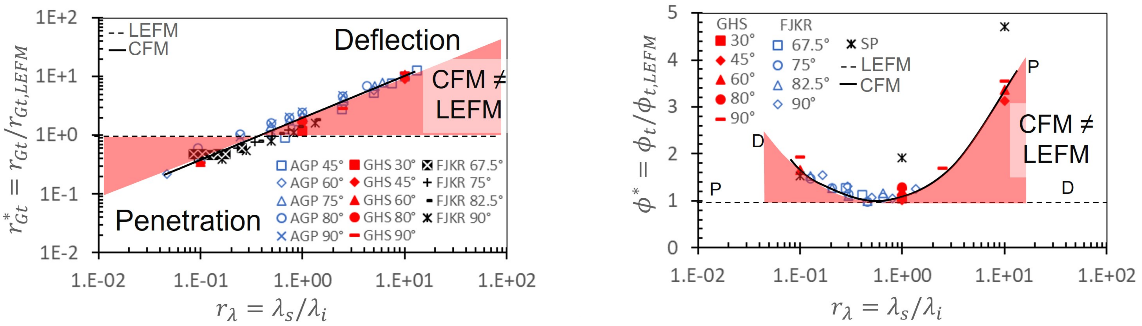

(c) Normalized transition toughness ratio. (d) Normalized transition non dimensional load.

Figure 5.16: Approximate universality in r_G and ϕ vs. r_λ. Highlighted red areas indicate zones where predictions based on LEFM and cohesive models differ.

predicted transition toughness ratio from LEFM we get $r^*_{Gt} = r_{Gt}/r_{Gt,LEFM}$. Similarly, by normalizing the maximum non-dimensional transition load with the corresponding LEFM transition load, $\phi_{t,LEFM}$, we obtain $\phi^* = \phi_t/\phi_{t,LEFM}$.

Figs. 5.16c and 5.16d show the variations of the normalized non-dimensional quantities above. It is apparent that an approximately universal behavior emerges for all angles of incidence. This is an empirical finding, and we conjecture that a further dimensional analysis might provide some insight into its underlying causes. We include the results from literature (PT, SP, AGP and FJKR). Highlighted red areas indicate zones where cohesive models disagree with LEFM predictions (dashed lines).

The r^*_{Gt} vs. r_λ mechanism map for all analyzed interaction angles is shown in Fig. 5.16c. The universal line divides the interaction mode between penetration and deflection. The intersection between the universal line and the LEFM prediction, $r^*_{Gt} = 1$, is at $r_\lambda \approx 0.45$. At that point both criteria are roughly coincident and as r_λ takes higher or lower values the difference between both lines gets bigger (red areas).

The variation of ϕ^* as a function of r_λ is shown in Fig. 5.16d. It is observed that the markers corresponding to our simulations (GHS), the simulations from Foulk III et al. (2008) and Strom and Parmigiani (2014) fall on an approximately universal curve for all analyzed angles. This curve represents the universal ϕ^* predicted for Cohesive Fracture Mechanics. In dashed line is shown the LEFM prediction, which corresponds to the value $\phi^* = 1$. The intersection between both curves is again in $r_\lambda \approx 0.45$. This intersection must be at the same r_λ value in both universal curves, since ϕ_t follows the trajectory of the critical load associated with LEFM, and if a given r_λ gives $r_{Gt} = r_{Gt,LEFM}$, then $\phi_t = \phi_{t,LEFM}$ is assured.

Departing from this r_λ transition value on the x-axis, the non-dimensional propagation load required for propagation increases with respect to that predicted by LEFM in both the deflection and penetration modes. To the right of the intersection CFM predicted penetration (P) and LEFM deflection (D), and at the left of the intersection CFM predicted deflection (D) and LEFM penetration (P). The zones where propagation load predicted by CFM is greater than LEFM prediction (red shaded area) is because of the competition between cohesive lengths on the substrate and interface as noted above. This effect results in a macroscopic toughening, which has significant technological importance.

It is important to note that this universal transition non dimensional load curve does not divide the (ϕ^* , r_λ)-space into penetration and deflection (like that of (r^*_{Gt} , r_λ)-space)). The zones outside of both curves are "forbidden" zones, and the possible states fall either on the LEFM line, or in the red zone (which includes the universal CFM curve).

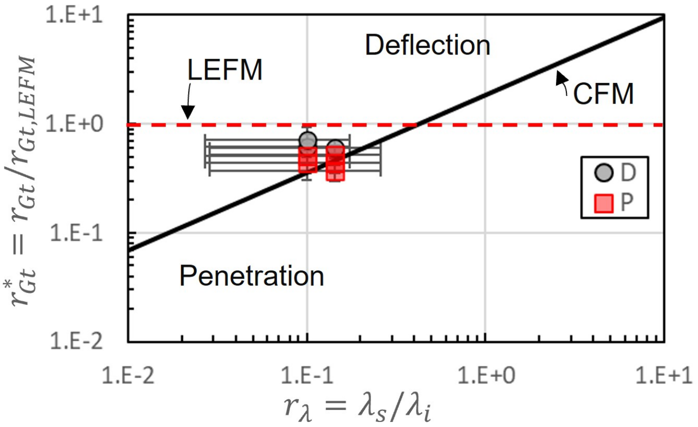

Figure 5.17: Experimental Deflection/Penetration results from Alam et al. (2017) with corresponding error bars (D stems for deflection and P for penetration), and the approximate universality curve in Toughness ratio, showing a good correlation.

To validate the universal behavior just derived, we surveyed the literature to find experimental results related to deflection/penetration behavior. It is worth noting that these types of experimental tests are not easily found in the literature, since measuring both the toughness and critical traction of both the substrate and the interface is required to incorporate the results into our universal propagation mode map. In the experimental work conducted by Alam et al. (2017), all parameters were measured for two types of interfaces in PMMA. Figure 5.17 shows these results, along with their respective error bars, overlaid with the universal propagation mode map. A strong correspondence can be observed between the experimental results and the universal behavior uncovered in this study. Additionally, it can be observed that cohesive models (universal curve) exhibit much better correspondence with the experimental results compared to what is predicted by LEFM.

It is important to mention that this study did not include results on critical propagation load, and therefore, they cannot be compared with the aforementioned universal curve.

5.5 Effect of defects on fracture deflection

The works of He and Hutchinson (1989a) and He et al. (1994) provide a very complete energy-based analysis of the conditions under which a crack will deflect when it impinges upon an interface. If the deflection mode is unfavorable, the crack penetrates the substrate. Validity of this analysis relies on the presence of kinks with length ℓ_k extending from the crack tip along the interface and/or in the substrate, as illustrated in Fig. 5.18, such that suitable LEFM fields develop about their sharp tips. Parmigiani and Thouless (2006) also performed cohesive zone model simulations of the kinked configurations, under conditions for which the assumptions of LEFM are valid. That is, the cohesive zone size is small compared to the kink length. Similarly as in the simple case of the propagation of single cracks, the small enough cohesive zones would remove the stress singularities from LEFM about the kink tips, but without affecting the energy balance that leads to the criteria of He and Hutchinson (1989a). Parmigiani and Thouless (2006) simply verified that critical stresses under such conditions matched the results from an energy-based analysis.

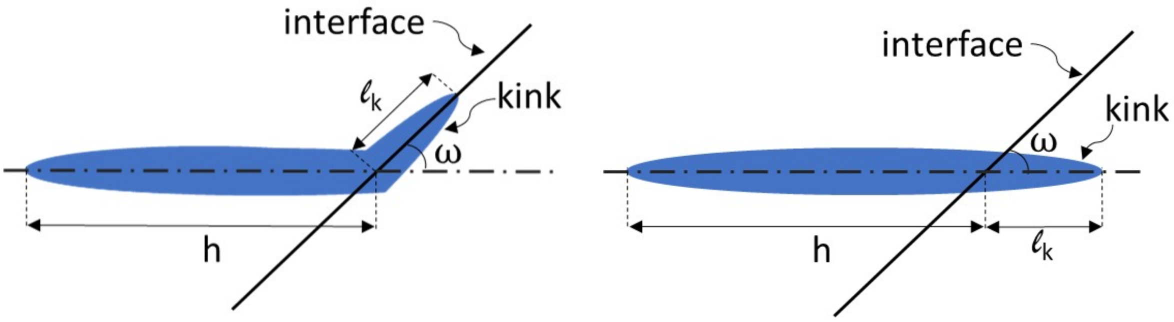

(a) Kink on the interface. (b) Kink on the substrate.

Figure 5.18: Kinked fractures simulation geometry.

In this section we perform a different analysis. The objective is to understand and quantify the effect of kinks on the deflection/penetration competition, but not necessarily restricting to conditions for LEFM to apply, as done by Parmigiani and Thouless (2006). Therefore, in our case we do not require that $\ell_k \gg \ell_{c,*}$. Part of our work amounts to bridging the gap between the LEFM and CFM extremes, whenever they differ, see red zone in the universal interaction mode map of Fig. 5.16c.

5.5.1 Model setup

The modification on the basic system described in Sec. 5.2 included a kink on either the interface or the substrate. This is the same configuration as used by Parmigiani and Thouless (2006). The case of simultaneous kinks was not explored.

The kink was introduced in the finite element mesh by incorporating decohered elements. The kink length ℓ_k was resolved with at least 6 elements in all simulations. Smaller kinks required finer meshes with a higher computational cost.

The selection of conditions of interest for the simulations was based on the universal interaction mode map. As described in section 5.4, CFM simulations had deflection/penetration transitions at higher ϕ values than predicted by LEFM even though from an energy point of view this is a metastable state. Unstable or metastable propagation occurs for a narrow range of material properties that promote intense interaction between the modes of propagation (Foulk III et al., 2008). During the competition between deflection and propagation, both cohesive zones are forming (and shielding) under increased far-field loading (Foulk III et al., 2008). The stable interaction mode predicted by LEFM is the one with the lowest propagation load. It is of interest to evaluate the effect of the presence of a kink, which may represent a pre-existing defect in the microstructure, under conditions which imply a different behaviour when considering LEFM vs. CFM. Generally speaking, it is expected that defects on the interface and in the substrate stabilize the deflection and penetration modes, respectively. This is illustrated in the simplified map of Fig 5.19a. We have replaced of the calculated data with a line that signals the transition between propagation regimes. Kinks on the interface or in the substrate would shift the line downard or upwards, respectively.

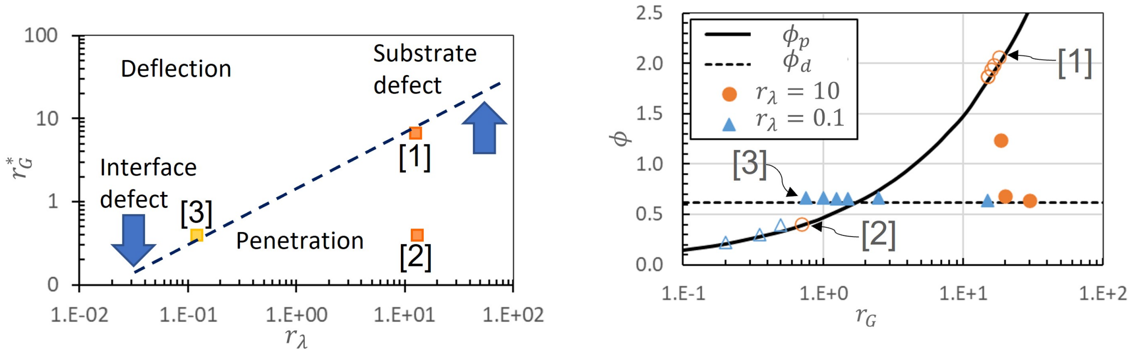

(a) Expected effect of a defect on the substrate or the interface on the universal interaction mode map (dashed line). Yellow squares indicate deflection and orange squares penetration.

(b) ϕ vs. r_G obtained in kink-free simulations.

Figure 5.19: .Configurations selected for the analysis of the effect of kinks.

Two configurations close to the domain boundary, and in the metastable region (red zone in Fig. 5.16c) are used. According to the expectation above, small kinks suitably located would suffice to change the interaction mode. Another configuration, with propagation mode according to LEFM (i.e., outside the red zone) and far removed from the domain boundary was also used. So the three cases can be summarized as

- [1] Interface kink with metastable penetration mode, close to the boundary.
- [2] Interface kink with stable penetration mode, far from the boundary.
- [3] Substrate kink in metastable deflection mode, close to the boundary.

The starting point for implementing the simulations above in this study is the kink-free simulations with interfaces at $\omega = 60°$. Fig. 5.19b shows the corresponding toughness ratio and critical load for each of the configurations above. Departing from that case, we designed new simulations with the same configuration and an initial kink either on the substrate or the interface as listed above. We performed a variation from very small kinks ($\ell_k = 1 \times 10^{-2}\, \ell_{c,*}$) to considerable sizes ($\ell_k = 1 \times 10^{2}\, \ell_{c,*}$), but always keeping the condition $\ell_k << h$ with at least two orders of magnitude.

5.5.2 Results and discussion

The non dimensional propagation load obtained for all simulations is plotted as a function of the ratios $\ell_{c,i}/\ell_k$ or $\ell_{c,s}/\ell_k$, for interface or substrate kinks, respectively, in Figs. 5.20. We found in all three cases that as ℓ_k approaches zero the interaction mode coincides with kink-free results, as expected.

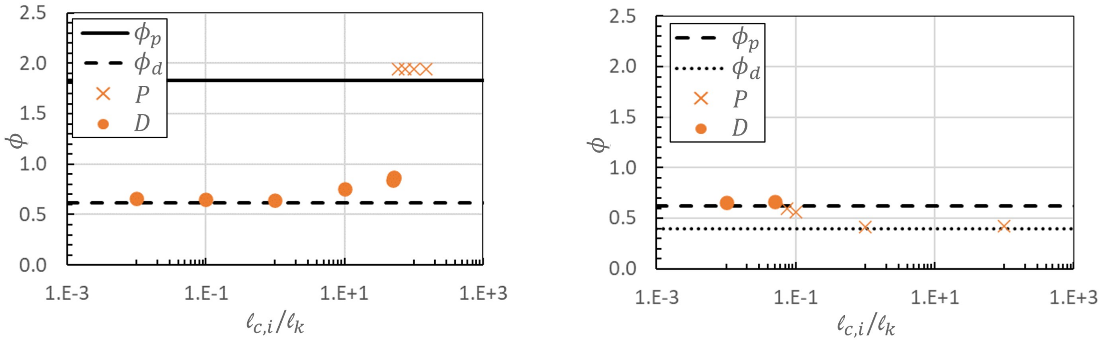

(a) Interface kink [1].

(b) Interface kink [2].

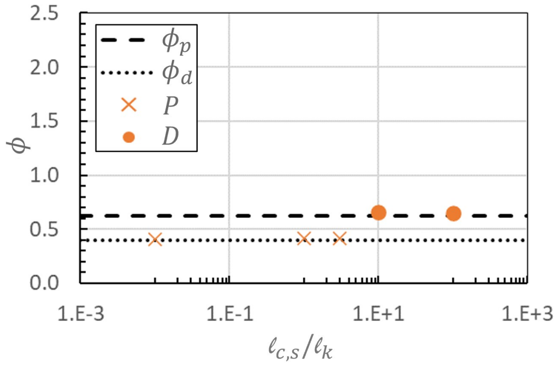

(c) Substrate kink [3].

Figure 5.20: Summary of kink simulations with interfaces at $\omega = 60°$. ϕ vs. $\ell_{c,i}/\ell_k$ plots with the effect of kink incorporation on propagation load.

In kink-free metastable interactions (cases [1] and [3]), as the kink size increased ($\ell_{c,*}/\ell_k$ decreases) a transition to stable interaction mode is found. This is to be expected, since a kink on the interface enhances deflection and a kink on the substrate enhances penetration. In both cases the transition occurred at $\ell_k \approx 0.1\ell_{c,*}$. On the other hand, in case [2], with initially stable penetration, as the kink size increased a transition to metastable deflection is found at $\ell_k \approx 17\ell_{c,i}$. The size of the kink needed to change this stable mode is two orders of magnitude larger than that necessary for the previous two cases.

To elucidate the mechanism by which a kink affects deflection/penetration, we studied the stress distribution on the substrate and the interface in the cases with and without kink, with the same remote load.

Fig. 5.21 shows the effective stresses, under a remote load of $K_I = 1.65\,\text{MPa}$, for the kink-free and kink simulation respectively. The simulation parameters correspond to case [1]: $r_\lambda = 10$, $r_G = 15$. Yellow lines show cohesive zones ($L_{c,s}$) and magenta lines show the fractured zones (ℓ_f).

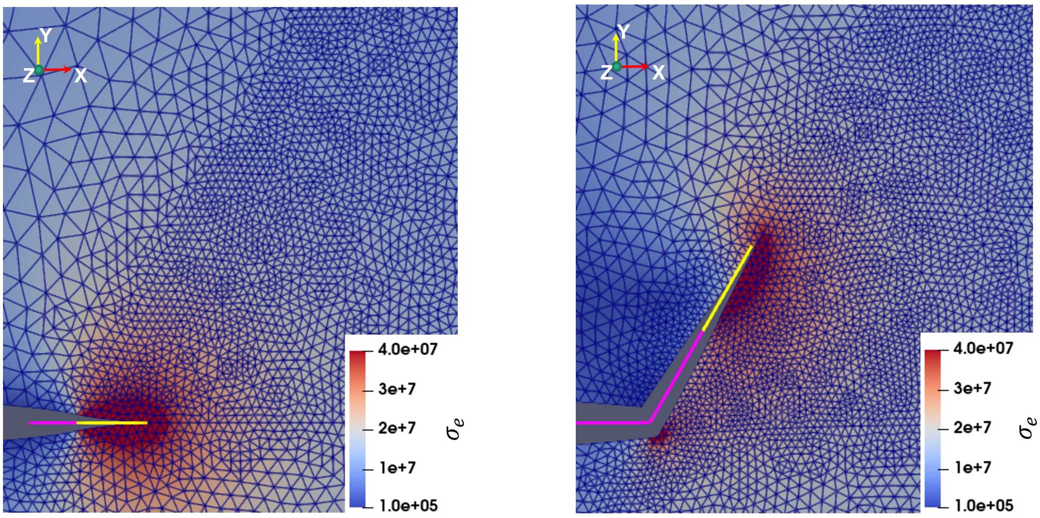

(a) Kink-free simulation. (b) Kink simulation.

Figure 5.21: Effective von Mises Stress distribution in simulations with and without kink. Both simulations have a remote load of $K_I = 1.65\,\text{MPa}$, an interface at $\omega = 60^\circ$ and $r_G = 15$. In yellow are indicated the obtained cohesive zones ($L_{c,s}$) and in magenta the fractured zones (ℓ_f).

In the kink-free simulation the stress is concentrated at the initial fracture tip, and is mostly concentrated on the substrate, while in the kink simulation these stresses are redistributed towards the kink tip, increasing the effective stress on the interface and enhancing deflection.

Fig. 5.21 shows the non dimensional cohesive traction (t) and separation (δ) normal and tangential distribution as a function of the distance r from the crack tip, for both simulations kink and kink-free. In the kink-free simulation, the cohesive zone developed on the substrate, therefore, to calculate the non-dimensional properties we divide the separation by the substrate's critical delta, $\Delta/\delta_{c,s}$, and the traction by the substrate strength, $t/\sigma_{c,s}$. On the other hand, on the kink simulation, the cohesive zone develops on the interface, therefore we divide by the interface properties: the separation by the interface's critical delta, $\Delta/\delta_{c,i}$, and the traction by the interface strength, $t/\sigma_{c,i}$. In Fig. 5.22a are the results of the kink-free case. The tangential traction and separation on the substrate are zero, as expected for a crack in mode I opening. The normal opening has its maximum in the crack tip and decreases to zero at the end of the cohesive zone.

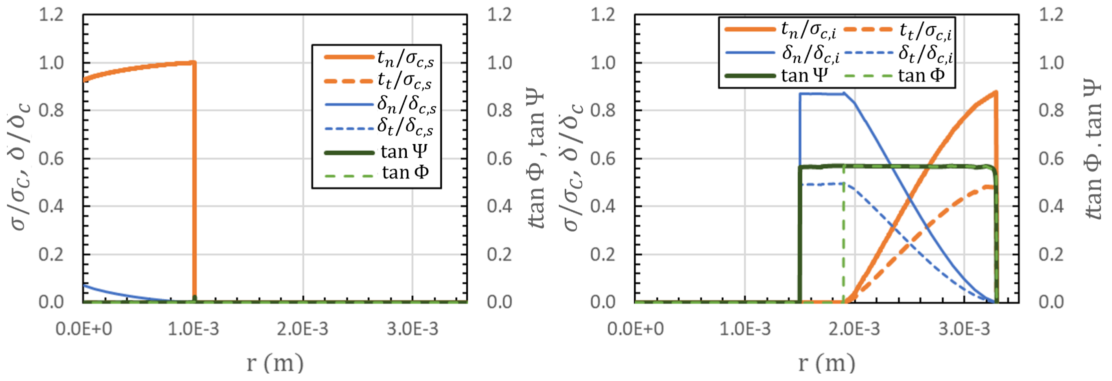

(a) Kink-free simulation.

(b) Kink simulation.

Figure 5.22: TSL parameters (traction and separation) distribution as a function of the distance from the fracture tip, r, on the substrate for the simulation kink-free and on the interface for the simulation with kink. The applied load is $K_I = 1.65\,\mathrm{MPa}$ for both figures.

Parameters on the substrate are identified with a subscript s and are marked with orange lines. Stresses on the interface are identified with a subscript i and marked with blue lines.

As expected and described above, we found that substrate defects, or kinks on the substrate, move the universality penetration/deflection curve to higher toughness ratios, enlarging the area corresponding to the penetration mode on the universal map. We also note that the displacement of the universal line is proportional to the size of the kink. For example, for the case [1], with a small displacement of the line the red point goes from being in the penetration zone to the deflection zone. In case [2], being farther away from the line, a larger displacement was necessary, and therefore, a larger defect size.

Following the same logic, interface defects, or kinks on the interface, move the universality penetration/deflection curve to lower toughness ratio ratios, enlarging the deflection area on the universal map. For example, for the case [3], with a small displacement of the line the yellow point goes from being in the penetration zone to the deflection zone.

5.6 Conclusions

In this chapter, the combined role of critical fracture energy and critical traction, and the effect of defects on fracture propagation competition in the alternative modes of interface deflection and penetration was studied.

In section 5.4, simulations were performed with interfaces at different angles with respect to the initial fracture, and the results were compared with LEFM predictions and results from related work available in the literature. The main conclusions are as follows:

- The propagation mode transition, from deflection to penetration, can occur for values of the ratio $r_G = G_{c,s}/G_{c,i}$ larger or smaller than those predicted by LEFM. This is strongly dependent on the ratio between the cohesive zone sizes $\ell_{c,s}/\ell_{c,i}$, through the stabilization of each of the modes induced by the development of the respective cohesive zones.

- The toughness of a structure under conditions where the cohesive zones develop simultaneously, and compete, is greater than that predicted by LEFM. This can occur in both propagation modes.

- The relative size of interface and substrate cohesive zones can modify the interaction mode. By increasing substrate cohesive length with respect to the interface cohesive length, deflection is inhibited. The opposite occurs when interface cohesive length is increased with respect to the substrate cohesive length.

- The results found can have direct application to any condition of competition between propagation modes, for example in hydraulic stimulation in the presence of mechanical discontinuities, and suggest that it is important to determine both toughness and strength for correct prediction.

- Traction and separation phase angles are ostensibly constant along the cohesive length. They depend essentially linearly on the interface angle, and they do not depend on the remote load.

In section 5.5 the effect of defects on the deflection/penetration transition and on the deflection/penetration universality found in section 5.4.2 was studied. Simulations were performed with interfaces and initial kinks on the substrate or interface and the effect on deflection/penetration transition was analyzed. The main conclusions are as follows:

- The presence of a kink generates a redistribution of stresses around the fracture tip which finally modifies the deflection/penetration behavior. A kink on the interface favors deflection and a kink on the substrate favors penetration.
- Even small defects, or kinks, on the substrate or interface may change the predicted deflection/penetration behavior.
- The size of the kink needed to change the propagation mode depends on the distance from the current configuration in the universal interaction mode map to the domain boundary in that map.
- Substrate defects move the universality penetration/deflection curve to higher transition toughness ratios.
- Interface defects move the universality penetration/deflection curve to lower transition toughness ratios.

Chapter 6

Speed-up algorithm for the finite element modeling of the interaction between a hydraulic fracture and a natural fracture

6.1 Introduction

In Chapter 4 we studied the controlling factors in the interaction between a hydraulic fracture and a natural fracture. This study showed that the interaction was controlled mainly by strength in both fluid lag and fluid lag-free algorithms. The main importance of these results is that by modifying, or adapting, the critical traction, a procedure typically used to accelerate cohesive fracture simulations (e.g., Alfano and Crisfield, 2001; Turon et al., 2007), as explained in Section 6.2 below, might not be used in the case of interaction between a hydraulic fracture and a discontinuity. Further analysis was needed to validate those results. In Chapter 5 we studied the combined role of critical fracture energy and critical traction on fracture propagation competence in the alternative modes of interface deflection and penetration. Although it would be necessary to complete this analysis with the incorporation of fluid and the study of the kink-out, the results suggest an alternative strategy can be used for accelerating simulations.

In this Chapter we propose an speed-up algorithm for hydraulic fracture simulations in reservoirs with discontinuities (natural fractures) and validate it with the fluid lag algorithm.

In section 6.2 we describe the critical traction adaptation, 6.3 we describe the basis of the proposed speed-up algorithm, in section 6.4 we give details of the implementation in Y-FRAC®, in section 6.5 we detail the physical and geometric properties of the case study, in section 6.6 we discuss the results of this method and we resume the conclusions in section 6.7.

6.2 Critical traction adaptation

One limitation associated with cohesive zone models is the requirement for fine meshes to ensure an adequate number of elements within the cohesive zone (Turon et al., 2007). The extent of the cohesive zone, as defined by Eq. (4.1), is directly proportional to the fracture energy release rate (G_c) and inversely proportional to the square of the cohesive strength (σ_c).

Reducing the cohesive strength results in an elongated cohesive zone and an increased number of elements encompassing it. Consequently, this approach offers a more precise representation of the softening response occurring ahead of the crack tip. However, it's noteworthy that this adjustment might induce alterations in the stress distribution within the regions proximate to the crack tip (Alfano and Crisfield, 2001; Turon et al., 2007).

Interestingly, the concept of reducing cohesive strength while maintaining constant fracture toughness was also proposed by Bažant and Planas (1997). In a separate context, this strategy is employed within Y-FRAC® to expedite simulations by enabling the utilization of coarser meshes.

The new σ_c is calculated with the following expression:

$$\sigma_c = \sqrt{\frac{1}{2\pi}\frac{E'G_c}{\ell_e}}. \tag{6.1}$$

This fictitious critical traction redefines an adaptive cohesive length, $\ell_{c,a}$ as

$$\ell_{c,a} = 0.53\frac{E'G_c}{(\sigma_c)^2} \approx 3.3\ell_e. \tag{6.2}$$

The adaptation mentioned in Eq. (6.1) is used both to model the bulk and the natural fractures. Therefore, there are two values of G_c, one associated with the bulk ($G_{c,b}$) and the other with the interface, or natural fracture ($G_{c,i}$).

To maintain consistency of the numerical model, σ_c adaptation with Eq. (6.1) should only be performed if $\ell_{c,a} > \ell_c$. In cases where $\ell_{c,a} < \ell_c$, which always happens for sufficiently fine meshes, we should not modify any bulk property and, therefore, keep the cohesive length equal to the real bulk cohesive length. Note that the factor $1/2\pi$ in Eq. (6.1), and therefore the factor 3.3 in Eq. (4.1), is arbitrary.

On the other hand, the factor 0.53 in Eq. (4.1) is not arbitrary, but has been selected after performing a large number of simulations in Y-FRAC® measuring the modeled cohesive zone, in a post-processing stage.

6.3 Speed-up algorithm description

The proposed speed-up algorithm is based on incorporating a zone of small dimensions (or Bulb) around the interface where there is a strict control over the critical traction (which correspond to the real properties of the material) while fracture energies are modified artificially in order to enlarge characteristic cohesive lengths. The idea of adapting the fracture energy inside the bulb, instead of doing it with the critical traction, is based on the results obtained in the systematic study in fluid lag regime: For the ranges of values that define the material properties in the hydraulic fracturing problem, the critical traction play a decisive role in defining the FH-IN interaction, while the fracture energies play a less relevant role. From this study it can be inferred that changes in the fracture energy with respect to the original physical value of the bulk, in a range of approximately one order of magnitude, do not induce notable changes in the mode of interaction, while more limited variations of critical traction do induce appreciable changes in said interaction. Note that the previous hypothesis is opposed to the one that arises from analyzing interactions between propagating cracks with pre-existing interfaces in a solid medium from the point of view of LEFM, refer for example to the works, Hutchinson et al. (1987); Hutchinson and Suo (1991). However, the hypothesis proposed in this work has been supported by other bibliographical sources, see in particular the contributions of Parmigiani and Thouless (2006) and Leguillon (2002) for materials with non-zero cohesive lengths.

6.4 Implementation

A finite element mesh of uniform size, ℓ_e, is assumed in the vicinity of the IN, both in the discretization of the IN and the bulk. The following implementation is only done if $\ell_e > \ell_c/3.3$. Three concentric bulbs, or geometric regions, are defined surrounding the IN, as schematized in Fig. 6.1.

Each of them has a half-thickness of one ℓ_e, and they are identified with the subscript 'n', $n = 1; 2; 3$, inside out. At the interfaces of the FE contained in each bulb, a fictitious cohesive material is defined whose properties are: the fracture energy $G_{c,n}$, the critical traction $\sigma_{c,n}$ and a characteristic cohesive length $\ell_{c,n}$. The three parameters of each region are related through Eq. (4.1), so only two of them can be selected through some rule, the rest is linked by said equation.

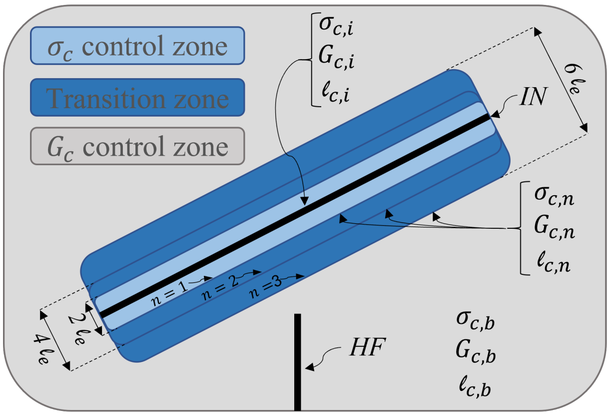

Figure 6.1: Scheme of Stepped Bulb: 3 layers of materials are defined within the Bulb, with fracture energies ($G_{c,1}$, $G_{c,2}$, $G_{c,3}$), critical tractions ($\sigma_{c,1}$, $\sigma_{c,2}$, $\sigma_{c,3}$) and cohesive lengths ($\ell_{c,1}$, $\ell_{c,2}$, $\ell_{c,3}$). Outside the bulb, the properties are: $G_{c,b}$, $\ell_{c,b}$ and the adapted critical traction $\sigma_{c,b}$ from the bulk.

Bulb properties are defined as follows:

1) Bulb cohesive lengths ares maintained equal, and and with a length of 3.3 finite elements: $\ell_{c,1} = \ell_{c,2} = \ell_{c,3} = 3.3\ell_e$.

2) For the inner Bulb region, interface and bulk critical traction maintain the real property value. It means $\sigma_{c,1}$ remain equal to bulk critical traction, $\sigma_{c,b}$ and for the IN, it remains equal to the interface critical traction, $\sigma_{c,i}$.

3) For the inner Bulb region, given $\sigma_{c,1}$ and $\ell_{c,1}$ and through Eq. (4.1), the adaptive $G_{c,1}$ is determined. This value is only used if $G_{c,n} > G_{c,b}$. If it is not, $G_{c,1} = G_{c,b}$ is adopted. The same calculation applies to the interface elements belonging to the

IN. Fracture energies for the three steps are calculated according to the following rule:

$$G_{c,n} = \alpha_n (G_{c,1} - G_{c,b}) + G_{c,b} \tag{6.3}$$

with $\alpha_n = 1.0,\ 0.8,\ 0.2$.

4) With the parameters $G_{c,2}$ and $G_{c,3}$ and again, with Eq. (4.1), critical traction $\sigma_{c,2}$ and $\sigma_{c,3}$ are calculated.

We subdivided the physical/numerical data set from which the reported simulations were performed into three cases, summarized below.

- Cases 0 to 3: variants in interaction angle and the state of maximum and minimum crustal stresses, in order to represent different regimes in the parametric space of dimensionless variables defined in Chapter 3.
- Cases A, B, C and D: Variants regarding the value assigned to the coefficient β that regulates the relationship between critical tensile and shear stresses in the reservoir materials (bulk and natural interfaces).
- Types I, II and III: variants regarding the type of numerical approximation used to perform the FH-IN interaction simulations, see the conceptual scheme in Fig. 6.2.

  I) Type I is a model with refined finite element mesh ($\ell_e < \ell_c/3.3$) over the entire propagation domain of HF and IN. It does not require parameter adaptation. Therefore, there is a strict control regarding the critical traction and fracture energies of the materials that constitute the reservoir, which correspond to the real physical properties that are to be modeled (see point indicated in red color in Fig. 6.2). The finite element size of this approximation guarantees a correct modeling of the cohesive length in both materials (bulk and natural interface). The computational cost of this alternative is elevated because of the fine mesh required.

  II) Type II model is similar to Type I, but the mesh refinement ($\ell_e < \ell_c/3.3$) is only satisfied in the region neighboring the IN. In the remaining part of the bulk, coarse mesh is used, and therefore, critical traction adaptation is applied.

III) Type III is a finite element model with a coarse mesh over the entire domain. For this approximation to be coherent, it is necessary to adapt the cohesive length of the material throughout the bulk, either by redefining the critical traction (decrease) or the fracture energies (increase). There are two variants of this Type III model:

- Adaptive critical traction, Act, (Without Bulb): It is the model already available in Y-FRAC® with automatic critical traction adaptation, keeping the fracture energies fixed and equal to those of the physical model (the point indicated in green in Figure 6.2 represents the set of fictitious parameters from this approximation).
- Adaptive fracture energies, AGc, (With Bulb): It is the model proposed in this work to capture the FH-IN interaction (the point indicated in blue in Fig. 6.2 represents the set of fictitious parameters from this approximation).

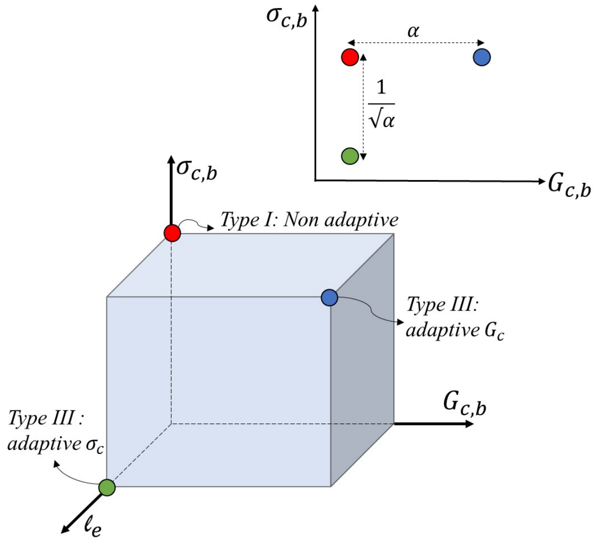

Figure 6.2: Set of physical (in red) and fictitious parameters that adopt the type III approximations: without bulb and adaptive critical traction, Act (in green), and with bulb and adaptive fracture energy, AGc (in blue). The fitted value of the fictitious parameters depends on the mesh size of FE, which is measured as a value relative to the physical cohesive length ℓ_e: $\alpha = (3.3\ell_e)/\ell_c$.

6.5 Physical and geometric properties of the problems

Nine sets of parameters have been simulated to represent different points in the parametric diagram described by Garagash (2006a) and explained in detail in Chapter 3 (crustal stresses govern the parameter $\mathcal{T}$ and fracture energies govern the parameter $\mathcal{K}$). Also different HF-IN interaction angles and bulk critical traction where studied. The parameter $\mathcal{T}$ is calculated a posteriori in all cases, with the pressure p_0, taken as the average value of the hydraulic pressure, and the time t, at the instant of intersection of the HF and IN.

Table 6.2 summarizes the main parameters that identify these nine simulations. The geometry of the problem (described in Fig. 6.3), and the parameters Q, μ, E, and ν are common to all four cases and its values are summarized in Table 6.1.

Table 6.1: Fluid and Bulk parameters used on the four cases simulations

Q $[m^3/s]$	μ [Pa.s]	E [GPa]	ν
0.096	0.0013	20	0.47

On this study we include variations of the mode weighting factor β to analyze it's effect. β is an important parameter for HF-NF interaction since interfaces can fail due to shear stresses, we studied the following values $\beta = 10.0, 5.0, 12.0, 11.5$, which correspond to letters A to D respectively in Table 6.2 .

6.6 Results

The main variable that was analyzed is the mode of HF-IN interaction. In general, for the simulated cases A, C and D, the interaction mode captured corresponds to the deviation of the HF with offset on the IN, without actually opening the full IN length. For this reason, the variable reported in detail is the offset length in all cases. On the contrary, B Cases, characterized by low β, tend to capture only crossing or opening modes and/or full-length

Table 6.2: Main parameters of the evaluated cases

Case	σ_h [MPa]	σ_H [MPa]	$G_{c,b}$ [N/m]	$\sigma_{c,b}$ [MPa]	ω [deg]	β
0 A	0	2.0	80	7.5	75	10.0
0 B	0	2.0	80	7.5	75	05.0
1 A	2	2.5	80	7.5	75	10.0
1 B	2	2.5	80	7.5	75	05.0
1 C	2	5.0	80	7.5	45	12.0
1 D	2	5.0	80	7.5	45	11.5
2 A	1	1.5	40	5.3	75	10.0
2 B	1	1.5	40	5.3	75	05.0
3 A	0	1.0	100	6.5	60	10.0

IN slip. Thus, the length ℓ_{offset} tends to take extreme values. This behavior should be exacerbated by even smaller values of β. Another important parameter reported here is the CPU time required for each simulation. This time depends on factors that make its evaluation more uncertain, since it loses meaning to take as a unit of measurement the CPU time consumed by each iteration, or the time step of the algorithm. Furthermore, for a certain stage of the simulation, the CPU time also depends very strongly of the mesh size in the area of the tip of the hydraulic domain, which in many cases reported here has not been considered as a relevant variable to be evaluated. To mitigate this effect, the criterion adopted for measuring the time is considering it from the start of the simulation to the moment the fracture deviates, or crosses the IN. Despite the uncertainty in the assessment of CPU time, with the reported results it is possible to obtain a fairly accurate idea of the order of the speed-up reached in a simulation by increasing the mesh size in the IN area.

From the analysis carried out regarding the CPU time required by the different simulations, it can be observed as a general characteristic that there is a significant decrease in the CPU requirement in Type III Models compared to Type II. This effect is due to

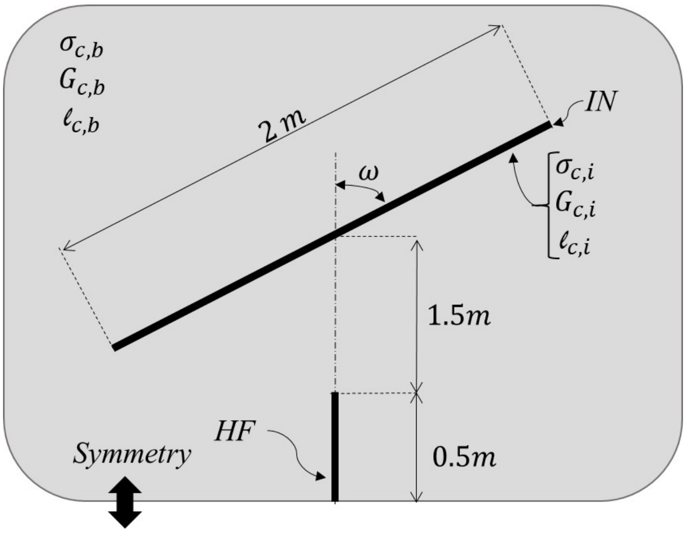

Figure 6.3: Geometric scheme of the simulations carried out to verify the speed-up algorithm.

the differences in the size of the mesh used in each Type of approximation.

Type I simulations (fine mesh with full real properties) were not considered in this analysis due to their high computational cost and associated CPU time. On the other hand, it was considered that Type II simulations are the benchmark since they use critical traction adaptation only in the hydraulic fracture propagation zone, and in the vicinity of the interface no properties adaptation is carried out, thus being able to capture the true interaction mode for the problem parameters.

In Fig. 6.4 are the ℓ_{offset} / ℓ_{IN} and CPU time vs $\ell_{e,IN}$ (finite element size on the interface) results obtained for simulations cases 0 to 3 and for the three types simulated: Type II Non adaptive (NA), Type III Adaptive critical Stress (Act) and Adaptive fracture energy (AGc). As expected, CPU time, symbolized with Filled symbols, decreased with an increasing ℓ_e for all the analyzed cases. Coarse meshes have fewer degrees of freedom and therefore a lower computational cost.

Going to the offset length results, in case 0A both fracture energy adaptive and non-adaptive simulations resulted in offset, with some scatter on ℓ_{offset} (see Fig. 6.4a). On the contrary, the critical traction adaptive simulations resulted in crossing ($\ell_{offset} = 0$). This evidences a change in the mode of interaction by using critical traction adaptation that does not occur in AGc simulations. Similar results were obtained for cases 1A, 1C, 2A and 3A as shown in Fig. 6.4a.

In Cases 0B and 1B the NA simulation resulted in opening ($\ell_{offset} = \ell_{IN}$) and the AGc simulations resulted in similar offset lengths, $\ell_{offset} \approx \ell_{IN}$, while Act simulations

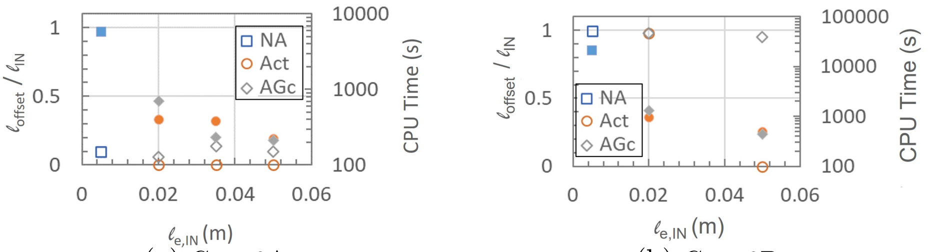

(a) Case 0A. (b) Case 0B.

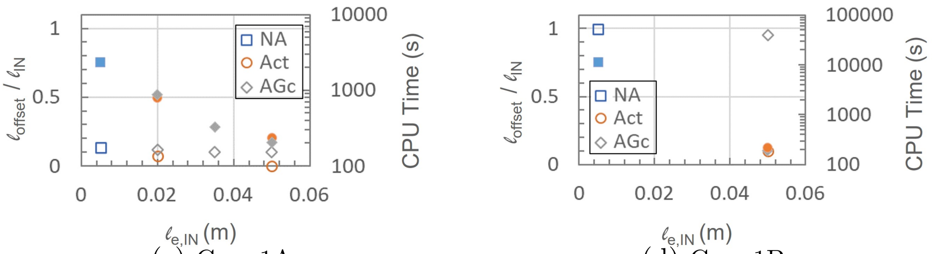

(c) Case 1A. (d) Case 1B.

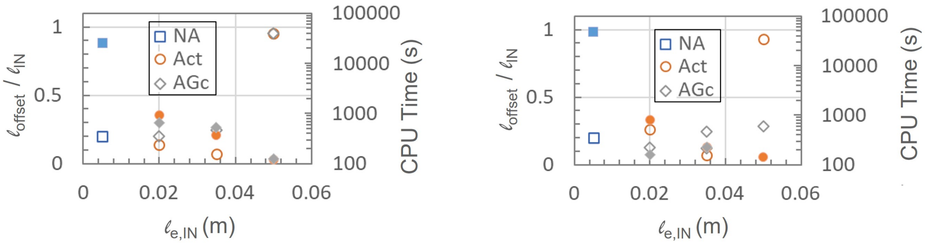

(e) Case 1C. (f) Case 1D.

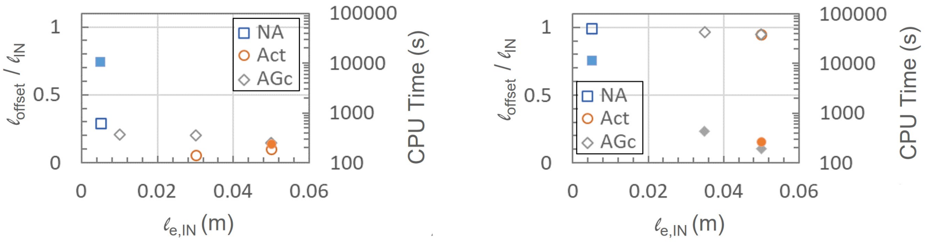

(g) Case 2A. (h) Case 2B.

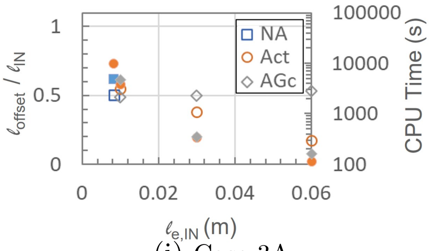

(i) Case 3A.

Figure 6.4: ℓ_{offset}/ℓ_{IN} and CPU time vs. ℓ_e/ℓ_{IN} results obtained for NA, Act, and AGc simulations.

resulted in crossing or small offsets. This results, again evidences a change in the mode of interaction by using critical traction adaptation.

Finally we can conclude that critical traction adaptation, within the range of parameters analyzed, does not maintain the real interaction type, in this case represented by Type II simulations (without properties adaptation around the interface). Secondly, fracture energy adaptation mostly maintained the interaction expected for the problem physical properties. In this way we can say that critical energies adaptation fulfills the objective of speed up the simulations (due to an increase in the finite element size) maintaining the results obtained with fine meshes and no properties adaptation.

6.7 Conclusions

1) A novel speed up algorithm for hydraulic fractures with interfaces based on fracture energy adaption was proposed and validated on fluid-lag regime in Y-FRAC®.

2) The validations included a wide range of parameters, with variations in crustal stresses (σ_h, σ_H), and physical parameters ($G_{c,b}$, $\sigma_{c,b}$, ω, β).

3) The results shown that simulations with critical traction adaptation, here represented as Act, allows to increase the mesh size but does not maintain the real interaction type, represented by non adaptive simulations (NA).

4) Fracture energy adaptation mostly maintained the interaction expected for the problem physical properties and allows to increase the mesh size. This validates the proposed speed-up algorithm.

Chapter 7

Conclusions

Many unconventional reservoirs are naturally fractured, and understanding the interactions between hydraulic fracture and natural fractures is crucial in estimating fracture complexity, drained reservoir volume and well stimulation efficiency. In this study, a fully coupled numerical model was developed to model hydraulic fracture process in naturally fractured reservoirs, where fracture turning, kinking, branching and coalescence can be captured.

In this dissertation, we focused on the modeling of hydraulic fracture stimulation in reservoirs with natural fractures. The incorporation of natural fractures that can deform and interact with the stimulated network of fractures presents challenges due to the increased degrees of freedom in the system. To address these challenges, we utilized Y-FRAC®, a numerical hydraulic fracturing simulator designed for parallel computing.

In Chapter 2, we conducted a comprehensive analysis of the evolution of fundamental variables throughout the life of a hydraulic fracture, encompassing various propagation regimes. This analysis provided valuable insights into accurately setting up simulation parameters. Building upon the previous work by Garagash (2006b) on approximate universal behavior, we extended the understanding of these behaviors and established quantitative time bounds for the applicability of each propagation regime.

Our study focused on the analysis of a two-dimensional hydraulic fracture propagating in an elastic medium, taking into account the fluid lag. We identified three distinct regimes: early, transient, and late time, which corresponded to different regions within the MKO triangle.

An important finding of our research was the identification of transition values, denoted as $\mathcal{T}_{ei}(\mathcal{K})$ and $\mathcal{T}_{il}(\mathcal{K})$, which determined the shifts between the early, transient, and late time regimes. These transition values provided a clearer understanding of the crack behavior across the entire range of non-dimensional toughness $\mathcal{K}$.

Furthermore, we discovered an approximate single curve, referred to as $\mathcal{C}$, that effectively captured the evolution of essential variables $\mathcal{F}_0$ across the MKO triangle, encompassing the cases of the OK and MK edges. We concluded that, for a significant portion of the MKO triangle (specifically, when $\mathcal{K} \gtrsim 0.3$), the values of $\mathcal{F}_0$ clustered closely around the $\mathcal{C}$ curve.

To facilitate practical applications, we developed a graphical representation method that could be utilized not only for hydraulic fracturing but also for other physical phenomena. This representation allowed for quick estimations and served as a reliable test for algorithms that neglected the fluid lag, particularly in the intermediate regime where $\xi_f < 1$ became significant. By comparing computed values within the expected bundle around the universal curve, projected onto the reduced space $\tilde{\mathcal{F}}_0 = \{\Omega_0, \Pi_0, \gamma\}$, the method's reliability could be assessed.

The practical implications of our conclusions are extensive. They contribute to the accurate determination of initial conditions for more refined hydraulic fracture propagation calculations, such as finite element simulations. Additionally, our findings provide valuable guidelines for making quick estimations in field applications where precise measurements of crack geometry may be unavailable or subject to significant uncertainties, as long as deviations from the observed universal behavior remain within approximately 20

Lastly, it is important to note that the disparities between the 2D and 3D cases indicate potential opportunities for extending our findings to three-dimensional scenarios. Further investigation into this realm is warranted and holds promise for future research endeavors.

Chapter 3 presented a systematic study aimed at identifying the controlling factors in the interaction between a hydraulic fracture and a natural fracture. Our analysis revealed significant insights into the behavior of these interactions in different regimes.

One key finding was that, in the fluid lag regime, the interaction mode between the hydraulic fracture and the natural fracture was primarily determined by the critical traction, regardless of the fracture energy involved. This indicates that the critical traction plays a crucial role in dictating the behavior of the interaction, and fracture energy has less influence in this regime.

Similarly, in the fluid lag-free regime, a string control by the critical traction was found. In addition, we observed some variability in the interaction mode and offset length depending on the mesh type and time increment used in the simulation. This suggests that the mesh type and time increment can affect the interaction between the hydraulic fracture and the natural fracture in this regime. Therefore, it is important to consider these factors and select appropriate settings to accurately capture the behavior of the interaction.

The findings from this study emphasize the importance of having benchmark solutions under simplifying conditions. These benchmark solutions can serve as reference points for validating numerical models and providing insights into the behavior of hydraulic fractures interacting with natural fractures. By comparing simulation results with benchmark solutions, researchers can assess the accuracy and reliability of their models and gain a better understanding of the complex interactions involved.

Overall, the results of this study contribute to our understanding of the controlling factors in the interaction between hydraulic fractures and natural fractures. They highlight the significance of the critical traction in the fluid lag regime and the influence of mesh type and time increment in the fluid lag-free regime. These findings provide valuable insights for further research and development of numerical models, and they underscore the need for continued investigation and refinement of techniques to accurately simulate and predict hydraulic fracture behavior in the presence of natural fractures.

In Chapter 4, the primary focus was on finding benchmark solutions for the interaction between a propagating hydraulic fracture and a natural fracture. Although analytic solutions were not available, extensive numerical studies were conducted to enhance the understanding of this complex phenomenon, specifically examining the simplest case of the deflection of the hydraulic fracture into the natural fracture (kink-in) during dry crack propagation.

On the fist part of this chapter, simulations of fracture propagation were performed with interfaces at various angles relative to the initial fracture, and the results were compared with predictions from LEFM and existing literature. The possible interaction types were categorized as deflection (propagation along the interface) and penetration (crossing across the interface). Through these investigations, several important conclusions were drawn:

We found that the transition from the deflection to the penetration propagation mode can occur at different values of the substrate-to-interface toughness ratio ($r_G = G_{c,s}/G_{c,i}$) compared to those predicted by LEFM. This transition is strongly dependent on the ratio between cohesive zone sizes ($\ell_{c,s}/\ell_{c,i}$), as it influences the stabilization of each mode through the development of their respective cohesive zones.

It was also found that the toughness of a structure, when cohesive zones develop simultaneously and compete, is greater than that predicted by LEFM. This phenomenon can occur in both propagation modes, highlighting the significance of cohesive zone interactions in determining fracture behavior.

From the results of these simulations, it can also be concluded that the relative sizes of the interface and substrate cohesive zones play a crucial role in modifying the interaction mode. Increasing the substrate cohesive length relative to the interface cohesive length inhibits deflection, while increasing the interface cohesive length relative to the substrate cohesive length promotes deflection.

The findings from this chapter have direct implications for situations involving competition between propagation modes, such as hydraulic stimulation in the presence of mechanical discontinuities. They suggest that accurate prediction requires considering both the toughness and strength of the materials involved.

Additionally, on the second part of Chapter 4, we conducted simulations including defects, or kinks, on the substrate or interface to analyze their effects on the deflection/penetration transition. From this investigation, several conclusions were drawn. Firstly, even small defects or kinks on the substrate or interface can significantly influence the predicted deflection/penetration behavior. Furthermore, our analysis revealed that substrate defects shift the universality curve of deflection/penetration to higher transition toughness ratios, while interface defects shift it to lower transition toughness ratios. These findings provide valuable insights into the interaction between hydraulic fractures and natural fractures, contributing to a better understanding of the factors that govern their behavior. Importantly, this knowledge has practical implications for fracture design and optimization in various engineering applications.

Moving on to Chapter 5, we proposed a new speed-up algorithm that utilizes fracture energy adaptation. This algorithm was tested in hydraulic fracture simulations with natural fractures, and its efficacy was evaluated. The algorithm demonstrated promising results in improving the computational efficiency of the simulations while maintaining accuracy.

We validated the algorithm's effectiveness in simulating the fluid-lag regime in Y-FRAC®. The validations encompassed a wide range of parameters, including variations in crustal stresses (σ_h, σ_H) and physical parameters ($G_{c,b}$, $\sigma_{c,b}$, ω, β).

The results of the validations revealed that simulations employing critical traction adaptation (Act) allowed for an increase in mesh size but did not accurately capture the real interaction type, as represented by non-adaptive simulations (NA). However, fracture energy adaptation demonstrated a better ability to maintain the expected interaction based on the problem's physical properties while still allowing for an increase in the mesh size. This successful validation supports the proposed speed-up algorithm.

Together, these chapters contribute to a comprehensive understanding of the interaction between hydraulic fractures and natural fractures, providing insights into important factors that govern their behavior. Moreover, the introduction of the speed-up algorithm in Chapter 5 presents practical implications for fracture design and optimization in various engineering applications, offering improved computational efficiency without sacrificing accuracy.

Finally, In the Appendix, We conducted an in-depth examination of straight propagation by exploring structured and unstructured meshes, we gained valuable insights into their respective effects on fracture behavior and propagation. This investigation helped us better understand the role of mesh types in the simulation models. We also studied mixed-mode loading with free propagation paths. Through the study of this complex loading scenario, we aimed to enhance our understanding of the intricate interplay between fracture modes and mesh characteristics. By thoroughly investigating these different aspects, we have contributed valuable insights into the behavior and performance of the simulation models employed in this dissertation. These findings deepen our understanding of fracture mechanics and provide a basis for further research and development in this field.

Overall, this dissertation provides valuable insights into the modeling of hydraulic fracture stimulation in reservoirs with natural fractures. The findings contribute to a better understanding of fracture propagation regimes, the interaction between hydraulic fractures and natural fractures, and the development of novel algorithms to enhance computational efficiency. The research conducted in this study lays the foundation for further advancements in hydraulic fracturing simulation and optimization techniques, ultimately leading to improved reservoir characterization and production optimization strategies in unconventional reservoirs.

Capítulo 8

Conclusiones

En yacimientos no convencionales, la presencia de fracturas naturales es común, y comprender las interacciones entre fracturas hidráulicas y naturales es crucial para estimar la complejidad de la fractura, el volumen drenado del yacimiento y la eficiencia de la estimulación del pozo. En este estudio, se desarrolló un modelo numérico completamente acoplado para simular el proceso de fracturación hidráulica en yacimientos naturalmente fracturados, capturando fenómenos como ramificaciones y coalescencias de fracturas.

En esta tesis, nos centramos en modelar la estimulación de fracturas hidráulicas en yacimientos con fracturas naturales. La incorporación de fracturas naturales que pueden deformarse e interactuar con la red estimulada de fracturas presenta desafíos debido al aumento de los grados de libertad en el sistema. Para abordar estos desafíos, utilizamos Y-FRAC®, un simulador numérico de fracturación hidráulica diseñado para cómputo paralelo.

En el Capítulo 3, realizamos un análisis exhaustivo de la evolución de variables fundamentales a lo largo de la vida de una fractura hidráulica, abarcando diversos regímenes de propagación. Este análisis proporcionó valiosas perspectivas para establecer parámetros de simulación con precisión. Ampliamos la comprensión de comportamientos universales aproximados anteriores y establecimos límites temporales cuantitativos para la aplicabilidad de cada régimen de propagación, construyendo sobre el trabajo previo de Garagash (2006b).

Nuestro estudio se centró en el análisis de una fractura hidráulica bidimensional que se propaga en un medio elástico, teniendo en cuenta el retraso del fluido. Identificamos tres regímenes distintos: temprano, transitorio y tardío, que corresponden a diferentes regiones dentro del triángulo MKO.

Un hallazgo importante fue la identificación de valores de transición, denotados como $\mathcal{T}_{ei}(\mathcal{K})$ y $\mathcal{T}_{il}(\mathcal{K})$, que determinaron los cambios entre los regímenes temprano, transitorio y tardío. Estos valores de transición proporcionaron una comprensión más clara del comportamiento de la fractura en todo el rango de tenacidad no dimensional $\mathcal{K}$.

Además, descubrimos una curva aproximada única, denominada $\mathcal{C}$, que capturó eficazmente la evolución de variables esenciales $\mathcal{F}_0$ en el triángulo MKO, abarcando los casos de los bordes OK y MK. Concluimos que, para una parte significativa del triángulo MKO (específicamente, cuando $\mathcal{K} \gtrsim 0.3$), los valores de $\mathcal{F}_0$ se agruparon estrechamente alrededor de la curva $\mathcal{C}$.

Para facilitar aplicaciones prácticas, desarrollamos un método de representación gráfica que podría utilizarse no solo para fracturación hidráulica sino también para otros fenómenos físicos. Esta representación permitió estimaciones rápidas y sirvió como una prueba confiable para algoritmos que ignoran el retraso del fluido, especialmente en el régimen intermedio donde $\xi_f < 1$ se volvía significativo. Al comparar los valores calculados dentro del conjunto esperado alrededor de la curva universal, proyectado en el espacio reducido $\tilde{\mathcal{F}}_0 = \{\Omega_0, \Pi_0, \gamma\}$, se podía evaluar la confiabilidad del método.

Las implicaciones prácticas de nuestras conclusiones son extensas. Contribuyen a la determinación precisa de condiciones iniciales para cálculos de propagación de fracturas hidráulicas más refinados, como simulaciones de elementos finitos. Además, nuestras conclusiones proporcionan pautas valiosas para hacer estimaciones rápidas en aplicaciones de campo donde las medidas precisas de la geometría de la grieta pueden no estar disponibles o estar sujetas a incertidumbres significativas, siempre y cuando las desviaciones del comportamiento universal observado permanezcan dentro de aproximadamente el 20

Es importante destacar que las disparidades entre los casos 2D y 3D indican oportunidades potenciales para extender nuestros hallazgos a escenarios tridimensionales. Se justifica una investigación adicional en este ámbito y promete futuros esfuerzos de investigación.

En el Capítulo 4, presentamos un estudio sistemático destinado a identificar los factores de control en la interacción entre una fractura hidráulica y una fractura natural. Nuestro análisis reveló perspicacias significativas sobre el comportamiento de estas interacciones en diferentes regímenes.

Un hallazgo clave fue que, en el régimen con retraso del fluido, el modo de interacción entre la fractura hidráulica y la fractura natural estaba determinado principalmente por la tracción crítica, independientemente de la energía de fractura involucrada. Esto indica que la tracción crítica desempeña un papel crucial en dictar el comportamiento de la interacción, y la energía de fractura tiene menos influencia en este régimen.

De manera similar, en el régimen sin retraso del fluido, se encontró un control por la tracción crítica. Además, observamos alguna variabilidad en el modo de interacción y la longitud de desplazamiento según el tipo de malla y el incremento de tiempo utilizado en la simulación. Esto sugiere que el tipo de malla y el incremento de tiempo pueden afectar la interacción entre la fractura hidráulica y la fractura natural en este régimen. Por lo tanto, es importante considerar estos factores y seleccionar configuraciones apropiadas para capturar con precisión el comportamiento de la interacción.

Los hallazgos de este estudio enfatizan la importancia de tener soluciones de referencia bajo condiciones simplificadas. Estas soluciones de referencia pueden servir como puntos de referencia para validar modelos numéricos y proporcionar perspicacias sobre el comportamiento de las fracturas hidráulicas que interactúan con fracturas naturales. Al comparar resultados de simulaciones con soluciones de referencia, los investigadores pueden evaluar la precisión y confiabilidad de sus modelos y obtener una mejor comprensión de las complejas interacciones involucradas.

En el Capítulo 5, el enfoque principal se centró en encontrar soluciones de referencia para la interacción entre una fractura hidráulica en propagación y una fractura natural. Aunque no se contaba con soluciones analíticas, se realizaron extensos estudios numéricos para mejorar la comprensión de este fenómeno complejo, examinando específicamente el caso más simple de la desviación de la fractura hidráulica en la fractura natural (kink-in) durante la propagación de la fractura en condiciones secas.

En la primera parte de este capítulo, se realizaron simulaciones de propagación de fracturas con interfaces en varios ángulos en relación con la fractura inicial, y los resultados se compararon con predicciones de LEFM y la literatura existente. Los tipos de interacción posibles se categorizaron como deflexión (propagación a lo largo de la interfaz) y penetración (cruzando la interfaz). A través de estas investigaciones, se llegaron a varias conclusiones importantes:

Descubrimos que la transición del modo de propagación de la deflexión a la penetración puede ocurrir en diferentes valores de la relación de tenacidad de sustrato a interfaz ($r_G = G_{c,s}/G_{c,i}$) en comparación con los predichos por LEFM. Esta transición depende en gran medida de la relación entre los tamaños de la zona cohesiva ($\ell_{c,s}/\ell_{c,i}$), ya que influye en la estabilización de cada modo a través del desarrollo de sus respectivas zonas cohesivas.

También se encontró que la tenacidad de una estructura, cuando las zonas cohesivas se desarrollan simultáneamente y compiten, es mayor que la predicha por LEFM. Este fenómeno puede ocurrir en ambos modos de propagación, destacando la importancia de las interacciones de zonas cohesivas en la determinación del comportamiento de la fractura.

A partir de los resultados de estas simulaciones, también se puede concluir que los tamaños relativos de las zonas cohesivas de la interfaz y el sustrato desempeñan un papel crucial en la modificación del modo de interacción. Aumentar la longitud cohesiva del sustrato en relación con la longitud cohesiva de la interfaz inhibe la deflexión, mientras que aumentar la longitud cohesiva de la interfaz en relación con la longitud cohesiva del sustrato promueve la deflexión.

Los hallazgos de este capítulo tienen implicaciones directas para situaciones que involucran competencia entre modos de propagación, como la estimulación hidráulica en presencia de discontinuidades mecánicas. Sugieren que una predicción precisa requiere considerar tanto la tenacidad como la resistencia de los materiales involucrados.

Además, en la segunda parte del Capítulo 5, realizamos simulaciones que incluyeron defectos, tanto en el sustrato como la interfaz, para analizar sus efectos en la transición de deflexión/penetración. De esta investigación, se extrajeron varias conclusiones. En primer lugar, incluso pequeños defectos en el sustrato o interfaz pueden influir significativamente en el comportamiento predicho de deflexión/penetración. Además, nuestro análisis reveló que los defectos en el sustrato desplazan la curva de universalidad de deflexión/penetración a relaciones de tenacidad de transición más altas, mientras que los defectos en la interfaz la desplazan a relaciones de tenacidad de transición más bajas. Estos hallazgos ofrecen perspicacias valiosas sobre la interacción entre fracturas hidráulicas y naturales, contribuyendo a una mejor comprensión de los factores que rigen su comportamiento. Importante destacar, este conocimiento tiene implicaciones prácticas para el diseño y la optimización de fracturas en diversas aplicaciones de ingeniería.

Pasando al Capítulo 6, propusimos un nuevo algoritmo de aceleración que utiliza la adaptación de la energía de fractura. Este algoritmo se probó en simulaciones de fracturamiento hidráulico con fracturas naturales, y se evaluó su eficacia. El algoritmo demostró resultados prometedores al mejorar la eficiencia computacional de las simulaciones sin sacrificar la precisión.

Validamos la eficacia del algoritmo al simular el régimen de retraso del fluido en Y-FRAC®. Las validaciones abarcaron una amplia gama de parámetros, incluyendo variaciones en las tensiones crustales (σ_h, σ_H) y parámetros físicos ($G_{c,b}$, $\sigma_{c,b}$, ω, β).

Los resultados de las validaciones revelaron que las simulaciones que emplearon la adaptación de la tracción crítica (Act) permitieron un aumento en el tamaño de la malla pero no capturaron con precisión el tipo real de interacción, como lo representan las simulaciones no adaptativas (NA). Sin embargo, la adaptación de la energía de fractura demostró una mejor capacidad para mantener la interacción esperada según las propiedades físicas del problema, al tiempo que permitía un aumento en el tamaño de la malla. Esta validación exitosa respalda el algoritmo propuesto de aceleración.

Juntos, estos capítulos contribuyen a una comprensión integral de la interacción entre fracturas hidráulicas y fracturas naturales, proporcionando perspectivas sobre factores importantes que rigen su comportamiento. Además, la introducción del algoritmo de aceleración en el Capítulo 6, presenta implicaciones prácticas para el diseño y la optimización de fracturas en diversas aplicaciones de ingeniería, ofreciendo una mayor eficiencia computacional sin sacrificar la precisión.

Finalmente, en el Apéndice, llevamos a cabo un examen detenido de la propagación recta explorando mallas estructuradas y no estructuradas, obteniendo información valiosa sobre sus efectos respectivos en el comportamiento y la propagación de las fracturas. Esta investigación nos ayudó a comprender mejor el papel de los tipos de malla en los modelos de simulación. También estudiamos la carga en modo mixto con rutas de propagación libre. A través de este estudio de un escenario de carga complejo, buscamos mejorar nuestra comprensión de la interacción intrincada entre los modos de fractura y las características de la malla. Al investigar a fondo estos aspectos diferentes, hemos aportado información valiosas sobre el comportamiento y rendimiento de los modelos de simulación utilizados en esta tesis. Estos hallazgos profundizan nuestra comprensión de la mecánica de fracturas y sientan las bases para futuras investigaciones y desarrollos en este campo.

En resumen, esta tesis proporciona valiosas para la modelación de la estimulación de fracturas hidráulicas en yacimientos con fracturas naturales. Los hallazgos contribuyen a una mejor comprensión de los regímenes de propagación de fracturas, la interacción entre fracturas hidráulicas y naturales, y el desarrollo de algoritmos novedosos para mejorar la eficiencia computacional. La investigación realizada en este estudio sienta las bases para futuros avances en técnicas de simulación y optimización de fracturamiento hidráulico, llevando en última instancia a estrategias mejoradas de caracterización de yacimientos y optimización de la producción en yacimientos no convencionales.

Appendix A

Fracture propagation analysis: benchmarking and comparative study

Currently, there is a shortage of analytical or semi-analytical models available for comparing simulations of Hydraulic fractures interactions with discontinuities.

This annex provides a comprehensive and sequential guide, within the framework of Y-FRAC®, for obtaining an analytical benchmark and performing the corresponding verifications. We will commence with the straightforward scenario of straight propagation, incorporating the geometric propagation line. Subsequently, we will gradually escalate the complexity, eventually addressing the mixed-mode case involving an unstructured mesh. The proposed steps are outlined below.

- Straight propagation
    1. Mesh with a propagation line
        (a) Straight line mesh
        (b) Angled line mesh
    2. Unstructured mesh
- Mixed Mode Propagation
    1. Unstructured mesh

These validations lay the foundations for the study and validation of $Y - FRAC^{®}$ in fracture deflection performed in Chapter 5.

In section A.1, we provide a comprehensive description of the simulation setup employed throughout this Appendix. This includes the specific parameters, conditions, and methodologies utilized to conduct the simulations discussed herein.

Moving forward, in section A.2, we delve into an in-depth examination of straight propagation. This investigation encompasses the exploration of various mesh types, namely structured and unstructured meshes, to gain insights into their respective effects on fracture behavior and propagation.

Furthermore, in section A.3, we shift our focus towards the analysis of mixed-mode loading with free propagation paths, specifically considering the influence of unstructured meshes. By studying this complex loading scenario, we aim to gain a more comprehensive understanding of the intricate interplay between fracture modes and mesh characteristics.

By thoroughly investigating these different aspects, we aim to provide valuable insights into the behavior and performance of the simulation models utilized in this Appendix.

A.1 Simulations setup

This section presents a detailed overview of the simulation setup adopted for the analysis conducted in this Appendix. We provide an in-depth description of the specific parameters, conditions, and methodologies employed to ensure the accuracy and reliability of the simulations discussed herein.

In subsection A.1.1, we focus on describing the boundary conditions applied in the simulations. These conditions play a crucial role in shaping the behavior of the fractures and are essential for accurately capturing the real-world scenarios under investigation.

Continuing further, subsection A.1.2 delves into an elaborate explanation of the loading mode and the corresponding algorithm implemented within the Y-FRAC® software. This detailed account sheds light on the methodology employed to effectively simulate the applied loads and their impact on the fracture propagation process.

Additionally, in subsection A.1.2.1, we provide comprehensive insights into the numerical factors utilized within the propagation algorithm. These factors play a vital role in controlling and accurately representing the behavior and progression of fractures during the simulations.

By thoroughly describing these essential components of the simulation setup, we aim to establish a solid foundation and ensure transparency and reproducibility in the experimental process undertaken in this thesis.

A.1.1 MBL boundary conditions

The mesh utilized for the simulations in this study consists of a rectangular model with a pre-existing crack, illustrated in Fig. A.1. To accurately represent the desired loading, we applied displacement values along the boundaries of the mesh model. These displacements were determined based on the specified K_I (stress intensity factor) and the mesh fracture length, serving as essential inputs for defining the boundary conditions.

Specifically, for mode I loading, the following LEFM displacements were applied:

$$u_{x,MBL} = \frac{K_I}{2\mu}\sqrt{\frac{r}{2\pi}}\cos\left(\frac{\theta}{2}\right)\left[\kappa - 1 + 2\sin^2\left(\frac{\theta}{2}\right)\right] \tag{A.1}$$

$$u_{y,MBL} = \frac{K_I}{2\mu}\sqrt{\frac{r}{2\pi}}\sin\left(\frac{\theta}{2}\right)\left[\kappa + 1 - 2\cos^2\left(\frac{\theta}{2}\right)\right] \tag{A.2}$$

where μ represents the shear modulus and $\kappa = 3 - 4\nu$ in plane strain.

For mode II loading, the displacements corresponding to K_{II} are as follows:

$$u_{x,MBL} = \frac{K_{II}}{2\mu}\sqrt{\frac{r}{2\pi}}\sin\left(\frac{\theta}{2}\right)\left[\kappa + 1 + 2\cos^2\left(\frac{\theta}{2}\right)\right] \tag{A.3}$$

$$u_{y,MBL} = -\frac{K_{II}}{2\mu}\sqrt{\frac{r}{2\pi}}\cos\left(\frac{\theta}{2}\right)\left[\kappa - 1 - 2\sin^2\left(\frac{\theta}{2}\right)\right] \tag{A.4}$$

For mixed mode loading, the displacements are obtained by combining the displacements for modes I and II.

To ensure the validity of the boundary conditions, it is crucial for the size of the plastic zone developing at the crack tip to be small relative to the overall model size. This approach, known as the Modified Boundary Layer (MBL) analysis, enables the simulation of near-tip conditions in arbitrary geometries while containing plasticity within the body. It involves removing a core region from the crack tip and constructing a free-body diagram.

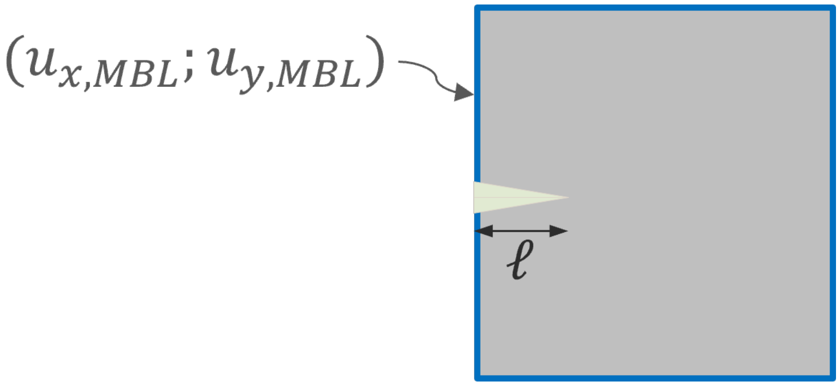

Figure A.1: Modified Boundary Layer boundary conditions scheme.

The implementation of these boundary conditions offers flexibility for incorporating future developments and easy modification of boundary conditions.

Furthermore, it is important to note that the boundary conditions are inferred from an elastic solution (Anderson, 2017). This study focuses on the MBL analysis, which allows for accurate representation of the crack propagation phenomenon while ensuring the containment of plasticity within the body.

A.1.2 Loading algorithm

We have developed a simulation algorithm, as illustrated in Fig. A.2, to facilitate the implementation of the proposed methodology. This algorithm encompasses the application of displacement boundary conditions ($u_{x,MBL}$,$u_{y,MBL}$) based on Eqs. (A.1) to (A.4). The algorithm takes into account initial input values, including the initial K_I (K_{I0}) and the initial fracture half-length (ℓ_0).

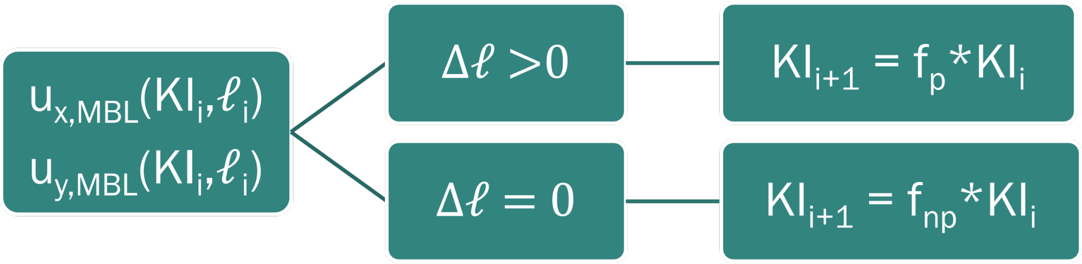

Figure A.2: Simulation algorithm designed to enhance propagation with constant K_I.

The simulation proceeds through a dynamic relaxation solver, which solves the solid mechanics problem. During each step, the algorithm evaluates whether fracture propagation occurs by examining the change in crack length ($\Delta\ell > 0$). If propagation is detected, the algorithm proceeds to the next step $(i+1)$ and computes the updated value of K_I $(K_{I,i+1})$ by applying a propagation factor (f_p) to the previous K_I value $(K_{I,i})$. This factor can be either less than or greater than unity, allowing for a decrease or increase in $K_{I,i}$, respectively.

In cases where no fracture propagation takes place $(\Delta\ell = 0)$, the algorithm calculates the updated value of K_I $(K_{I,i+1})$ for the subsequent step by applying a No propagation factor, f_{np}, to $K_{I,i}$. It is important to note that the No propagation factor always assumes values greater than unity $(f_{np} > 1)$, ensuring a gradual increase in $K_{I,i}$ compared to the previous step. This incremental adjustment continues until fracture propagation is observed.

By incorporating these conditions and factors into our algorithm, we have developed a robust framework that enables accurate simulation of fracture propagation. The algorithm is designed to maintain a constant value of K_I throughout the simulation process, thereby favoring the propagation of the crack. This iterative approach allows us to effectively capture the intricate complexities associated with crack growth and gain valuable insights into the fracture behavior under a wide range of loading conditions. Through this methodology, we can explore and analyze the critical aspects of fracture mechanics, shedding light on the mechanisms that govern crack propagation and its implications in real-world scenarios.

A.1.2.1 Propagation factors

In this section, we focus on optimizing the propagation factor values for fracture propagation. We investigate the effect of the propagation factor variations, as shown in Figure A.3a. As expected, higher values of f_p lead to an increase in K_I during propagation. However, it is important to note that this increase in K_I is an artifact caused by plotting the imposed K_I at each step of the simulation with boundary conditions, rather than the equilibrium K_I obtained at the end of each step. To address this, we calculated the final K_I values for selected steps using stress regression, as illustrated by the circles in Figure A.4a. The results clearly demonstrate that despite the initial increase in K_I, the fracture propagates with a constant K_I value (represented by the circles). This finding validates the stability and accuracy of our simulation approach.

Next, we examine the variations in the no propagation factor, presented in Figure

A.3b. Consistent with expectations, higher values of f_{np} contribute to increased scatter in K_I during propagation.

The maximum value of f_{np} leads to a length jump of one finite element. It is worth noting that using higher values of f_{np} may result in "jumps" of more than one element at each step. To ensure controlled propagation, we analyze the length jump ($\Delta\ell$) for the simulation with $f_{np} = 1.001$, as depicted in Figure A.4b. The plot confirms that $\Delta\ell \leq 1$ for all cases.

The determination of the maximum value for f_{np} depends on factors such as the length of the finite element and the physical properties of the system. An estimation of the maximum f_{np} can be obtained based on equilibrium curves, as described in the following section.

Through the optimization of the propagation factors and the analysis of their effects on fracture behavior, we enhance the accuracy and reliability of our simulation model. These findings provide valuable insights into the mechanisms underlying crack propagation and contribute to a more comprehensive understanding of fracture mechanics.

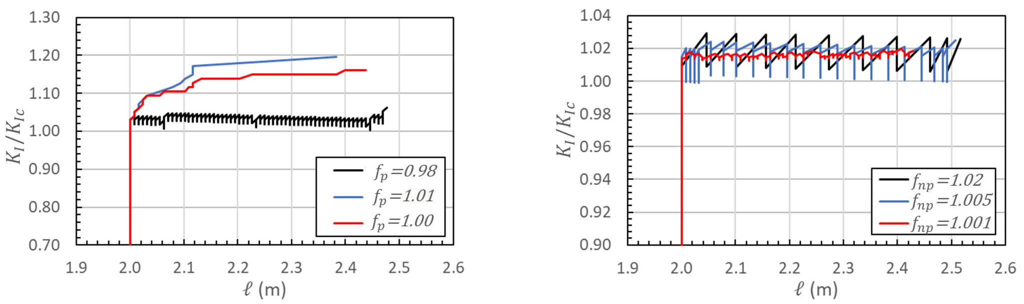

(a) Propagation factor.

(b) No propagation factor

Figure A.3: K_I/K_{Ic} ratio as a function of fracture length ℓ for simulations with different propagation and No propagation factors.

A.1.2.2 Critical non propagation factor

To avoid jumps in the simulations we calculate the critical f_{np} that ensures $\Delta\ell \leq 1$. Given an initial set of Boundary conditions, $BC(\ell_i, K_{I,i})$, and a load increment $BC_i(\ell_i, K_{I,i}) \longrightarrow f_{np}BC_i$, the expected fracture advance, or propagation, $\ell_i \longrightarrow \ell_f$ can be estimated by assuming that in the region of interest the load curves $K_{I,i}(\ell_i, BC_i)$ and $K_{I,i}(\ell_i, f_{np}BC_i)$ are approximately parallel (i.e., $dK_I/d\ell \approx const.$). These curves are schematized in Fig. A.5. Therefore,

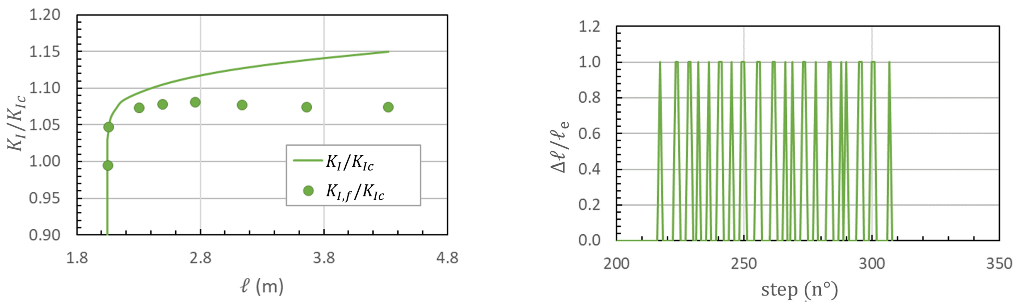

(a) (b)

Figure A.4: (*a*) Imposed, K_I, and calculated, $K_{I,f}$, stress intensity factors for a simulation with $f_p < 1$. (*b*) Fracture length propagation for step for a simulation with $f_{np} = 1.001$ and $\ell_e = 7.8 \times 10^{-3}$.

$$\Delta\ell \approx \frac{\Delta K_I}{\frac{dK_I}{d\ell}} \tag{A.5}$$

From the non propagation factor definition:

$$\Delta K_I = K_{I,i}(\ell_i, BC_i) - K_{I,i+1}(\ell_i, f_{np}BC_i) = (f_{np} - 1)K_I(\ell_i, BC_i) \tag{A.6}$$

For the critical f_{np} we assume $\Delta L = \ell_e$, then

$$\ell_e = \frac{\Delta K_I}{\frac{dK_I}{d\ell}} \tag{A.7}$$

Introducing Eq. (A.6) into (A.7) we get

$$(f_{np,c} - 1)K_I = \ell_e \frac{dK_I}{d\ell} \tag{A.8}$$

where $f_{np,c}$ is the critical non propagation factor. Clearing,

$$f_{np,c} = 1 + \frac{\ell_e}{K_I}\frac{dK_I}{d\ell} \tag{A.9}$$

With Eq. (A.9), and calculating $\frac{dK_I}{d\ell}$ in one simulation, we can estimate the critical non propagation factor for simulations with the same physical parameters.

In Fig.A.6 we have an example of $f_{np,c}$ application. We show two simulation results with equal physical parameters and different propagation factors. The first with $f_{np,c} = 1.01$ and the second with $f_{np,c} = 1.001$. The results shows that simulation with higher factor ($f_{np,c} = 1.01$) had fracture length jumps, while the simulation with smaller factor not. With dashed lines are plotted the critical non propagation factors

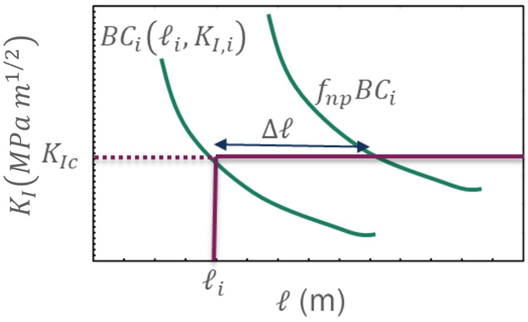

Figure A.5: Stress intensity factor vs. fracture length curves on a step with fracture propagation $Delta\ell$. Curves correspond to initial, BC_i, and final $BC_f = f_{np}BC_f$ boundary conditions.

during propagation. The average critical non propagation factor (for both simulations) is $f_{np,c} \approx 1.0085$. This result explains why simulation with $f_{np} = 1.01 > f_{np,c}$ had jumps while simulation with $f_{np} = 1.001 < f_{np,c}$ not.

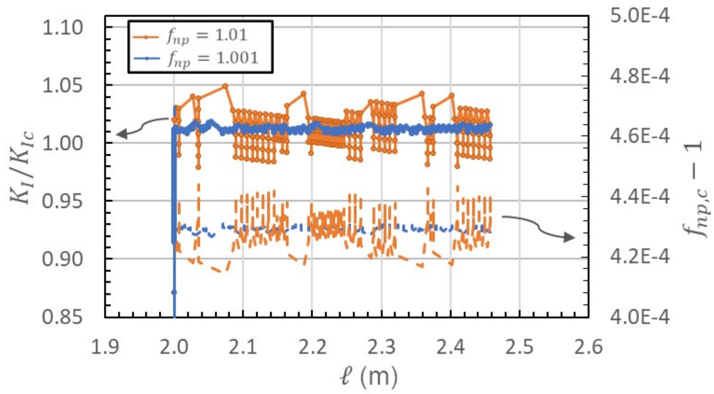

Figure A.6: K_I/K_{Ic} vs. ℓ and $f_{np,c}$ vs. ℓ plots for two simulations: The first with $f_{np,c} = 1.01$ and the second with $f_{np,c} = 1.001$.

A.2 Straight propagation

In this section, we delve into the fundamental scenario of straight fracture propagation by incorporating an applied K_I through the utilization of MBL boundary conditions, as previously explained in section A.1.1.

To comprehensively explore this topic, we will begin by conducting simulations that consider different types of propagation lines, including both right and angled configurations. The details of these simulations can be found in sub-section A.2.1. Subsequently, we will proceed to investigate simulations involving unstructured meshes, which will be discussed in depth in sub-section A.2.2.

By systematically examining these distinct aspects, we aim to gain a comprehensive understanding of the behavior and characteristics of fracture propagation in the given context.

A.2.1 Simulations with geometric propagation line

In this section, we investigate the impact of mesh orientation on the propagation behavior. To explore this aspect, we conducted simulations by varying the geometric angle ω of the mesh, as illustrated in the schematic diagram presented in Fig. A.7.

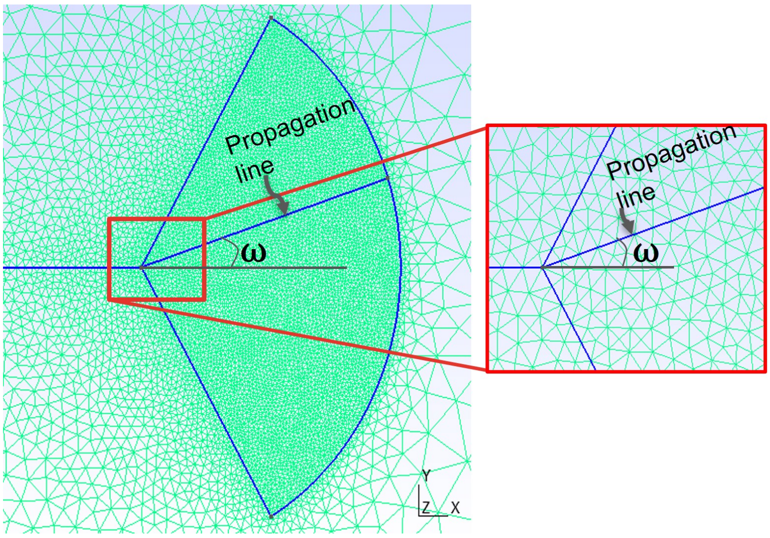

Figure A.7: Scheme of the mesh with propagation line at an ω angle.

We will first study the particular case of $\omega = 0$ and then we will study increasing this angle.

A.2.1.1 Straight propagation line

A particular case of angled propagation line occurs when $\omega = 0$, where the geometric line aligns with the original fracture propagation line. On this particular case, we obtained a fracture propagating at constant $K_I = K_{Ic}$ with less than 1% error, as shown in Fig. A.8 with a red line.

A.2.1.2 Angled propagation line

Fig. A.8 shows the K_I/K_{Ic} vs. ℓ plots for simulations with $\omega > 0$. We observed propagation with some scatter compared to the $\omega = 0$ case. Additionally, there was an increase in K_I for larger ω angles. This dispersion is associated with the mixed mode propagation on the angled propagation line. Similar dispersion was observed on unstructured meshes, as analyzed in section A.2.2. Furthermore, we noticed that increasing the mesh angle resulted in growing K_I values during propagation, instead of constant values as observed with $\omega = 0$.

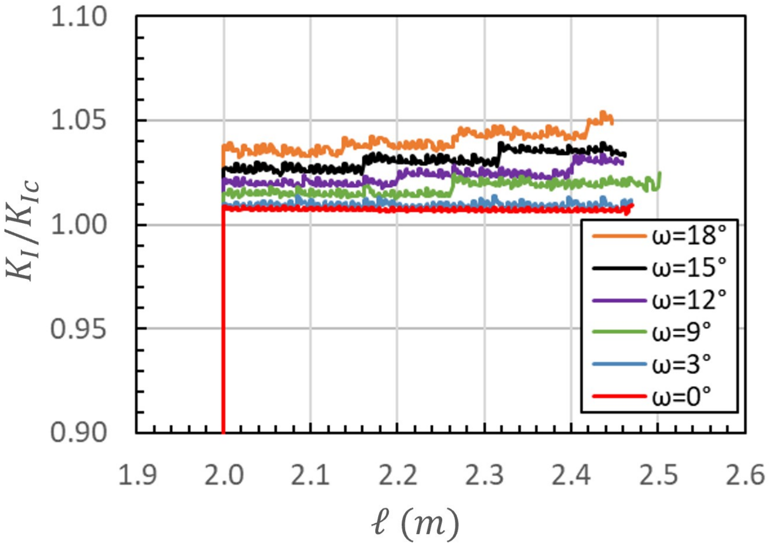

Figure A.8: K_I/K_{Ic} vs. fracture length results for simulations with geometric propagation lines at an ω angle.

A.2.2 Free path propagation

In this section, we investigate the impact of eliminating the geometrical propagation mesh path and employing unstructured meshes to enable free path propagation. Figure A.9b illustrates an example of an unstructured mesh. Here, ℓ represents the cumulative length of all open elements, while ℓ_d denotes the straight line distance from the initial fracture to the last fractured element, as depicted in Figure A.9b.

In Fig. A.10, we present the results of fracture length as a function of K_I/K_{Ic} obtained using an unstructured mesh and the propagation line ($\omega = 0°$).

The first noteworthy observation is that the propagation initiates at approximately $K_I \approx 1.06 K_{Ic}$, whereas the simulation with the propagation line propagated at $K_I \approx K_{Ic}$. This disparity can be attributed to the additional energy consumption that occurs when generating a cohesive zone with branching in non-oriented meshes, as depicted in Fig. A.11b.

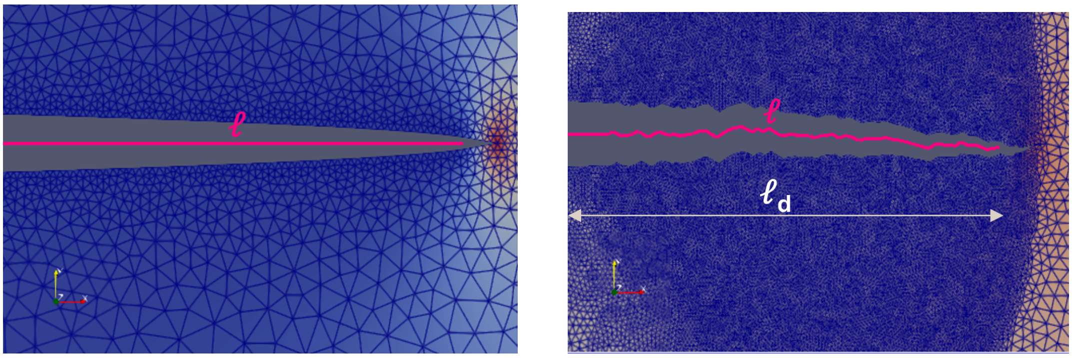

(a) Mesh with propagation line. (b) Mesh without propagation line.

Figure A.9: Meshes with and without propagation line for free path propagation analysis. ℓ is the sum of all open elements length and ℓ_d is the straight line distance from the initial fracture to the last fractured element.

Furthermore, it is worth noting that there is a certain level of dispersion in the values of K_I/K_{Ic}. Additionally, the parameter K_I exhibits a positive slope, indicating an increase in its magnitude as propagation takes place.

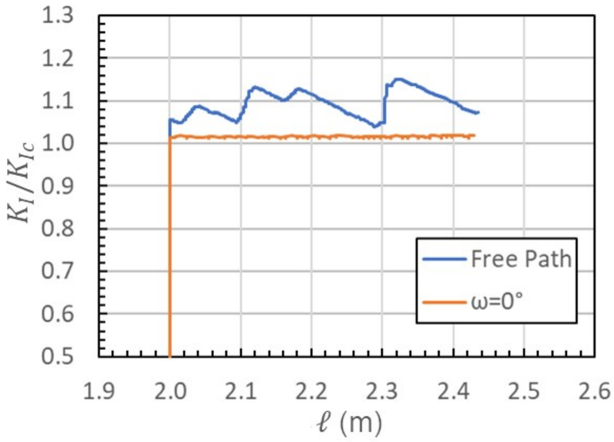

Figure A.10: Non dimensional stress intensity factor vs. fracture length curves for two simulations with different mesh types. The first with an unstructured mesh, and the second with a geometric propagation line aligned with the main fracture.

To better understand the reasons behind this increase in the necessary K_I value for propagation, we conducted an energy analysis on both the simulation with a propagation line and the one with an unstructured mesh.

A.2.2.1 Energy Analysis

We aim to establish a connection between the increase in K_I during propagation through the energy analysis performed on both the simulation with a propagation line and the

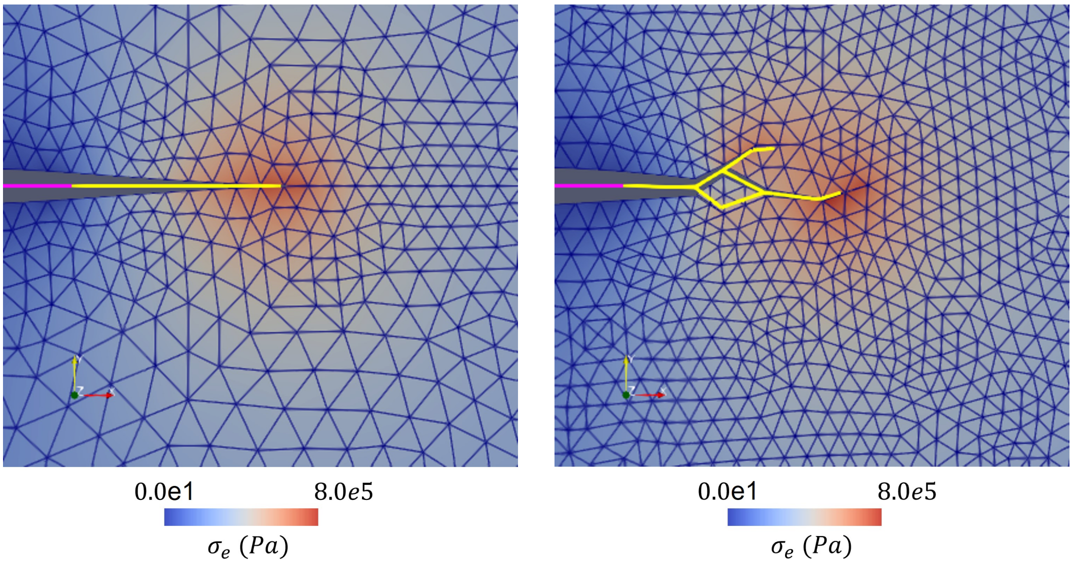

(a) Simulation with propagation line. (b) Simulation without propagation line.

Figure A.11: Cohesive zone development in simulations with pre-defined propagation path and with free propagation. In yellow are indicated the cohesive zones and in magenta the fractured zones. Branching is observed on the if free path simulation.

one using an unstructured mesh.

Here, W_f represents the energy consumed during the simulation for fracture propagation, W_c denotes the energy consumed in opening cohesive zones (separation greater than zero but less than the critical value), and W_d stands for the total energy consumption associated with damage during fracture propagation, encompassing both fractured and cohesive energies.

$\tilde{W}_{theo}$ is the theoretical fractured energy, calculated on each step as:

$$\tilde{W}_{theo} = G_c \Delta \ell, \tag{A.10}$$

where $\Delta\ell$ is the fractured length increase between the previous and the current step.

W_{theo} is the theoretical total damaged energy, including cohesive and fractured zones, calculated on each step as:

$$W_{theo} = G_c \Delta(\ell + c), \tag{A.11}$$

where $\Delta(\ell + c)$ is the total damaged length increase between the previous and the current step.

The energy results for the simulation with propagation line are shown in Fig. A.12a. The fractured energy is equal to $\tilde{W}_{theo}$, while the consumed energy falls between $\tilde{W}_{theo}$

and W_{theo}, as expected. Furthermore, the difference in consumed energy between $\tilde{W}_{theo}$ and W_{theo} remains constant throughout the entire simulation.

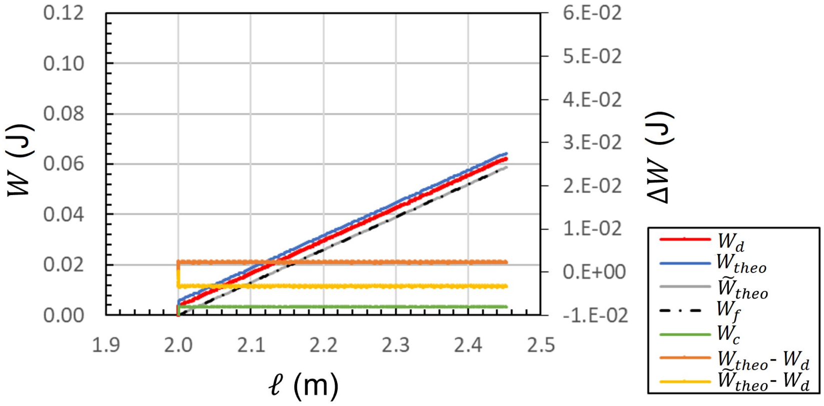

(a) Simulation with propagation line.

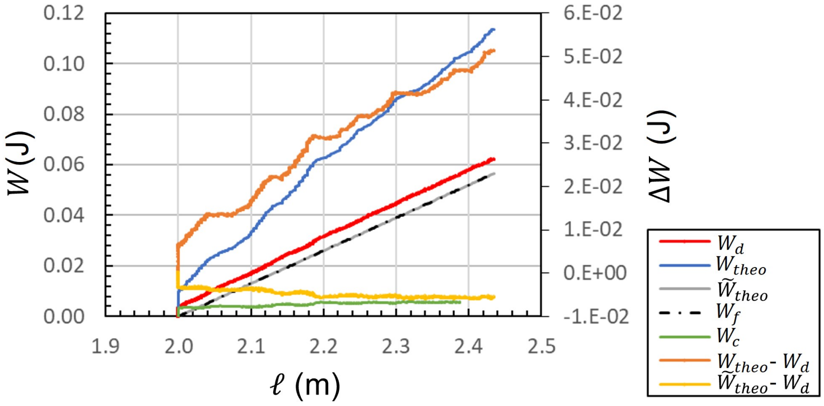

(b) Simulation without propagation line.

Figure A.12: Energy calculations for simulations with propagation line and unstructured mesh.

One significant difference observed between the two simulations is that W_{theo} undergoes a much larger increase during propagation in the unstructured mesh simulation. This is because this energy takes into account the entirety of the damaged zones (with irreversible damage greater than zero). Due to the occurrence of branching during propagation, the length of these damaged zones is much greater compared to the simulation with a propagation line.

In Figure A.13, we can observe the development of the damaged zone for both simulations, clearly illustrating how L_c increases during propagation in the case of unstructured mesh (free path). In the simulation with a propagation line, no branching occurs, and as a result, the cohesive length remains constant during propagation.

In Fig. A.14, we present the total energy consumed during propagation for both simulations. The graph illustrates that the energy consumption increases as propagation

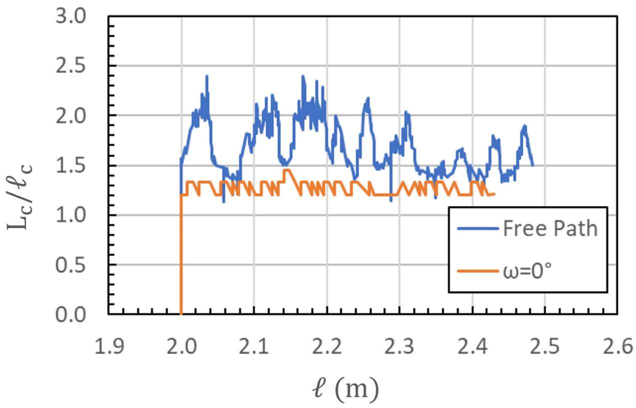

Figure A.13: Ratio of damaged zone length to theoretical cohesive length for simulations with propagation line and unstructured mesh as a function of fracture length.

progresses in the case of the unstructured mesh simulation, once again due to the typical branching observed in this type of mesh.

Thus, we can confirm that there is an increase in energy consumption during propagation in unstructured meshes compared to straight-line propagation. This increase is attributed to the generation of damaged zones around the fracture (branching), which require energy for their formation.

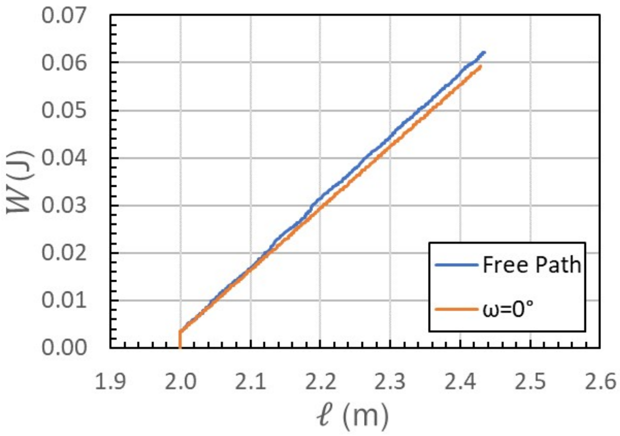

Figure A.14: Non dimensional stress intensity factor vs. fracture length curves for two simulations with different mesh types. The first with an unstructured mesh, and the second with a geometric propagation line aligned with the main fracture.

A.3 Mixed mode propagation

A.3.1 Introduction

The propagation of a 2D fracture according to LEFM is a function of the stress intensity factors in opening (K_I) and shear (K_{II}) modes, which are a measure of the concentration of stresses in the fracture tip (Lawn, 2004). Both factors are combined into the Energy Release Rate (ERR) G by Irwin's relationship (Irwin, 1957),

$$G = \frac{{K_I}^2 + {K_{II}}^2}{E'} \tag{A.12}$$

If G is greater than a certain critical value, called G_c, the fracture will propagate. The direction in which the fracture propagates is the one that maximizes G. The energy release rate $\bar{G}$ at an orientation θ_0 (defined in the coordinate system of the fracture tip) can be calculated as (Nuismer, 1975).

$$G_\theta = \frac{\bar{k}_{1\theta}^2 + \bar{k}_{2\theta}^2}{E'} \tag{A.13}$$

where $\bar{k}_{1\theta}$ and $\bar{k}_{2\theta}$ are

$$\bar{k}_{1\theta} = \frac{1}{2}\cos\frac{\theta_0}{2}([K_I(1+\cos\theta_0) - 3K_{II}\sin\theta_0]) \tag{A.14}$$

$$\bar{k}_{2\theta} = \frac{1}{2}\cos\frac{\theta_0}{2}([K_I\sin\theta_0 + K_{II}(1+\cos\theta_0)]) \tag{A.15}$$

Hutchinson and Suo (1991) performed an exhaustive analysis and corresponding numerical calculations for more general cases when the kink has finite length. In that circumstance, the ratio of the ERR of the primary fracture when it propagates in a straight line (G_0) to that of the kink (G_θ) is as follows (Hutchinson and Suo, 1991).

$$G_0/G_\theta = F(\theta, \psi, \eta), \tag{A.16}$$

where $\psi = \arctan(K_{II}/K_I)$ is the measurement of the mode II to mode I load acting on the main fracture, called the phase angle of the load. η is the in-plane stress parameter. In what follows, we limit our discussion to the initiation of the kink. Therefore, the kink has zero length.

In order to obtain the explicit expression of Eq. (A.13), we must consider that the circumferential stress is related to $\bar{k}_{1\theta}$ through $\sigma_{\theta\theta} = \bar{k}_{1\theta}/\sqrt{2\pi r}$ (Zeng and Wei, 2017), where r is the radial coordinate of the local polar coordinate system shown in Fig. A.15.

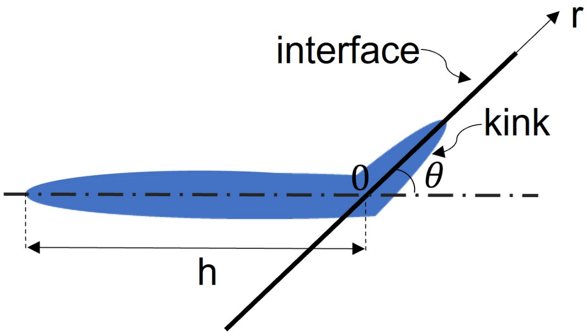

Figure A.15: Schematic of a fracture with kink and the polar coordinate system at the fracture tip.

Substituting the expressions for $\bar{k}_{1\theta}$ and $\bar{k}_{2\theta}$ in Eq. (A.13) we obtain the expression for the kink ERR as a function of K_I and K_{II} of the main fracture:

$$G_\theta = \frac{\cos^2\frac{\theta}{2}[{K_I}^2 + 5{K_{II}}^2 + ({K_I}^2 - 3{K_{II}}^2)\cos\theta - 4K_IK_{II}\sin\theta]}{2E'} \tag{A.17}$$

Therefore, the relationship between the main fracture energy release rate (G_0) and the maximum release rate ($G_{\theta max}$) is

$$\frac{G_0}{G_{\theta max}} = \frac{4}{(1+\cos\theta_0)(2\cos(\theta_0+\psi) - 2\cos(2\psi) - \cos\theta_0 + 3)} \tag{A.18}$$

where θ_0 is the angle corresponding to $G_{\theta max}$. Fig. A.16 shows plots this ratio for different values of ψ. By maximizing Eq. (A.17) with respect to θ we can find the expression of θ_0 for which we have the maximum rate of kink energy release ($G_{\theta max}$), according to the following expression Zeng and Wei (2017)

$$\theta_0 = acos\left(\frac{3{K_{II}}^2 + \sqrt{{K_I}^2 + 8{K_I}^2{K_{II}}^2}}{{K_I}^2 + 9{K_{II}}^2}\right) \tag{A.19}$$

which can also be expressed as a function of the biaxiality parameter ψ

$$\theta_0 = acos\left(\frac{3tan^2\psi + \sqrt{1 + 8tan^2\psi}}{1 + 9tan^2\psi}\right) \tag{A.20}$$

and can be seen graphically in Fig. A.16.

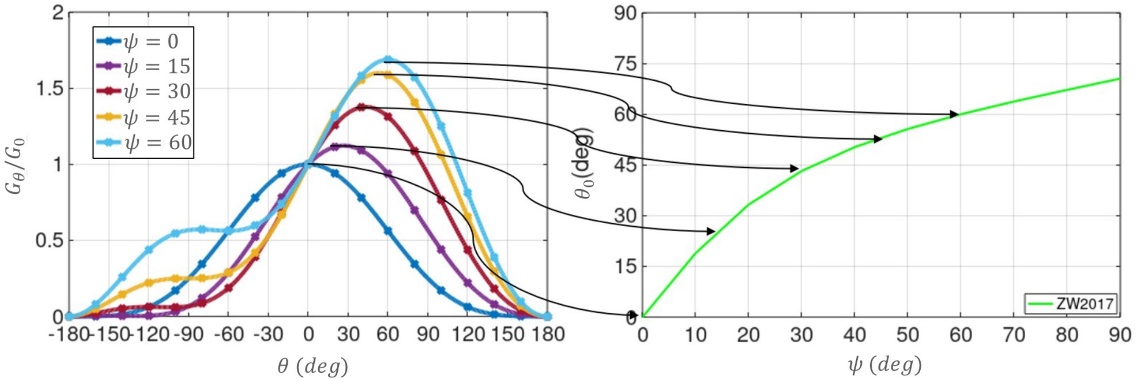

(a)

Figure A.16: Ratio of the ERR of the primary fracture when it propagates in a straight line, G_0, to that of the kink, G_θ, as a function of the kink angle θ for various phase angles ψ (Left). And kink angle θ_0 corresponding to the maximum energy release rate $G_{\theta max}$ as a function of phase angle ψ (Right). The black arrows indicate the correspondence of the maximum points of G_θ on the left with the corresponding angle θ_0 on the right.

A.3.2 Results

In this section we analyze the simulations results to validate Y-FRAC® for mixed-mode fracture branching. We applied different phase angles ψ to an unstructured mesh. For each step, K_{II} was calculated in order to keep $\psi = const.$ through all the simulation. For each simulation, we obtained a kinking angle, and a propagation load (K_I). This results are shown in Fig. A.17.

In Fig. A.17a, the plots of K_I/K_{Ic} as a function of fracture length for simulations with different values of ψ are shown. It can be observed that, as expected, increasing the mode mixity, i.e., increasing ψ, decreases K_I/K_{Ic} during propagation. Similar as obtained for straight propagation with unstructured mesh, there is some dispersion and an increase in K_I during propagation, associated with the extra energy consumption due to branching.

In order to characterize mixed-mode fracture, we can define the effective stress intensity factor as $K^* = \sqrt{{K_I}^2 + {K_{II}}^2}$. In Fig. A.18a, we plot K^* as a function of fracture length. This graph allows us to observe more clearly the increase in K^* during propagation. It is evident that as the fracture length increases, the mixed-mode stress intensity factor also increases. The increase in K^* during propagation highlights the importance of considering mixed-mode effects in fracture mechanics analysis.

In Fig. A.17b, the kink angles are plotted as a function of the phase angle, along with the theoretical curve of θ_0 described in section A.3.1. We can see that there is very good agreement between the results obtained with Y-FRAC® and the theory.

The kinking angles, as shown in Fig. A.17b, are graphed against the phase angle. Additionally, the theoretical curve of θ_0, as discussed in section A.3.1, is included in the plot. The results obtained with Y-FRAC® exhibit a remarkable agreement with the theoretical predictions. This strong correlation further validates the accuracy and reliability of Y-FRAC® in simulating mixed-mode fracture propagation.

Furthermore, in Fig. A.18b, the ratio K_{II}/K_{Ic} is plotted against the ratio K_{II}/K_{Ic} for all the conducted simulations. The graph also includes the theoretical curve determined by the energy criterion $G = G_c$. As observed, as the mode mixity increases, the results deviate from the energy curve, and fracture begins to propagate at $G < G_c$. This behavior is attributed to failure by stresses occurring before the energy criterion is met. The effect is more prominent with larger phase angles, while it is practically negligible with smaller phase angles.

The close match between the experimental data and the theoretical curve provides confidence in the predictive capabilities of the model, thereby contributing to the overall understanding of mixed-mode fracture behavior.

In summary, the comprehensive simulations conducted using Y-FRAC® demonstrate its effectiveness in modeling mixed-mode fracture branching. The results exhibit agreement with theoretical predictions, highlighting the importance of considering mixed-mode effects in fracture mechanics analysis. These findings contribute to advancing our understanding of fracture behavior under mixed-mode conditions.

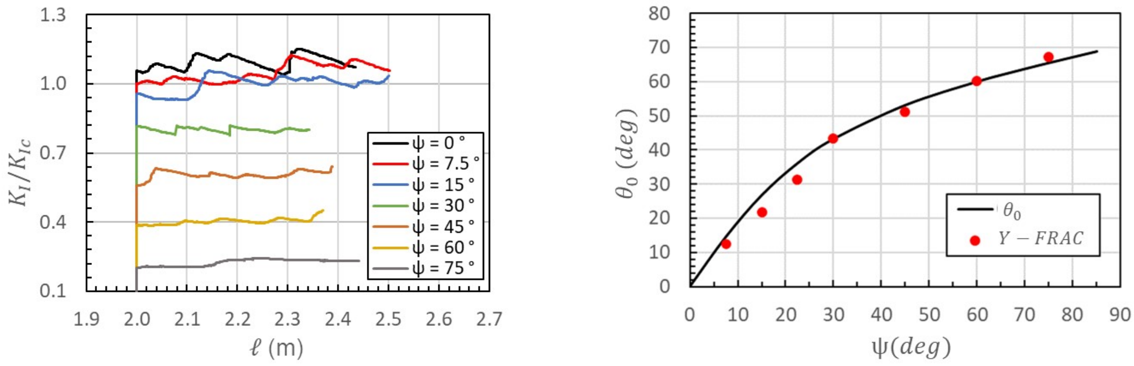

(a) (b)

Figure A.17: a) Ratio of Mode I Fracture Toughness to fracture length for simulations with different phase angles ψ. b) Kink angle θ_0 versus phase angle ψ. The curve represents the theoretical kinking angle, while the red dots indicate the mean propagation angle obtained from the simulations.

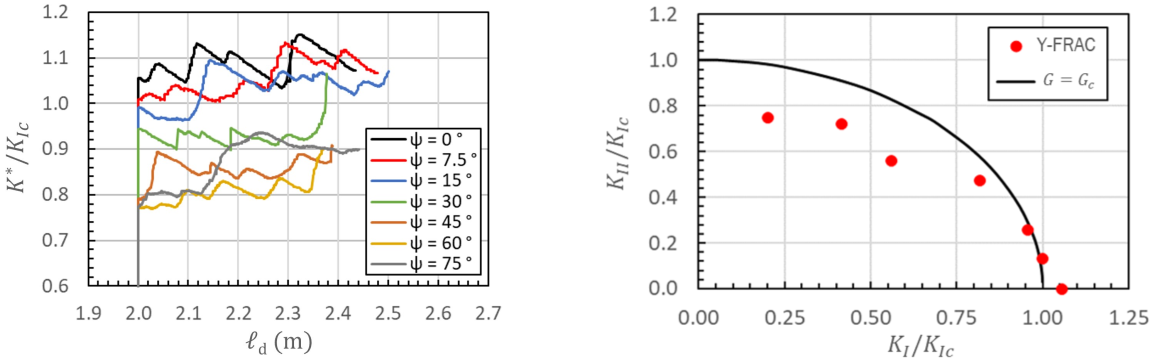

(a) (b)

Figure A.18: a) Ratio of effective stress intensity factor to critical traction intensity factor as a function of fracture length for simulations with various phase angles. b) Non dimensional stress intensity factor vs. fracture length curves for two simulations with different mesh types. The first with an unstructured mesh, and the second with a geometric propagation line aligned with the main fracture.

Bibliography

Aguilera, R. F. and Radetzki, M. (2014). The shale revolution: Global gas and oil markets under transformation. *Miner. Econ.*, 26:75–84. 19, 30

Alam, M., Grimm, B., and Parmigiani, J. P. (2016). Effect of incident angle on crack propagation at interfaces. *Eng. Frac. Mech.*, 162:155–163. 10, 11, 81, 83, 85, 91, 94

Alam, M., Parmigiani, J. P., and Kruzic, J. J. (2017). An experimental assessment of methods to predict crack deflection at an interface. *Engineering Fracture Mechanics*, 181:116–129. 13, 103, 104

Alfano, G. and Crisfield, M. (2001). Finite element interface models for the delamination analysis of laminated composites: mechanical and computational issues. *Int. J. Numer. Methods Eng.*, 50(7):1701–1736. 112, 113

Anderson, T. L. (2017). *Fracture Mechanics: Fundamentals and Applications*. CRC press. 88, 97, 138

Arroyo, M. and Trepat, X. (2017). Hydraulic fracturing in cells and tissues: Fracking meets cell biology. *Curr. Opin. Cell Biol.*, 44(6):1–6. 40

As, A. V. and Jeffrey, R. (2000). Hydraulic fracturing as a cave inducement technique at Northparkes Mines. In *Pacific Rocks 2000*, pages ARMA–2000–0353, Rotterdam, Amsterdam. 40

Ba Geri, M., Imqam, A., and Flori, R. (2019). A critical review of using high viscosity friction reducers as fracturing fluids for hydraulic fracturing applications. In *SPE Oklahoma city oil and gas symposium*. OnePetro. 21, 32, 33

Barati, R. and Liang, J.-T. (2014). A review of fracturing fluid systems used for hydraulic fracturing of oil and gas wells. *J. Appl. Polym. Sci.*, 131(16). 20, 21, 32

Barenblatt, G. I. (1959). The formation of equilibrium cracks during brittle fracture. general ideas and hypotheses. axially-symmetric cracks. *J. Appl. Math. Mech*, 23(3):622–636. 25, 37

Barenblatt, G. I. (1962). The mathematical theory of equilibrium cracks in brittle fracture. *Adv. Appl. Mech.*, 7:55–129. 25, 37, 44, 63

Basirat, R., Goshtasbi, K., and Ahmadi, M. (2019). Geomechanical key parameters of the process of hydraulic fracturing propagation in fractured medium. *Oil & Gas Science and Technology–Revue d'IFP Energies nouvelles*, 74:58. 23, 35

Bažant, Z. P. and Planas, J. (1997). *Fracture and Size Effect in Concrete and Other Quasibrittle Materials*. Routledge. 113

Bertani, R. (2016). Geothermal power generation in the world 2010–2014 update report. *Geothermics*, 60:31–43. 21, 32

Blanton, T. (1982). An experimental study of interaction between hydraulically induced and pre-existing fractures. In *SPE Unconventional Gas Recovery Symposium, Pittsburgh, Pennsylvania, May 16–18, 1982*, pages 559—571. (SPE-10847-MS). 9, 69

Breede, K., Dzebisashvili, K., Liu, X., and Falcone, G. (2013). A systematic review of enhanced (or engineered) geothermal systems: Past, present and future. *Geotherm. Energy*, 1(1):4. 40

Bunger, A. P. and Detournay, E. (2007). Early-time solution for a radial hydraulic fracture. *J. Eng. Mech.*, 133(5):534–540. 41, 42, 50

Bunger, A. P., Detournay, E., and Jeffrey, R. G. (2005). Crack tip behavior in near-surface fluid-driven fracture experiments. *C. R. - Mec.*, 333(4):299–304. 41

Camacho, G. T. and Ortiz, M. (1996). Computational modelling of impact damage in brittle materials. *Int. J. Solids Struc.*, 33(20-22):2899–2938. 63

Carpinteri, A., Cornetti, P., Barpi, F., and Valente, S. (2003). Cohesive crack model description of ductile to brittle size-scale transition: Dimensional analysis vs. renormalization group theory. *Eng. Frac. Mech.*, 70(14):1809–1839. 67

Celleri, H. M., Serebrinsky, S. A., and Sánchez, M. (2018). Coupled simulation of the interaction of a hydraulic hracture with a natural fracture. In *52nd U.S. Rock Mechanics/Geomechanics Symposium*, pages ARMA–2018–1319, Seattle, Washington, USA. American Rock Mechanics Association. 41

Chen, Z., Jeffrey, R. G., Zhang, X., and Kear, J. (2017). Finite-element simulation of a hydraulic fracture interacting with a natural fracture. *SPE J.*, 22(01):219–234. 25, 37

Chuprakov, D., Melchaeva, O., and Prioul, R. (2014). Injection-sensitive mechanics of hydraulic fracture interaction with discontinuities. *Rock Mech. Rock Eng.*, 47(5):1625–1640. 61, 81

Damjanac, B., Detournay, C., and Cundall, P. A. (2016). Application of particle and lattice codes to simulation of hydraulic fracturing. *Comput. Part. Mech.*, 3(2):249–261. 23, 35

De Pater, C. and Beugelsdijk, L. (2005). Experiments and numerical simulation of hydraulic fracturing in naturally fractured rock. In *Alaska Rocks 2005, The 40th US Symposium on Rock Mechanics (USRMS)*. OnePetro. 23, 35

Detournay, E. (2004). Propagation regimes of fluid-driven fractures in impermeable rocks. *Int. J. Geomech.*, 4(1):35–45. 40, 44, 47, 50

Detournay, E. (2016). Mechanics of hydraulic fractures. *Annu. Rev. Fluid Mech.*, 48:311–339. 41, 48, 79

Dugdale, D. (1960). Yielding of steel sheets containing slits. *J. Mech. Phys. Solids*, 8(2):100–104. 25, 37, 44, 46, 63

Dundurs, J. (1969). Discussion: "Edge-bonded dissimilar orthogonal elastic wedges under normal and shear loading" (Bogy, D. B., 1968, J. Appl. Mech., 35, pp. 460–466). *J. Appl. Mech.*, 36(3):650–652. 86

Economides, M. and Nolte, K., editors (2000). *Reservoir Stimulation, 3rd Ed.* John Wiley & Sons, Chichester, UK. 19, 23, 30, 34, 40

Economides, M. J., Martin, T., et al. (2007). *Modern fracturing: Enhancing natural gas production.* ET publishing Houston. 21, 33

Falk, M. L., Needleman, A., and Rice, J. R. (2001). A critical evaluation of cohesive zone models of dynamic fracture. *J. Phys. IV*, 11(Pr5):43—-50. 63, 67

Foulk III, J., Johnson, G., Klein, P., and Ritchie, R. (2008). On the toughening of brittle materials by grain bridging: Promoting intergranular fracture through grain angle, strength, and toughness. *J. Mech. Phys. Solids*, 56(6):2381–2400. 10, 11, 81, 82, 83, 84, 85, 90, 91, 94, 103, 105

Frank, U. and Barkley, N. (2005). Remediation of low permeability subsurface formations by fracturing enhancements of soil vapor extraction. *J. Hazard. Mater.*, 40:191–201. 40

Gale, J. F., Elliott, S. J., and Laubach, S. E. (2018). Hydraulic fractures in core from stimulated reservoirs: core fracture description of HFTS slant core, Midland Basin, West Texas. In *Unconventional Resources Technology Conference, Houston, Texas, 23-25 July 2018*, pages 1340–1357. Society of Exploration Geophysicists, American Association of Petroleum 20, 31

Gale, J. F., Laubach, S. E., Olson, J. E., Eichhubl, P., and Fall, A. (2014). Natural fractures in shale: A review and new observations. *Am. Assoc. Pet. Geol. Bull.*, 98(11):2165–2216. 19, 20, 23, 31, 34

Garagash, D. (2006a). Propagation of a plane-strain hydraulic fracture with a fluid lag: Early-time solution. *Int. J. Solids Struc.*, 43(18-19):5811–5835. 9, 41, 42, 49, 50, 53, 56, 57, 67, 68, 79, 118

Garagash, D. I. (2006b). Plane-strain propagation of a fluid-driven fracture during injection and shut-in: Asymptotics of large toughness. *Eng. Frac. Mech.*, 73(4):456–481. 26, 38, 123, 129

Garagash, D. I. (2019). Cohesive-zone effects in hydraulic fracture propagation. *J. Mech. Phys. Solids*, 133:103727. 79, 81

Geertsma, J. and De Klerk, F. (1969). A rapid method of predicting width and extent of hydraulically induced fractures. *J. Pet. Technol.*, 21(12):1571–1581. 40, 41, 42

Giovanardi, B., Serebrinsky, S., and Radovitzky, R. (2020). A fully-coupled computational framework for large-scale simulation of fluid-driven fracture propagation on parallel computers. *Comput. Meth. App. Mech. Eng.*, 372:113365. 41

Grimm, B. A. (2012). *Investigation into the role of strength and toughness in composite materials with an angled incident crack*. PhD thesis, Oregon State University, 2012. 90

Gu, H., Weng, X., et al. (2010). Criterion for fractures crossing frictional interfaces at non-orthogonal angles. In *44th US rock mechanics symposium and 5th US-Canada rock mechanics symposium*. American Rock Mechanics Association. 20, 31

Gu, H., Weng, X., Lund, J., Mack, M., Ganguly, U., and Suarez-Rivera, R. (2012). Hydraulic fracture crossing natural fracture at nonorthogonal angles: a criterion and its validation. *SPE Prod. Oper.*, 27(01):20–26. 20, 31, 61

Guo, J., Luo, B., Lu, C., Lai, J., and Ren, J. (2017). Numerical investigation of hydraulic fracture propagation in a layered reservoir using the cohesive zone method. *Eng. Frac. Mech.*, 186:195–207. 24, 25, 35, 37

Guo, J., Zhao, X., Zhu, H., Zhang, X., and Pan, R. (2015). Numerical simulation of interaction of hydraulic fracture and natural fracture based on the cohesive zone finite element method. *J. Nat. Gas Sci. Eng.*, 25:180–188. 25, 37

Gupta, V., Argon, A., and Suo, Z. (1992). Crack deflection at an interface between two orthotopic media. *J. Appl. Mech.* 82

Gutiérrez, J. and Serebrinsky, S. (2021). Propagation regimes, transition times, and approximate universality in 2d hydraulic fracture propagation with fluid lag. *Eng. Frac. Mech.*, 254:107905. 40

He, M.-Y., Bartlett, A., Evans, A. G., and Hutchinson, J. W. (1991). Kinking of a crack out of an interface: Role of in-plane stress. *J. Amer. Ceram. Soc.*, 74(4):767–771. _eprint: https://ceramics.onlinelibrary.wiley.com/doi/pdf/10.1111/j.1151-2916.1991.tb06922.x. 81

He, M.-Y., Evans, A., and Hutchinson, J. W. (1994). Crack deflection at an interface between dissimilar elastic materials: Role of residual stress. *Int. J. Solids Struc.*, 31:3443. 10, 82, 83, 84, 86, 104

He, M.-Y., Hsueh, C., and Becher, P. (2000). Deflection versus penetration of a wedge-loaded crack: effects of branch-crack length and penetrated-layer width. *Compos. B. Eng.*, 31(4):299–308. 10, 83, 84

He, M.-Y. and Hutchinson, J. W. (1989a). Crack deflection at an interface between dissimilar elastic materials. *Int. J. Solids Struc.*, 25(9):1053–1067. 10, 11, 82, 83, 84, 86, 87, 88, 91, 104

He, M.-Y. and Hutchinson, J. W. (1989b). Kinking of a crack out of an interface. *J. Appl. Mech.*, 56(2):270–278. Publisher: American Society of Mechanical Engineers Digital Collection. 81

Hu, Y. T., Fisher, D., Kurian, P., and Calaway, R. (2018). Proppant transport by a high viscosity friction reducer. In *SPE Hydraulic Fracturing Technology Conference and Exhibition*. OnePetro. 21, 33

Hull, K. L., Abousleiman, Y. N., Han, Y., Al-Muntasheri, G. A., Hosemann, P., Parker, S. S., and Howard, C. B. (2015). New insights on the mechanical characterization of kerogen-rich shale, krs. In *Abu Dhabi International Petroleum Exhibition and Conference*. OnePetro. 25, 36

Hunsweck, M. J., Shen, Y., and Lew, A. J. (2013). A finite element approach to the simulation of hydraulic fractures with lag. *Int. J. Numer. Anal. Methods Geomech.*, 37(9):993–1015. 42, 53, 56

Hutchinson, J. W., Mear, M., and Rice, J. R. (1987). Crack paralleling an interface between dissimilar materials. *J. Appl. Mech.* 81, 82, 114

Hutchinson, J. W. and Suo, Z. (1991). Mixed mode cracking in layered materials. In *Adv. Appl. Mech.*, volume 29, pages 63–191. Elsevier. 81, 114, 149

Irwin, G. R. (1957). Analysis of stresses and strains near the end of a crack traversing a plate. *J. Appl. Mech.* 96, 149

Kanninen, M. F. and Popelar, C. H. (1985). *Advanced Fracture Mechanics*. Oxford University Press, Oxford UK. 44

Khristianovic, S. and Zheltov, Y. (1955). Formation of vertical fractures by means of highly viscous liquid. In *4th World Petroleum Congress*, pages 579–586, Rome, Italy. World Petroleum Council. 41

Kresse, O., Weng, X., Chuprakov, D., Prioul, R., and Cohen, C. (2013). Effect of flow rate and viscosity on complex fracture development in UFM model. *Effective and Sustainable Hydraulic Fracturing*. Publisher: IntechOpen. 23, 35, 41

Lawn, B. R. (2004). Fracture and deformation in brittle solids: A perspective on the issue of scale. *J. Mater. Res.*, 19(1):22–29. 149

Lecampion, B. and Detournay, E. (2007). An implicit algorithm for the propagation of a hydraulic fracture with a fluid lag. *Comput. Meth. App. Mech. Eng.*, 196(49-52):4863–4880. 8, 9, 42, 50, 51, 56, 57, 69

Legarth, B., Huenges, E., and Zimmermann, G. (2005). Hydraulic fracturing in a sedimentary geothermal reservoir: Results and implications. *Int. J. Rock Mech. Mining Sci.*, 42(7):1028–1041. 40

Leguillon, D. (2002). Strength or toughness? A criterion for crack onset at a notch. *Eur. J. Mech. A/Solids*, 21(1):61–72. 81, 114

Lu, M.-C. and Erdogan, F. (1983). Stress intensity factors in two bonded elastic layers containing cracks perpendicular to and on the interface—I. analysis. *Eng. Frac. Mech.*, 18(3):491–506. 82

Malhotra, S., Rijken, P., and Sanchez, A. (2018). Experimental investigation of propellant fracturing in a large sandstone block. *SPE Drill. Complet.*, 33(02):87–99. 24, 36

Manchanda, R., Bryant, E. C., Bhardwaj, P., Cardiff, P., and Sharma, M. M. (2018). Strategies for effective stimulation of multiple perforation clusters in horizontal wells. *SPE Prod. Oper.*, 33(03):539–556. 25, 37

Martinez, D. and Gupta, V. (1994). Energy criterion for crack deflection at an interface between two orthotropic media. *J. Mech. Phys. Solids*, 42(8):1247–1271. 82

McClure, M. W. and Horne, R. N. (2013). *Discrete fracture network modeling of hydraulic stimulation: Coupling flow and geomechanics*. Springer Science & Business Media. 25, 36

Medlin, W. L. and Masse, L. (1984). Laboratory experiments in fracture propagation. *SPE J.*, 24(03):256–268. 41

Middleton, R., Viswanathan, H., Currier, R., and Gupta, R. (2014). CO_2 as a fracturing fluid: Potential for commercial-scale shale gas production and CO_2 sequestration. *Energy Proc.*, 63:7780–7784. 40

Moës, N. and Belytschko, T. (2002). Extended finite element method for cohesive crack growth. *Eng. Frac. Mech.*, 69(7):813–833. 67

Mokryakov, V. (2011). Analytical solution for propagation of hydraulic fracture with barenblatt's cohesive tip zone. *Int. J. Fract.*, 169(2):159–168. 25, 37

Murdoch, L. (2002). Mechanical analysis of idealized shallow hydraulic fracture. *J. Geotech. Geoenviron.*, 128(6):488–495. 40

Nagel, N., Zhang, F., Sanchez-Nagel, M., Lee, B., and Agharazi, A. (2013). Stress shadow evaluations for completion design in unconventional plays. In *SPE Unconventional Resources Conference Canada*. OnePetro. 23, 35

Nuismer, R. J. (1975). An energy release rate criterion for mixed mode fracture. *Int. J. Fract.*, 11(2):245–250. 149

Ortiz, M. and Pandolfi, A. (1999). Finite-deformation irreversible cohesive elements for three-dimensional crack-propagation analysis. *Int. J. Numer. Methods Eng.*, 44(9):1267–1282. 45, 46

Parmigiani, J. and Thouless, M. (2006). The roles of toughness and cohesive strength on crack deflection at interfaces. *J. Mech. Phys. Solids*, 54(2):266–287. 10, 81, 82, 83, 84, 85, 88, 90, 104, 105, 114

Parmigiani, J. and Thouless, M. (2007). The effects of cohesive strength and toughness on mixed-mode delamination of beam-like geometries. *Eng. Frac. Mech.*, 74(17):2675–2699. 81

Parmigiani, J. P. (2007). *Delamination and deflection at interfaces.* PhD thesis, University of Michigan, 2007. 81

Ponce, J. J., Montagna, A. O., Carmona, N., Brisson, I., Buhler, M., and Fernandez, M. (2015). Geología de la cuenca neuquina y sus sistemas petroleros. *Fundación YPF*. 17, 28

Pro, J. W., Sehr, S., Lim, R. K., Petzold, L. R., and Begley, M. R. (2018). Conditions controlling kink crack nucleation out of, and delamination along, a mixed-mode interface crack. *J. Mech. Phys. Solids*, 121:480–495. 67, 81

Radovitzky, R., Seagraves, A., Tupek, M., and Noels, L. (2011). A scalable 3d fracture and fragmentation algorithm based on a hybrid, discontinuous galerkin, cohesive element method. *Comput. Meth. App. Mech. Eng.*, 200(1-4):326–344. 46

Remij, E., Remmers, J., Huyghe, J., and Smeulders, D. (2018). On the numerical simulation of crack interaction in hydraulic fracturing. *Computational Geosciences*, 22:423–437. 23, 35

Rice, J. R. (1992). Dislocation nucleation from a crack tip: an analysis based on the peierls concept. *J. Mech. Phys. Solids*, 40(2):239–271. 63

Rice, J. R. and Beltz, G. E. (1994). The activation energy for dislocation nucleation at a crack. *J. Mech. Phys. Solids*, 42(2):333–360. 63

Roshankhah, S., Cruz, L., Shin, H., Lizcano, A., and Santamarina, J. (2019). Kinematic dilation during the hydraulic stimulation of pre-fractured rocks. *Geotech. Lett.*, 9(3):186–192. 61

Roshankhah, S., Marshall, J., Tengattini, A., Ando, E., Rubino, V., Rosakis, A., Viggiani, G., and Andrade, J. (2018). Neutron imaging: a new possibility for laboratory observation of hydraulic fractures in shale? *Geotech. Lett.*, 8(4):316–323. 61

Rubin, A. (1995). Propagation of magma-filled cracks. *Annu. Rev. Earth and Plan. Sci.*, 23:287–336. 40

Rudnicki, J. (2000). Geomechanics. *Int. J. Solids Struc.*, 37:349–358. 40

Ruiz, G., Pandolfi, A., and Ortiz, M. (2001). Three-dimensional cohesive modeling of dynamic mixed-mode fracture. *Int. J. Numer. Methods Eng.*, 52(1-2):97–120. 63

Salimzadeh, S. and Khalili, N. (2015). A three-phase XFEM model for hydraulic fracturing with cohesive crack propagation. *Comp. Geotech.*, 69:82–92. 41

Savitski, A. A. and Detournay, E. (2002). Propagation of a penny-shaped fluid-driven fracture in an impermeable rock: Asymptotic solutions. *Int. J. Solids Struc.*, 39(26):6311–6337. 50

Serebrinsky, S. A., Winograd, E. A., Celleri, H. M., Sánchez, M., Alvarez, J. P., Hryb, D. E., and López, R. G. (2017). Finite elements simulation of the interaction of a hydraulic fracture with a natural fracture. In *51st US Rock Mechanics/Geomechanics Symposium*, page 1044, San Francisco, California, USA. American Rock Mechanics Association, American Rock Mechanics Association. 41

Sesetty, V. and Ghassemi, A. (2017). Complex fracture network model for stimulation of unconventional reservoirs. In *51st US Rock Mechanics/Geomechanics Symposium*. OnePetro. 25, 36

Shen, Y. (2014). A variational inequality formulation to incorporate the fluid lag in fluid-driven fracture propagation. *Comput. Meth. App. Mech. Eng.*, 272:17–33. 42

Shrivastava, K. and Sharma, M. M. (2018). Mechanisms for the formation of complex fracture networks in naturally fractured rocks. In *SPE Hydraulic Fracturing Technology Conference and Exhibition*. OnePetro. 25, 36

Smilovich, D., Baldini, M., Celleri, H. M., Gutiérrez, J., Gallana, I., Castez, M. F., and Serebrinsky, S. (2023). A pseudo-transient-based staggered algorithm for hydraulic fracturing simulations in the absence of a fluid lag. *Comp. Geotech.*, 155:105202. 74

Smilovich, D., Radovitzky, R., and Dvorkin, E. (2018). Mesh dependent properties to produce mesh independent results in fracture mechanic simulations. In *World Conference on Computational Mechanics (WCCM2018)*, New York, NY, USA. 78

Smilovich, D., Radovitzky, R., and Dvorkin, E. (2021). A parallel staggered hydraulic fracture simulator incorporating fluid lag. *Comput. Meth. App. Mech. Eng.*, 384:114003. 42, 50, 56, 72

Sone, H. and Zoback, M. D. (2013). Mechanical properties of shale-gas reservoir rocks—part 1: Static and dynamic elastic properties and anisotropy. *Geophysics*, 78(5):D381–D392. 25, 36

Sousa, J., Carter, B., and Ingraffea, A. (1993). Numerical simulation of 3D hydraulic fracture using Newtonian and power-law fluids. *Int. J. Rock Mech. Mining Sci. Geomech. Abs.*, 30(7):1265–1271. 41

Spence, D. and Turcotte, D. (1985). Magma-driven propagation of cracks. *J. Geophys. Res. Sol. Earth*, 90(B1):575–580. 40

Spence, D. A., Sharp, P., and Benjamin, T. B. (1985). Self-similar solutions for elastohydrodynamic cavity flow. *Proc. R. Soc. London. A. Math. Phys. Sci.*, 400(1819):289–313. 41

Strom, J. L. and Parmigiani, J. P. (2014). Transition of crack path at bi-material interfaces. *Eng. Frac. Mech.*, 115:13–21. 10, 11, 81, 83, 84, 85, 86, 87, 89, 90, 91, 103

Tada, H., Paris, P. C., and Irwin, G. R. (1973). The stress analysis of cracks. *Handbook, Del Research Corporation*, 34:635. 86

Taleghani, A. D., Gonzalez-Chavez, M., Yu, H., and Asala, H. (2018). Numerical simulation of hydraulic fracture propagation in naturally fractured formations using the cohesive zone model. *J. Pet. Sci. Eng.*, 165:42–57. 24, 26, 35, 37

Taleghani, D. A. and Olson, J. E. (2011). Numerical modeling of multistranded-hydraulic-fracture propagation: accounting for the interaction between induced and natural fractures. *SPE J.*, 16(03):575–581. 25, 36, 61

Thouless, M., Cao, H., and Mataga, P. (1989). Delamination from surface cracks in composite materials. *J. Mater. Sci.*, 24(4):1406–1412. 82

Tullock, D., Reimanis, I., Graham, A., and Petrovic, J. (1994). Deflection and penetration of cracks at an interface between two dissimilar materials. *Acta Metall. Mater.*, 42(9):3245–3252. 82

Turon, A., Davila, C. G., Camanho, P. P., and Costa, J. (2007). An engineering solution for mesh size effects in the simulation of delamination using cohesive zone models. *Eng. Frac. Mech.*, 74(10):1665–1682. 63, 67, 78, 112, 113

Ukar, E., Lopez, R. G., Laubach, S. E., Gale, J. F., Manceda, R., and Marrett, R. (2017). Microfractures in bed-parallel veins (beef) as predictors of vertical macrofractures in shale: Vaca Muerta Formation, Agrio Fold-and-Thrust Belt, Argentina. *J. S. Am. Earth Sci.*, 79:152–169. 20, 31

Vahab, M. and Khalili, N. (2018). Computational algorithm for the anticipation of the fluid-lag zone in hydraulic fracturing treatments. *Int. J. Geomech.*, 18(10):04018139. 42

Valkó, P. and Economides, M. J. (1995). *Hydraulic fracture mechanics*, volume 28. Wiley Chichester. 61

Wang, H. (2019). Hydraulic fracture propagation in naturally fractured reservoirs: Complex fracture or fracture networks. *J. Nat. Gas Sci. Eng.*, 68:102911. 23, 25, 34, 36, 37

Wang, H., Marongiu-Porcu, M., and Economides, M. J. (2016a). Poroelastic and poroplastic modeling of hydraulic fracturing in brittle and ductile formations. *SPE Prod. Oper.*, 31(01):47–59. 25, 37

Wang, T., Hu, W., Elsworth, D., Zhou, W., Zhou, W., Zhao, X., and Zhao, L. (2017). The effect of natural fractures on hydraulic fracturing propagation in coal seams. *J. Pet. Sci. Eng.*, 150:180–190. 23, 24, 34, 35

Wang, Y., Li, X., and Tang, C. (2016b). Effect of injection rate on hydraulic fracturing in naturally fractured shale formations: a numerical study. *Environmental Earth Sciences*, 75:1–16. 20, 31

Warpinski, N. (2011). Fracture growth in layered and discontinuous media. In *Proceedings of the Technical Workshops for the Hydraulic Fracturing Study: Fate and Transport*. Environ. Prot. Agency Washington, DC. 10, 71

Warpinski, N. R. (1985). Measurement of width and pressure in a propagating hydraulic fracture. *SPE J.*, 25(01):46–54. 41

Warpinski, N. R., Mayerhofer, M. J., Vincent, M. C., Cipolla, C. L., and Lolon, E. (2009). Stimulating unconventional reservoirs: maximizing network growth while optimizing fracture conductivity. *J. Can. Pet. Technol.*, 48(10):39–51. 23, 34, 61

Weng, X., Kresse, O., Chuprakov, D., Cohen, C.-E., Prioul, R., and Ganguly, U. (2014). Applying complex fracture model and integrated workflow in unconventional reservoirs. *J. Pet. Sci. Eng.*, 124:468–483. 23, 35

Weng, X., Kresse, O., Cohen, C., Wu, R., and Gu, H. y. o. (2011). Modeling of hydraulic fracture network propagation in a naturally fractured formation. In *SPE Hydraulic Fracturing Technology Conference*. Society of Petroleum Engineers. 23, 25, 35, 36, 61

Wong, T.-f. and Baud, P. (2012). The brittle-ductile transition in porous rock: A review. *J. Struct. Geol.*, 44:25–53. 25, 37

Wu, K., Olson, J., Balhoff, M. T., and Yu, W. (2017). Numerical analysis for promoting uniform development of simultaneous multiple-fracture propagation in horizontal wells. *SPE Prod. Oper.*, 32(01):41–50. 23, 35

Wu, K. and Olson, J. E. (2015). A simplified three-dimensional displacement discontinuity method for multiple fracture simulations. *Int. J. Fract.*, 193(2):191–204. 41

Yang, D., Wang, W., Li, K., Chen, W., Yang, J., and Wang, S. (2019). Experimental investigation on the stress sensitivity of permeability in naturally fractured shale. *Environ. Earth Sci.*, 78:1–10. 23, 34

Ye, Z., Sesetty, V., and Ghassemi, A. (2018). Experimental and numerical investigation of shear stimulation and permeability evolution in shales. In *SPE Hydraulic Fracturing Technology Conference and Exhibition*. OnePetro. 23, 35

Zeng, X. and Wei, Y. (2017). Crack deflection in brittle media with heterogeneous interfaces and its application in shale fracking. *J. Mech. Phys. Solids*, 101:235–249. 150

Zhang, J., Biao, F., Zhang, S., and Wang, X. (2012). A numerical study on horizontal hydraulic fracture. *J. Pet. Explor. Prod. Technol.*, 2:7–13. 23, 35

Zhang, X., Jeffrey, R. G., and Detournay, E. (2005). Propagation of a hydraulic fracture parallel to a free surface. *Int. J. Numer. Anal. Methods Geomech.*, 29:1317–1340. 41

Zhou, J. (2016). *Hydraulic fracture propagation modeling and data-based fracture identification*. Ph.D. thesis for the University of Utah. 23, 35

Zimmermann, G. and Reinicke, A. (2010). Hydraulic stimulation of a deep sandstone reservoir to develop an enhanced geothermal system: Laboratory and field experiments. *Geothermics*, 39(1):70–77. 21, 32